

Effect of Carbon Steel Composition and Microstructure on CO<sub>2</sub> Corrosion

A dissertation presented to  
the faculty of  
the Russ College of Engineering and Technology of Ohio University

In partial fulfillment  
of the requirements for the degree  
Doctor of Philosophy

Emad S. Akeer

August 2014

©2014 Emad S. Akeer. All Rights Reserved.

This dissertation titled  
Effect of Carbon Steel Composition and Microstructure on CO<sub>2</sub> Corrosion

by

EMAD S. AKEER

has been approved for  
the Department of Chemical and Biomolecular Engineering  
and the Russ College of Engineering and Technology by

Srdjan Nestic

Professor of Chemical and Biomolecular Engineering

Dennis Irwin

Dean, Russ College of Engineering and Technology

## ABSTRACT

AKEER, EMAD S., Ph.D., August 2014, Chemical Engineering

Effect of Carbon Steel Composition and Microstructure on CO<sub>2</sub> Corrosion

Director of Dissertation: Srdjan Nestic

The environmental conditions encountered in oil and gas wells and pipelines can cause severe localized corrosion to mild steel. The utility of carbon steel in oil and gas pipelines depends on formation of protective corrosion product layers. However, the microstructure and chemical composition of steel are considered to be important variables that affect the ability of these layers to protect steel from corrosion.

The present study investigated the effect of alloying elements and metallurgy of five different pipeline steels, with different chemical composition and microstructure, on CO<sub>2</sub> corrosion in flowing conditions with focus on the iron carbonate layer formed and related corrosion phenomena that could lead to localized corrosion.

The microstructure of tested steels was examined using optical microscopy and etching. Preliminary experiments were conducted using a glass cell, which is a very well known and widely used apparatus. Then a comparison was done with the newly developed thin channel flow cell (TCFC) to validate whether the TCFC can be used instead of glass cell in this study, which required very high velocity and wall shear stresses. It was found that there are no significant effects of alloying elements and steel microstructure on corrosion rate in experiments done at pH 4.0 at 25°C and 80°C.

Further experiments were then conducted in the TCFC to study the effect of alloying elements and microstructure under conditions where a protective FeCO<sub>3</sub>

corrosion product layer forms, using very high liquid flow rates. For each of the studied steels, an  $\text{FeCO}_3$  corrosion product layer was formed within two days of exposure at low wall shear stress at  $80^\circ\text{C}$ , pH 6.6, and partial pressure of  $\text{CO}_2$  of 1.5 bar (1.5 bar  $\text{pCO}_2$ ). For all tested steels, the  $\text{FeCO}_3$  layer reduced the general corrosion rate to less than 1.0 mm/y. These "pre-formed"  $\text{FeCO}_3$  layers were then exposed to high liquid flow velocity and wall shear stress (535 Pa) for 3 days. This caused partial loss of the protective  $\text{FeCO}_3$  layer which was probably related to the local increase in shear stress and the changes in pressure caused by turbulence at the high flow rates.

Although all steels suffered from pitting corrosion to different degrees, the  $\text{FeCO}_3$  layer formed on normalized steel was more protective than the one formed on quenched and tempered steel (Q&T). This can be attributed to microstructure, because the pearlite structures present in the normalized steel conferred superior  $\text{FeCO}_3$  adherence to the steel surface. On the other hand, X65II steel, which has metallurgical characteristics consistent with a normalized hot rolled material, suffered pitting corrosion, which initiated even before increasing wall shear stress. This type of localized corrosion was related to inclusions and phase distributions within the ferrite/pearlite microstructure.

In a separate series of experiments, the formation mechanisms of the  $\text{FeCO}_3$  corrosion product layer were challenged for each steel at high wall shear stress (535Pa) and at  $80^\circ\text{C}$ , pH 6.6, and 1.5 bar  $\text{pCO}_2$ . It was observed that the  $\text{FeCO}_3$  corrosion product layers did not form at this high wall shear stress, even under conditions that were supersaturated with respect to  $\text{FeCO}_3$ . This was related to mass transfer behavior, where the fast movement of species from and toward the steel surface contributed to removal of

generated ferrous ions and prevented the formation of an  $\text{FeCO}_3$  layer. High local shear stresses may have also mechanically interfered with formation of any  $\text{FeCO}_3$  layer on the steel surface. At high wall shear stress, the general corrosion rates of normalized steels (X52, A106GRB) are higher than for Q&T steels. This can be related to the amount of iron carbides in the steel. There was no localized corrosion observed at high wall shear stress since no  $\text{FeCO}_3$  formed on the steels.

*Keywords:  $\text{CO}_2$  corrosion, wall shear stress, iron carbonate, steel microstructure, normalized, quenched and tempered.*

## DEDICATION

*To*

*My Wife*

*My parents*

*and all other family members*

*for their*

*love, care and support*

## ACKNOWLEDGMENTS

I would like to thank my academic advisor, Dr. Srdjan Nesic, for his enthusiasm, and his encouragement. I would like to thank Mr. Bruce Brown, my project leader, for his support and advice in my research work. Actually, Mr. Brown was patient and helpful even when he was busy, he always tried to help me as much as he could. I would like to thank Dr. David Young who supported and advised me in my proposal and dissertation writing. I would also like to thank Stephen Smith for his support and advice in my research especially in relation to metallurgy. I am also indebted to my committee members, Dr. Tingyue Gu, Dr. Pasic Hajrudin, Dr. Martin Kordesch, and Dr. Lauren McMills for their support and academic advice in my proposal and dissertation. I would like to acknowledge all staff at the Institute for Corrosion and Multiphase Technology, Mr. Albert Schubert, Mr. Danny Cain, Mr. Cody Shafer, Mr. Steve Upton and Mr. Phil Bullington for their assistance in my experimental work. I also would like to thank Rebecca Gill for her assistance. I also would like to thank all the post-docs and students for their help. I would like to acknowledge the high education minister of Libya for financial support during my PhD. I want to thank all the sponsoring companies for their technical and financial support during my PhD work. I would like to thank my wife for her care and support during my PhD work. Also I would like to thank all my family members, my mother, my father, my sisters and brothers, for their care and support.

## TABLE OF CONTENTS

	Page
Abstract.....	3
Dedication.....	6
Acknowledgments.....	7
List of Tables.....	11
List of Figures.....	12
Chapter 1: Introduction.....	26
Chapter 2: Literature Review.....	28
2.1    CO <sub>2</sub> Corrosion.....	28
2.1.1    Chemical Reactions.....	28
2.1.2    Electrochemical Reactions.....	29
2.1.3    Mass Transport.....	30
2.1.4    Iron Carbonate as Corrosion Product.....	31
2.2    Flow Effects.....	31
2.3    Steel Composition and Microstructural Effects.....	33
2.3.1    Bare Steel as a Corroding Substrate.....	34
2.3.2    Corrosion Inhibitors and Metallurgical Characteristics.....	37
Chapter 3: Hypothesis and Research Objectives.....	39
3.1    Hypothesis.....	39
3.2    Research Objective.....	39
Chapter 4: Metallographic Analysis.....	40
4.1    Introduction.....	40

	9
4.2	Chemical Composition of Chosen Steels .....45
4.3	Microstructure of Chosen Steels .....46
4.4	Grain Size.....55
4.4.1	Intercept Method, ASTM E112 Standard .....55
4.4.2	ImageJ Software .....56
Chapter 5: General Corrosion Experiments .....59	
5.1	Introduction.....59
5.2	Tests done in a Glass Cell with a Rotating Cylinder Electrode (RCE).....59
5.2.1	Sample Materials.....59
5.2.2	Experimental Method .....59
5.2.3	Results and Discussion .....63
5.3	Tests done in the Thin Channel Flow Cell (TCFC) System.....65
5.3.1	Sample Materials.....65
5.3.2	Experimental Method .....65
5.3.3	Results and Discussion .....68
5.4	Summary .....72
Chapter 6: Flow Effect Experiments .....73	
6.1	Introduction.....73
6.2	Wall Shear Stress Determination .....74
6.3	Effect of Flow on Formed FeCO <sub>3</sub> Corrosion Product Layer .....77
6.3.1	Introduction.....77
6.3.2	Experimental Method .....78

	10
6.3.3 Results .....	79
6.3.4 Summary.....	123
6.3.5 Discussion.....	127
6.4 Summary .....	131
Chapter 7: Determination of FeCO <sub>3</sub> Formation at High Wall Shear Stress .....	133
7.1 Introduction.....	133
7.2 Experimental Method .....	133
7.3 Results.....	135
7.4 Summary .....	148
7.5 Discussion .....	150
Chapter 8: Conclusions and Future Work.....	154
8.1 Conclusions.....	154
8.2 Future Work.....	156
References.....	157
Appendix A: Grinding, Polishing, and Etching Procedures .....	166
Appendix B: Intercept Method and ImageJ Software .....	170
Intercept Method, ASTM E112 Standard:.....	170
ImageJ Software:.....	172
Appendix C: Thin Channel Flow Cell (TCFC) System Design.....	174
Appendix D: Repeated Experiments .....	177

## LIST OF TABLES

	Page
Table 1: Chemical Composition of X65I, X65II, and X70 Steels. ....	45
Table 2: Chemical Composition of A106GRB and X52 Steels. ....	46
Table 3: Microstructure and Heat Treatment of the Tested Steels. ....	55
Table 4: Grain Sizes of X65 II, X52, and A106GRB Steels. ....	58
Table 5: Test Matrix: Glass Cell Experiments (Uniform Corrosion). ....	62
Table 6: Test Matrix: TCFC Experiments (Uniform Corrosion) ....	67
Table 7: Physical Properties of Water and Reynolds Number at Shear Stress of 535 Pa. ....	63
Table 8: Test Matrix: The Effect of High Wall Shear Stress ( $\tau = 535$ Pa) on Adhesion and Protection from an $\text{FeCO}_3$ Layer Formed at Low Wall Shear Stress ( $\tau =$ 35 Pa). ....	77
Table 9: Test Matrix: Determination of $\text{FeCO}_3$ at High Wall Shear Stress ( $\tau = 535$ Pa). ....	134

## LIST OF FIGURES

	Page
Figure 1: Diagram of the destruction mechanisms for surface layer caused by pressure changes near the steel surface [45].	33
Figure 2: Mechanism of $\text{FeCO}_3$ development for F/P steels.	37
Figure 3: Fe-C phase diagram shows the phase transformation from austenite to ferrite/pearlite (slow cooling) and from austenite to martensite (fast cooling), where; white = ferrite, gray = pearlite [60].	41
Figure 4: CCT diagram for 0.4wt% C steel shows the phase transformation form austenite to martensite in the fast cooling processes.	43
Figure 5: CCT diagram for 0.4wt% C steel shows the final obtained microstructure (martensite) in the fast cooling processes.	43
Figure 6: CCT diagram for 0.4wt% C steel shows the phase transformation form austenite to ferrite in the slow cooling processes.	44
Figure 7: CCT diagram for 0.4wt% C steel shows the phase transformation form austenite to ferrite/pearlite in the slow cooling processes.	44
Figure 8: Preparation of samples for metallographic analysis.	47
Figure 9: X65I steel, plane A, B, C microstructures.	49
Figure 10: X65I steel, microstructure consists of tempered martensite.	49
Figure 11: X70 steel, plane A, B, C microstructures.	50

	13
Figure 12: X70 steel, microstructure consists of tempered martensite.....	50
Figure 13: X65II steel, plane A, B, C microstructures. ....	51
Figure 14: X65II steel, there is difference in the microstructure between plane A and B. ....	51
Figure 15: X52 steel, plane A, B, C microstructures.....	53
Figure 16: X52 steel, microstructure consists of large dark pearlite surrounded by large bright ferrite. ....	53
Figure 17: A106GRB, plane A, B, C microstructures.....	54
Figure 18: A106GRB steel, microstructure consists of large dark pearlite surrounded by large bright ferrite.....	54
Figure 19: Comparison between images that obtained by optical microscopy and IFM. .	57
Figure 20: Schematic image of glass cell used to conduct the corrosion experiments. ....	62
Figure 21: RCE corrosion rate at 25°C, 0.95 bar CO <sub>2</sub> , pH 4.0, 1000 rpm, and B=26 mV/decade. ....	64
Figure 22: RCE corrosion rate at 80°C, 0.5 bar CO <sub>2</sub> , pH 4.0, 1000 rpm, and B=26 mV/decade. ....	64
Figure 23: Schematic diagram of the thin channel flow cell (TCFC) system and samples used to conduct corrosion experiments. ....	68
Figure 24: TCFC corrosion rate measured by LPR, weight loss (WL), at 25°C, 0.95 bar CO <sub>2</sub> , pH 4.0, 0.63 m/s, B=26 mV/decade. ....	70

Figure 25: TCFC corrosion rate measured by LPR, weight loss (WL), at 80°C, 0.5 bar CO <sub>2</sub> , pH 4.0, 0.63 m/s, B=26 mV/decade. ....	70
Figure 26: Comparison between RCE & TCFC corrosion rates measured by LPR, at 25°C, 0.95 bar CO <sub>2</sub> , pH 4.0, 0.63m/s, B=26 mV/decade.....	71
Figure 27: Comparison between RCE & TCFC corrosion rates measured by LPR, at 80°C, 0.5 bar CO <sub>2</sub> , pH 4.0, 0.63 m/s, B=26 mV/decade.....	71
Figure 28: Schematic diagram of the thin channel flow cell (TCFC) used to conduct pressure drop measurement.....	76
Figure 29: Wall shear stresses in the TCFC measured at 25° C with different methods for various flow velocities. ....	77
Figure 30: Corrosion rate obtained from LPR measurements versus exposure time at 80°C, 1.5 bar CO <sub>2</sub> , pH 6.6, B=26 mV/decade, $\tau$ = 35 Pa for the first 2 days, $\tau$ = 535 Pa for another 3 days. ....	81
Figure 31: LPR Corrosion rate of X65I steel during 5 days of exposure at 80°C, 1.5 bar CO <sub>2</sub> , pH 6.6, B=26 mV/decade, $\tau$ = 35 Pa for the first 2 days, $\tau$ = 535 Pa for another 3 days.....	82
Figure 32: SEM top surface analysis of FeCO <sub>3</sub> layer after 2 days of exposure at 80°C, X65I steel, 1.5 bar CO <sub>2</sub> , pH 6.6, $\tau$ = 35 Pa for the first 2 days. ....	83
Figure 33: SEM & EDS top surface analysis of FeCO <sub>3</sub> layer after 2 days of exposure at 80°C, X65I steel, 1.5 bar CO <sub>2</sub> , pH 6.6, $\tau$ = 35 Pa for the first 2 days.....	83

Figure 34: SEM cross section analysis of $\text{FeCO}_3$ layer after 2 days of exposure at $80^\circ\text{C}$ , X65I steel, 1.5 bar $\text{CO}_2$ , pH 6.6, $\tau=35$ Pa for the first 2 days. ....	84
Figure 35: Comparison between corrosion rates measured by weight loss (WL) and integrated LPR after 5 days of exposure at $80^\circ\text{C}$ , X65I steel, 1.5 bar $\text{CO}_2$ , pH 6.6, $B=26$ mV/decade, $\tau=35$ Pa for the first 2 days, $\tau=535$ Pa for another 3 days. ....	86
Figure 36: SEM top surface analysis of $\text{FeCO}_3$ layer after 5 days of exposure at $80^\circ\text{C}$ , X65I steel, 1.5 bar $\text{CO}_2$ , pH 6.6, $\tau=35$ Pa for the first 2 days, $\tau=535$ Pa for another 3 days.....	86
Figure 37: SEM & EDS top surface analysis of $\text{FeCO}_3$ layer after 5 days of exposure at $80^\circ\text{C}$ , X65I steel, 1.5 bar $\text{CO}_2$ , pH 6.6, $\tau=35$ Pa for the first 2 days, $\tau=535$ Pa for another 3 days.....	87
Figure 38: IFM image of descaled sample after 5 days of exposure at $80^\circ\text{C}$ , X65I steel, 1.5 bar $\text{CO}_2$ , pH 6.6, $\tau=35$ Pa for the first 2 days, $\tau=535$ Pa for another 3 days. Size of the deepest pit is $500\mu\text{m}$ in width & $70\mu\text{m}$ in depth. ....	87
Figure 39: Comparison between the final corrosion rate measured by LPR and the penetration rate of the deepest pit on each steel (PR) after 5 days of exposure at $80^\circ\text{C}$ , X65I steel, 1.5 bar $\text{CO}_2$ , pH 6.6, $B=26$ mV/decade, $\tau=35$ Pa for the first 2 days, $\tau=535$ Pa for another 3 days.....	88
Figure 40: LPR Corrosion Rate of X70 steel during 5 days of exposure at $80^\circ\text{C}$ , 1.5 bar $\text{CO}_2$ , pH 6.6, $B=26$ mV/decade, $\tau=35$ Pa for the first 2 days, $\tau=535$ Pa for another 3 days. ....	89

Figure 41: SEM analysis of X70 steel after 2 days of exposure at 80°C, 1.5 bar pCO <sub>2</sub> , pH 6.6, $\tau = 35$ Pa showing top surface view of FeCO <sub>3</sub> layer.....	89
Figure 42: SEM & EDS top surface analysis of X70 steel after 2 days of exposure at 80°C, 1.5 bar CO <sub>2</sub> , pH 6.6, $\tau = 35$ Pa. ....	90
Figure 43: SEM & EDS cross section analysis of X70 steel after 2 days of exposure at 80°C, 1.5 bar CO <sub>2</sub> , pH 6.6, $\tau = 35$ Pa for the first 2 days. ....	90
Figure 44: Comparison between corrosion rates of X70 measured by weight loss (WL) and integrated LPR after 5 days of exposure at 80°C, 1.5 bar CO <sub>2</sub> , pH 6.6, B=26 mV/decade, $\tau = 35$ Pa for the first 2 days, $\tau = 535$ Pa for another 3 days. ....	92
Figure 45: SEM top surface analysis of FeCO <sub>3</sub> layer after 5 days of exposure at 80°C, X70 steel, 1.5 bar CO <sub>2</sub> , pH 6.6, $\tau = 35$ Pa for the first 2 days, $\tau = 535$ Pa for another 3 days. ....	93
Figure 46: SEM & EDS top surface analysis of FeCO <sub>3</sub> layer after 5 days of exposure at 80°C, X70 steel, 1.5 bar CO <sub>2</sub> , pH 6.6, $\tau = 35$ Pa for the first 2 days, $\tau = 535$ Pa for another 3 days.....	93
Figure 47: IFM image of de-scaled sample after 5 days of exposure at 80°C, X70 steel, 1.5 bar CO <sub>2</sub> , pH 6.6, $\tau = 35$ Pa for the first 2 days, $\tau = 535$ Pa for another 3 days, Size of the deepest pit is 200 $\mu$ m in width & 50 $\mu$ m in depth. ....	94
Figure 48: Comparison between the final corrosion rate measured by LPR and penetration rate of the deepest pit on each steel (PR) after 5 days of exposure at 80°C,	

X70 steel, 1.5 bar CO <sub>2</sub> , pH 6.6, B=26 mV/decade, $\tau$ = 35 Pa for the first 2 days, $\tau$ = 535 Pa for another 3 days. ....	94
Figure 49: LPR Corrosion Rate of X70 steel (without initial Fe <sup>2+</sup> additions) during 11 days of exposure at 80°C, 1.5 bar CO <sub>2</sub> , pH 6.6, B=26 mV/decade, $\tau$ = 35 Pa for the first 8 days, $\tau$ = 535 Pa for another 3 days. ....	96
Figure 50: Comparison between SEM & EDS top surface analysis of FeCO <sub>3</sub> layer at 80°C, X70 steel, 1.5 bar CO <sub>2</sub> , pH 6.6, $\tau$ = 35 Pa for the FeCO <sub>3</sub> layer formation. ....	97
Figure 51: Comparison between SEM & EDS cross section analysis of FeCO <sub>3</sub> layer at 80°C, X70 steel, 1.5 bar CO <sub>2</sub> , pH 6.6, $\tau$ = 35 Pa for the FeCO <sub>3</sub> layer formation. ....	97
Figure 52: Comparison between corrosion rates measured by weight loss (WL) and integrated LPR (without initial Fe <sup>2+</sup> additions), after 5 days of exposure at 80°C, X70 steel, 1.5 bar CO <sub>2</sub> , pH 6.6, B=26 mV/decade, $\tau$ = 35 Pa for the FeCO <sub>3</sub> layer formation, $\tau$ = 535 Pa for the FeCO <sub>3</sub> layer removal. ....	98
Figure 53: Comparison between SEM top surface analysis of FeCO <sub>3</sub> layer At 80°C, X70 steel, 1.5 bar CO <sub>2</sub> , pH 6.6, $\tau$ = 35 Pa for the FeCO <sub>3</sub> layer formation, $\tau$ = 535 Pa for the FeCO <sub>3</sub> layer removal. ....	99
Figure 54: Comparison between SEM & EDS top surface analysis of FeCO <sub>3</sub> layer at 80°C, X70 steel, 1.5 bar CO <sub>2</sub> , pH 6.6, $\tau$ = 35 Pa for the FeCO <sub>3</sub> layer formation, $\tau$ = 535 Pa for the FeCO <sub>3</sub> layer removal. ....	99

- Figure 55: Comparison between IFM images of descaled sample at 80°C, X70 steel, 1.5 bar CO<sub>2</sub>, pH 6.6,  $\tau = 35$  Pa for the FeCO<sub>3</sub> layer formation,  $\tau = 535$  Pa for the FeCO<sub>3</sub> layer removal. Size of the deepest pit 200 $\mu$ m in width & 50  $\mu$ m in depth. .... 100
- Figure 56: Comparison between corrosion rates of X70 steel without addition of Fe<sup>2+</sup>, measured by weight loss (WL), integrated LPR, and penetration rate of the deepest pit on each steel (PR) after 5 days of exposure at 80°C, 1.5 bar CO<sub>2</sub>, pH 6.6, B=26 mV/decade,  $\tau = 35$  Pa for the FeCO<sub>3</sub> layer formation,  $\tau = 535$  Pa for the FeCO<sub>3</sub> layer removal. .... 100
- Figure 57: LPR Corrosion rate of X65II steel during 5 days of exposure at 80°C, 1.5 bar CO<sub>2</sub>, pH 6.6, B=26 mV/decade,  $\tau = 35$  Pa for the FeCO<sub>3</sub> layer formation,  $\tau = 35$  Pa for the first 2 days,  $\tau = 535$  Pa for another 3 days. .... 102
- Figure 58: SEM top surface analysis of FeCO<sub>3</sub> layer after 2 days of exposure at 80°C, X65II steel, 1.5 bar CO<sub>2</sub>, pH 6.6,  $\tau = 35$  Pa for the first 2 days. .... 103
- Figure 59: SEM & EDS top surface analysis of FeCO<sub>3</sub> layer after 2 days of exposure at 80°C, X65II steel, 1.5 bar CO<sub>2</sub>, pH 6.6,  $\tau = 35$  Pa for the first 2 days. .... 103
- Figure 60: SEM & EDS cross section analysis of FeCO<sub>3</sub> layer after 2 days of exposure at 80°C, X65II steel, 1.5 bar CO<sub>2</sub>, pH 6.6,  $\tau = 35$  Pa for the first 2 days. .... 104
- Figure 61: Experiment II, IFM image of FeCO<sub>3</sub> layer after 2 days of exposure at 80°C, X65II steel, 1.5 bar CO<sub>2</sub>, pH 6.6,  $\tau = 35$  Pa. .... 104
- Figure 62: Comparison between corrosion rates measured by weight loss (WL) and integrated LPR after 5 days of exposure (Experiment I), at 80°C, X65II steel, 1.5 bar

CO <sub>2</sub> , pH 6.6, B=26 mV/decade, $\tau$ = 35 Pa for the FeCO <sub>3</sub> layer formation, $\tau$ = 35 Pa for the first 2 days, $\tau$ = 535 Pa for another 3 days. ....	106
Figure 63: SEM top surface analysis of FeCO <sub>3</sub> layer after 5 days of exposure at 80°C, X65II steel, 1.5 bar CO <sub>2</sub> , pH 6.6, $\tau$ = 35 Pa for the first 2 days, $\tau$ = 535 Pa for another 3 days.....	107
Figure 64: SEM& EDS top surface analysis of FeCO <sub>3</sub> layer after 5 days of exposure at 80°C, X65II steel, 1.5 bar CO <sub>2</sub> , pH 6.6, $\tau$ = 35 Pa for the first 2 days, $\tau$ = 535 Pa for another 3 days.....	107
Figure 65: SEM cross section analysis of FeCO <sub>3</sub> layer after 2 days of exposure at 80°C, X65II steel, 1.5 bar CO <sub>2</sub> , pH 6.6, $\tau$ = 35 Pa for the first 2 days, $\tau$ = 535 Pa for another 3 days.....	108
Figure 66: IFM image of descaled sample after 5 days of exposure at 80°C, X65II steel, 1.5 bar CO <sub>2</sub> , pH 6.6, $\tau$ = 35 Pa for the first 2 days, $\tau$ = 535 Pa for another 3 days. Size of the deepest pit 250 $\mu$ m in width & 110 $\mu$ m in depth. ....	108
Figure 67: Comparison between corrosion rates measured by weight loss (WL), integrated LPR and average penetration rate of the deepest pits on each steel (Experiments I, II) (PR) after 5 days of exposure at 80°C, X65II steel, 1.5 bar CO <sub>2</sub> , pH 6.6, B =26 mV/decade, $\tau$ = 35 Pa for the first 2 days, $\tau$ = 535 Pa for another 3 days. .	109
Figure 68: LPR corrosion rate of X52 steel during 5 days of exposure at 80°C, 1.5 bar CO <sub>2</sub> , pH 6.6, B=26 mV/decade, $\tau$ = 35 Pa for the first 2 days, $\tau$ = 535 Pa for another 3 days.....	110

Figure 69: SEM top surface analysis of $\text{FeCO}_3$ layer after 2 days of exposure at $80^\circ\text{C}$ , X52 steel, 1.5 bar $\text{CO}_2$ , pH 6.6, $\tau=35$ Pa.....	111
Figure 70: SEM & EDS top surface analysis of $\text{FeCO}_3$ layer after 2 days of exposure at $80^\circ\text{C}$ , X52 steel, 1.5 bar $\text{CO}_2$ , pH 6.6, $\tau=35$ Pa. ....	111
Figure 71: SEM& EDS cross section analysis of $\text{FeCO}_3$ layer after 2 days of exposure at $80^\circ\text{C}$ , X52 steel, 1.5 bar $\text{CO}_2$ , pH 6.6, $\tau=35$ Pa for the first 2 days. ....	112
Figure 72: Comparison between corrosion rates measured by weight loss (WL) and integrated LPR after 5 days of exposure at $80^\circ\text{C}$ , X52 steel, 1.5 bar $\text{CO}_2$ , pH 6.6, $B=26$ mV/decade, $\tau=35$ Pa for the first 2 days, $\tau=535$ Pa for another 3 days. ....	113
Figure 73: SEM top surface analysis of $\text{FeCO}_3$ layer after 5 days of exposure at $80^\circ\text{C}$ , X52 steel, 1.5 bar $\text{CO}_2$ , pH 6.6, $\tau=35$ Pa for the first 2 days, $\tau=535$ Pa for another 3 days. ....	114
Figure 74: SEM & EDS top surface analysis of $\text{FeCO}_3$ layer after 5 days of exposure at $80^\circ\text{C}$ , X52 steel, 1.5 bar $\text{CO}_2$ , pH 6.6, $\tau=35$ Pa for the first 2 days, $\tau=535$ Pa for another 3 days.....	114
Figure 75: IFM image of de-scaled sample after 5 days of exposure at $80^\circ\text{C}$ , X52 steel, 1.5 bar $\text{CO}_2$ , pH 6.6 $\tau=35$ Pa for the first 2 days, $\tau=535$ Pa for another 3 days, Size of the deepest pit $120\mu\text{m}$ in width & $12\mu\text{m}$ in depth.....	115
Figure 76: Comparison between corrosion rates measured by weight loss (WL), integrated LPR , and penetration rate of the deepest pit on each steel (PR)after 5 days	

of exposure at 80°C, X52 steel, 1.5 bar CO <sub>2</sub> , pH 6.6, B=26 mV/decade, $\tau$ = 35 Pa for the first 2 days, $\tau$ = 535 Pa for another 3 days. ....	115
Figure 77: LPR corrosion rate during 5 days of exposure at 80°C, A106GRB steel, 1.5 bar CO <sub>2</sub> , pH 6.6, B=26 mV/decade, $\tau$ = 35 Pa for the first 2 days, $\tau$ = 535 Pa for another 3 days. ....	117
Figure 78: SEM top surface analysis of FeCO <sub>3</sub> layer after 2 days of exposure at 80°C, A106GRB steel, 1.5 bar CO <sub>2</sub> , pH 6.6, $\tau$ = 35 Pa. ....	117
Figure 79: SEM & EDS top surface analysis of FeCO <sub>3</sub> layer after 2 days of exposure at 80°C, A106GRB steel, 1.5 bar CO <sub>2</sub> , pH 6.6, $\tau$ = 35 Pa. ....	118
Figure 80: SEM of an etched cross section sample with FeCO <sub>3</sub> layer & microstructure after 2 days of exposure at 80°C, A106GRB steel, 1.5 bar CO <sub>2</sub> , pH 6.6, $\tau$ = 35 Pa. ....	119
Figure 81: Comparison between corrosion rates measured by weight loss (WL) and integrated LPR after 5 days of exposure at 80°C, A106GRB steel, 1.5 bar CO <sub>2</sub> , pH 6.6, B=26 mV/decade, $\tau$ = 35 Pa for the first 2 days, $\tau$ = 535 Pa for another 3 days. ....	120
Figure 82: SEM top surface analysis of FeCO <sub>3</sub> layer after 5 days of exposure at 80°C, A106GRB steel, 1.5 bar CO <sub>2</sub> , pH 6.6, $\tau$ = 35 Pa for the first 2 days, $\tau$ = 535 Pa for another 3 days. ....	121
Figure 83: SEM& EDS top surface analysis of FeCO <sub>3</sub> layer after 5 days of exposure at 80°C, A106GRB steel, 1.5 bar CO <sub>2</sub> , pH 6.6, $\tau$ = 35 Pa for the first 2 days, $\tau$ = 535 Pa for another 3 days. ....	121

Figure 84: SEM & EDS cross section analysis of $\text{FeCO}_3$ layer after 5 days of exposure at $80^\circ\text{C}$ , A106GRB steel, 1.5 bar $\text{CO}_2$ , pH 6.6, $\tau = 35$ Pa for the first 2 days, $\tau = 535$ Pa for another 3 days. ....	122
Figure 85: IFM image of de-scaled sample after 5 days of exposure at $80^\circ\text{C}$ , A106GRB steel, 1.5 bar $\text{CO}_2$ , pH 6.6, $\tau = 35$ Pa for the first 2 days, $\tau = 535$ Pa for another 3 days, Size of the deepest pit $200\mu\text{m}$ in width & $30\mu\text{m}$ in depth. ....	122
Figure 86: Comparison between corrosion rates measured by weight loss (WL), integrated LPR, and penetration rate of the deepest pit on each steel (PR) after 5 days of exposure at $80^\circ\text{C}$ , A106GRB steel, 1.5 bar $\text{CO}_2$ , pH 6.6, $B=26$ mV/decade $\tau = 35$ Pa for the first 2 days, $\tau = 535$ Pa for another 3 days. ....	123
Figure 87: SEM & IFM (after Clarke solution) of Q&T steels (X65I, X70) after 5 days of exposure at $80^\circ\text{C}$ , 1.5 bar $\text{CO}_2$ , pH 6.6, $B=26$ mV/decade, $\tau = 35$ Pa for the first 2 days, $\tau = 535$ Pa for another 3 days. ....	125
Figure 88: SEM & IFM (after Clarke solution) images of normalized steels (X65II, X52, A106GRB) after 5 days of exposure at $80^\circ\text{C}$ , 1.5 bar $\text{CO}_2$ , pH 6.6, $B=26$ mV/decade, $\tau = 35$ Pa for the first 2 days, $\tau = 535$ Pa for another 3 days. ....	126
Figure 89: TCFC final corrosion rate measured by LPR & penetration rate (PR) of the deepest pit on each steel after 5 days of exposure at $80^\circ\text{C}$ , 1.5 bar $\text{CO}_2$ , pH 6.6, $\tau = 35$ Pa for the first 2 days, $\tau = 535$ Pa for another 3 days. ....	127
Figure 90: Mechanism of $\text{FeCO}_3$ formations on normalized steel. ....	130
Figure 91: Mechanism of $\text{FeCO}_3$ formations on Q&T steel. ....	131

Figure 92: LPR measurement corrosion rates (CR) mm/y, five different steels, 3 days of exposure at 80°C, 1.5 bar CO <sub>2</sub> , pH 6.6, B=26 mV/decade, $\tau = 535$ Pa.....	135
Figure 93: LPR measurements with time for Q&T steels. 3 days of exposure at 80°C, 1.5 bar CO <sub>2</sub> , pH 6.6, B=26 mV/decade, $\tau = 535$ Pa. ....	136
Figure 94: SEM top surface analysis of Q&T steel samples (X65I, X70) after 3 days of exposure at 80°C, 1.5 bar CO <sub>2</sub> , pH 6.6, $\tau = 535$ Pa. ....	137
Figure 95: SEM & EDS top surface analysis show that there is no FeCO <sub>3</sub> layer formed on the steel surface after 3 days of exposure at 80°C, Q&T steels, 1.5 bar CO <sub>2</sub> , pH 6.6, $\tau = 535$ Pa.....	138
Figure 96: IFM top surface analysis shows wide shallow pits with 200 $\mu$ m in width & 14 $\mu$ m in depth. There is no FeCO <sub>3</sub> layer formed on the steel surface after 3 days of exposure at 80°C, Q&T steel X65I, 1.5 bar CO <sub>2</sub> , pH 6.6, $\tau = 535$ Pa. ....	139
Figure 97: IFM top surface analysis shows wide shallow pits with 350 $\mu$ m in width & 18 $\mu$ m in depth. There is no FeCO <sub>3</sub> layer formed on the steel surface after 3 days of exposure at 80°C, Q&T steel X70, 1.5 bar CO <sub>2</sub> , pH 6.6, $\tau = 535$ Pa. ....	139
Figure 98: Comparison between corrosion rates measured by integrated LPR, weight loss (WL), and pit penetration rate (PR). After 3 days of exposure at 80°C, Q&T steels, 1.5 bar CO <sub>2</sub> , pH 6.6, $\tau = 535$ Pa.....	140
Figure 99: LPR measurements with time for Normalized hot rolled steel X65II, 3 days of exposure at 80°C, 1.5 bar CO <sub>2</sub> , pH 6.6, B=26 mV/decade, $\tau = 535$ Pa.....	141

Figure 100: SEM top surface analysis of samples after 3 days of exposure at 80°C, NHR steel X65II, 1.5 bar CO <sub>2</sub> , pH 6.6, $\tau = 535$ Pa, No iron carbides remained on the steel surface.....	142
Figure 101: SEM & EDS top surface analysis show that there is no FeCO <sub>3</sub> layer formed on the steel surface after 3 days of exposure at 80°C, NHR steel X65II, 1.5 bar CO <sub>2</sub> , pH 6.6, $\tau = 535$ Pa.....	142
Figure 102: IFM top surface analysis shows large areas of shallow localized corrosion with 1250 $\mu\text{m}$ in width & 18 $\mu\text{m}$ in depth. No FeCO <sub>3</sub> layer formed on the surface after 3 days of exposure at 80°C, NHR steel X65II, 1.5 bar CO <sub>2</sub> , pH 6.6, $\tau = 535$ Pa.....	143
Figure 103: Comparison between corrosion rates measured by integrated LPR, weight loss (W/L), and pit penetration rate (PR). After 3 days of exposure at 80°C, NHR steel X65II, 1.5 bar CO <sub>2</sub> , pH 6.6, $\tau = 535$ Pa.....	143
Figure 104: LPR measurements with time for Normalized steels.....	145
Figure 105: SEM top surface analysis of samples after 3 days of exposure at 80°C, Normalized steels, 1.5 bar CO <sub>2</sub> , pH 6.6, $\tau = 535$ Pa.....	146
Figure 106: SEM & EDS top surface analysis show that there is no FeCO <sub>3</sub> layer formed on the steel surface after 3 days of exposure at 80°C, Normalized steels, 1.5 bar CO <sub>2</sub> , pH 6.6, $\tau = 535$ Pa.....	146
Figure 107: IFM top surface analysis show that there is no FeCO <sub>3</sub> layer formed on the steel surface after 3 days of exposure at 80°C, Normalized steel X52, 1.5 bar CO <sub>2</sub> , pH 6.6, $\tau = 535$ Pa.....	147

Figure 108: IFM top surface analysis show that there is no $\text{FeCO}_3$ layer formed on the steel surface after 3 days of exposure at $80^\circ\text{C}$ , Normalized steel A106, 1.5 bar $\text{CO}_2$ , pH 6.6, $\tau = 535$ Pa.....	147
Figure 109: Comparison between corrosion rates measured by integrated LPR, weight loss (W/L), and pit penetration rate (PR). After 3 days of exposure at $80^\circ\text{C}$ , Normalized steels, 1.5 bar $\text{CO}_2$ , pH 6.6, $B=26$ mV/decade, $\tau = 535$ Pa.....	148
Figure 110: LPR measurements of corrosion rate (CR) in mm/y. 3 days of exposure at $80^\circ\text{C}$ , 1.5 bar $\text{CO}_2$ , pH 6.6, $B=26$ mV/decade, $\tau = 535$ Pa, Quenched and Tempered (Q&T), Normalized steels (N), Normalized hot rolled steels (NHR) . .....	149
Figure 111: Comparison between corrosion rates measured by weight loss (W/L), integrated LPR, pit penetration rate (PR) and carbon content (wt. %). 3 days of exposure at $80^\circ\text{C}$ , 1.5 bar $\text{CO}_2$ , pH 6.6, $\tau = 535$ Pa.....	150
Figure 112: Effect of high wall shear stress on normalized steel.....	152
Figure 113: Effect of high wall shear stress on Q&T and low carbon steels.....	153

## CHAPTER 1: INTRODUCTION

The internal environmental conditions encountered in oil and gas lines can cause severe corrosion of mild steel [1]-[4]. Despite this limitation, mild steel is, in combination with corrosion inhibition, still preferred because it is considered the most cost effective option as compared to more expensive alternative materials, such as stainless steels [5]. The ability to protect mild steel pipelines from corrosion is affected by the water chemistry, fluid velocity, and temperature [6]-[21]; however, the microstructure and chemical composition of steel are also considered to be important variables that affect the resistance of steel to corrosion [22]-[32].

The utility of mild steel in oil and gas pipelines depends on either formation of protective corrosion product layers or use of corrosion inhibitors [5]. However, performance of protective corrosion products and corrosion inhibitors is influenced by chemical composition and microstructure of steel [22], [23], [26], [31], [32]. Although there are no significant effects of alloying elements and microstructure on corrosion rate in environments where protective corrosion product layers do not form, when partially protective iron carbonate layers exist, localized areas of accelerated corrosion occur which vary with metallurgical characteristics [33], [34]. Localized corrosion takes place when small areas selectively experience a higher corrosion rate than the rest of the surface. Localized corrosion is particularly dangerous and can cause failure, over a period of months, of pipelines designed to last for over 40 years. The development of the protective layer on the mild steel surface is highly dependent on surface features and material characteristics [5]. It is known that breakdown of protective layers that form on

mild steel can lead to localized corrosion [35]-[37]. Two mechanisms that can cause attrition of protective layers are chemical attack and mechanical breakdown. If a large area of a mild steel surface is covered by a protective layer, then failure of a small area on that surface is expected to lead to development of a galvanic cell and accelerate corrosion by an electrochemical mechanism [12]. On the other hand, if a small area of the mild steel surface is covered by a protective layer, then excessive turbulence around the obstruction to flow would be expected to increase the mass transfer of species leading to a local loss of material or flow-induced localized corrosion [38]-[44]. Chemical and mechanical effects on localized corrosion are considered to be dependent on water chemistry and flow parameters [38]-[47]; however, chemical composition and microstructure of steel play a major role in localized corrosion mechanisms in CO<sub>2</sub> corrosion.

Many studies have discussed the influence of chemical composition and microstructure of carbon and low alloy steels in CO<sub>2</sub> corrosion [22]-[30]; however, most of these studies did not give a clear explanation relating microstructure and chemical composition of steel to localized corrosion mechanisms in CO<sub>2</sub> corrosion.

## CHAPTER 2: LITERATURE REVIEW

Mild steel can rapidly corrode when exposed to CO<sub>2</sub> corrosion environments.

There are many factors that need to be considered to understand the mechanism of CO<sub>2</sub> corrosion and performance of mild steel, these are briefly described below [7], [8], [15], [16].

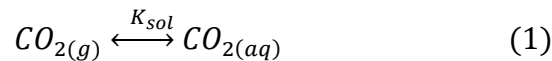
### 2.1 CO<sub>2</sub> Corrosion

The CO<sub>2</sub> corrosion process can be described by the chemical reactions of species in bulk solution, electrochemical reactions of species on the steel surface, and mass transport of species from bulk solution to and away from the steel surface.

#### 2.1.1 Chemical Reactions

Water chemistry is considered one of the important parameters that affect CO<sub>2</sub> corrosion.

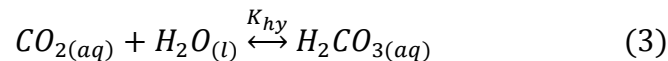
When CO<sub>2</sub> is dissolved in water, it can be described as aqueous CO<sub>2</sub>, “CO<sub>2(aq)</sub>”, with a molar concentration in solution designated by “[CO<sub>2</sub>]” [8]:



Where  $K_{sol}$  is the temperature-dependent solubility constant, which is defined as:

$$K_{sol} = \frac{[CO_2]}{pCO_2} \quad (2)$$

The dissolved, CO<sub>2</sub>, will then partially hydrate, forming carbonic acid:



Where  $K_{hy}$  is the corresponding equilibrium constant for hydration, which is defined as follows:

$$K_{hy} = \frac{[H_2CO_3]}{[CO_2]} \quad (4)$$

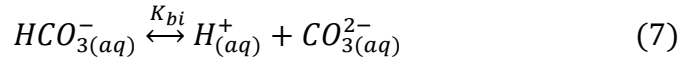
The generated carbonic acid partially dissociates to give hydrogen ion and bicarbonate ion:



Where  $K_{ca}$  is the equilibrium constant of the reaction, which is written as follows:

$$K_{ca} = \frac{[H^+].[HCO_3^-]}{[H_2CO_3]} \quad (6)$$

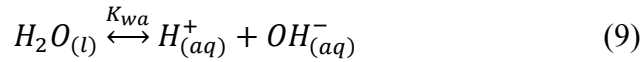
Bicarbonate ions then partially dissociate again into carbonate and hydrogen ions:



Where  $K_{bi}$  is the equilibrium constant, which is defined as:

$$K_{bi} = \frac{[H^+].[CO_3^{2-}]}{[HCO_3^-]} \quad (8)$$

Hydrogen ions can also be derived from dissociation of water:



Where  $K_{wa}$  is the equilibrium constant and is defined as:

$$K_{wa} = [H^+].[OH^-] \quad (10)$$

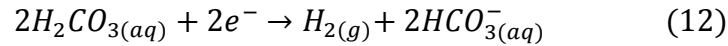
### 2.1.2 Electrochemical Reactions

The electrochemical reactions that occur on the steel surface involve the cathodic evolution of hydrogen (reduction) and the anodic dissolution of iron (oxidation). The cathodic evolution of hydrogen can be described by the following half-reactions [8]:

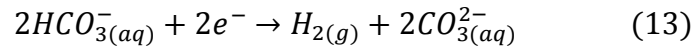
- Reduction of hydrogen ions generated by the partial dissociation of  $H_2CO_3$ ,  $HCO_3^-$  and  $H_2O$ , as shown by the equilibrium reactions (5), (7) and (9):



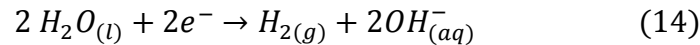
- The direct reduction of  $H_2CO_3$ :



- The direct reduction of bicarbonate  $HCO_3^-$  at  $pH > 7$ , where it is a dominant species [16]:



- The direct reduction of water, that can be significant if  $pH > 6$  and low partial pressure of  $CO_2$ ,  $pCO_2 \ll 1$  [6]:



The anodic half-reaction is the oxidative dissolution of iron:



### 2.1.3 Mass Transport

The mass transport rates of the reducible species and dissolved metal ions to and away from the steel surface can control the rate of electrochemical reactions. In  $CO_2$  corrosion, mass transport occurs *via* molecular diffusion, within a diffusion boundary layer, and *via* convection, due to the turbulent movement of solution near the metal surface [8].

In the corrosion process, the concentration of reducible hydrogen ions is depleted at the steel surface and at the same time the concentration of ferrous ion increases (Equation 11 and Equation 15 combined). Consequently, this process is governed, and limited, by the mass transport of reducible hydrogen ions to the steel surface. Carbonic acid (Equation 12) and bicarbonate ions (Equation 13) also react with the metal to release electrons for the corrosion process and are influenced by mass transport, but, because the

chemical reaction of the dissolved CO<sub>2</sub> to form carbonic acid (Equation 3) is slower than the diffusion rate, the chemical reaction to form carbonic acid is the rate determining step for these two species [8].

#### 2.1.4 Iron Carbonate as Corrosion Product

The carbonate anions (CO<sub>3</sub><sup>2-</sup>) which form by the dissociation processes described above, react with dissolved ferrous ion (Fe<sup>2+</sup>) to form FeCO<sub>3</sub> as a corrosion product. This FeCO<sub>3</sub> heterogeneously precipitates at the steel surface; its protectiveness against corrosion is dependent on the precipitation rate. When the precipitation/formation rate of FeCO<sub>3</sub> on the steel surface exceeds the corrosion rate (oxidative dissolution of iron), an adherent and dense FeCO<sub>3</sub> layer can form on the steel surface [15], [16], [20], [21]. The precipitation rate of FeCO<sub>3</sub> is also dependent on the CO<sub>2</sub> pressure and temperature. The precipitation rate is directly influenced by the saturation value (*S*) of FeCO<sub>3</sub>, which is defined by Equation 16:

$$S = \frac{[Fe^{2+}] \cdot [CO_3^{2-}]}{K_{sp}} \quad (16)$$

Where *K<sub>sp</sub>* is the solubility limit. The saturation value (*S*) has to be >1 to have supersaturation with respect to iron carbonate that can lead to the formation of an adherent and dense FeCO<sub>3</sub> layer. The carbonate ion concentration is directly related to the solution pH by Equation 7.

## 2.2 Flow Effects

The influence of flow on CO<sub>2</sub> corrosion is dependent on the condition of the steel surface. When no FeCO<sub>3</sub> layer is formed on the steel surface (at pH4 where *S*<1), turbulent flow increases the rate of species transport from and towards the steel surface

[7], [8]. This fast movement of species increases the rate at which hydrogen ion is replenished and generated ferrous ion is removed from the surface, which in turn increases the corrosion rate. When  $\text{FeCO}_3$  is formed on the steel surface (at higher pH where  $S > 1$ ), the influence of flow becomes insignificant [7]. However, flow effects can cause a breakdown of  $\text{FeCO}_3$  corrosion product layers that can be particularly deleterious at local areas such as valves, expansions, and bends; where local increases in wall shear stress are observed [13], [38]. This local breakdown of the  $\text{FeCO}_3$  layer can also contribute to localized corrosion, which has the potential to be more dangerous than uniform corrosion [35]-[37]. Many studies have discussed the effect of flow on  $\text{FeCO}_3$  corrosion product layers [38]-[47]. However, mechanisms relating to flow effects remain poorly understood. Some studies show that the  $\text{FeCO}_3$  corrosion product layer can be removed by high flow rates [41], [45]. On the other hand, other studies reported that the wall shear stress is too low under normal operating parameters in oil and gas pipelines to remove an  $\text{FeCO}_3$  layer [46], [47]. One study utilized tensile testing equipment to remove previously formed  $\text{FeCO}_3$  from a steel surface. This study reported that the adhesion strength of the  $\text{FeCO}_3$  was “measured to be of the order of 10 MPa” [46]. Another study discussed the effect of high flow rate on the protectiveness of the  $\text{FeCO}_3$  layer and how it can be related to its mechanical properties [41]. According to that study, the  $\text{FeCO}_3$  layer can be removed due to “intrinsic” stress contributions, i.e., stresses within the  $\text{FeCO}_3$  corrosion product itself, rather than purely due to application of “extrinsic” stress, such as wall shear stresses, which alone are insufficient to cause breakdown and loss of  $\text{FeCO}_3$  layers. The same study also reported that the local pressure changes caused by turbulent

flow can contribute to the breakdown of the  $\text{FeCO}_3$  layer. In another study, it was shown that changes in pressure caused by flow can increase the tendency of  $\text{FeCO}_3$  layer to crack; a depiction of this mechanism is shown in Figure 1 [45]. The same study also reported that low wall shear stress, generated by a submerged jet impingement, can cause localized corrosion when initiated from an artificial pit even at wall shear stress values as low as 0.2 Pa [45].

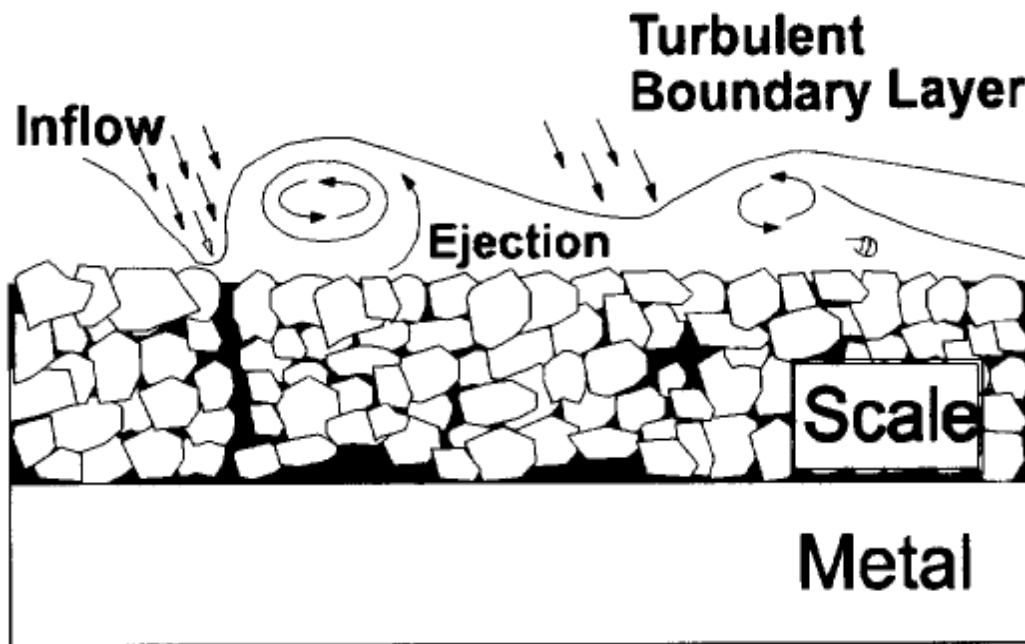


Figure 1: Diagram of the destruction mechanisms for surface layer caused by pressure changes near the steel surface [45].

### 2.3 Steel Composition and Microstructural Effects

In the oil and gas industry, the design criteria of pipeline materials are mainly focused on mechanical properties, such as strength, weldability, and toughness, rather

than corrosion resistance [5]. The mechanical properties of pipeline materials are dependent on microstructure, which is determined by its chemical composition and thermo-mechanical treatment [48], [54]. The microstructure of steel is considered to have an important effect on  $\text{FeCO}_3$  layer and inhibitor layer characteristics in  $\text{CO}_2$  environments.

### *2.3.1 Bare Steel as a Corroding Substrate*

In  $\text{CO}_2$  environments, the  $\text{FeCO}_3$  layer can form if the saturation of  $\text{FeCO}_3$  in the bulk is sufficiently high [15], [16]. The  $\text{FeCO}_3$  layer can be adherent; however, it is uncertain if it will have any protective properties [15]. Both lab experiments and field experience have shown that the protective properties and the adherence of such corrosion products can vary for different mild steels with the same mechanical properties [22], [30]. Many studies [21], [22], [26], [32], showed that the normalized steels, which have ferrite/pearlite (F/P) microstructure, behave differently compared to quenched and tempered (Q&T) steels, which mostly have tempered martensite microstructure. Carbides are thought to play a major role on the protective properties and adherence of the  $\text{FeCO}_3$  layer.

In F/P steels, pearlite exists as a lamellar structure composed of alternating layers of ferrite and iron carbide (cementite). When steel is exposed to the  $\text{CO}_2$  environment, the ferrites from the pearlite will become anodic, and rapidly corrode, while the iron carbides are left intact. When the concentration of ferrous ions becomes high enough to achieve supersaturation condition of  $\text{CO}_2$  and the flow becomes stagnant, such as in the cavities

between iron carbide lamellae, the  $\text{FeCO}_3$  layer rapidly forms, and the iron carbide lamellae assist its retention on the steel surface, see Figure 2.

The distribution of F/P has a significant effect on the performance of the steel in  $\text{CO}_2$  corrosion. If the F/P distribution is not homogenous, the performance of the steel will be decreased. One study showed that the performance of J55, which has bands of F/P structure, can be improved by increasing the carbon content and normalization heat treatment [29]. Increasing the carbon content will give steel with homogeneous and fine globular grains that is more protective than the bands of F/P.

Corrosion and related phenomena from martensitic Q&T steels remain poorly understood. *Martensitic* Q&T steel contains fine grains; consequently, it is difficult to resolve its microstructure by optical microscopy. However, higher magnification electron microscopy can be used. The pearlite ratio in normalized steels is dependent on carbon content; however, martensite can form even with almost carbon-free steel. According to one study there is no clear explanation about how the microstructural characteristics of Q&T martensitic steels affect the development of the  $\text{FeCO}_3$  layer [22]; the authors noted that the corrosion rate of Q&T steels with a large population of small grain carbides is higher than for those with larger spheroidal carbides. The authors stated that “the large number of small iron carbides can stick together and lead to formation of non-protective  $\text{FeCO}_3$  layers with exposed, and conductive, carbides”. On the other hand, they observed the lowest corrosion rates on Q&T steels containing no iron carbides, but they did not give clear explanations about how the  $\text{FeCO}_3$  layer adheres to the surface. In another study[55], the authors discussed the effect of supersaturation of  $\text{CO}_2$  with different

ferrous ion and bicarbonate concentrations on a martensitic X65 steel at 25°C and higher pH (pH > 6.8), without consideration of its microstructure. They speculated that the relative inability to form protective FeCO<sub>3</sub> layers under these conditions could be due to an iron carbide effect.

There are other studies, [22], [33], [55], [56], [57] that evaluated the effect of Cr content on the FeCO<sub>3</sub> layer and found that Cr addition can improve the protective properties of mild steel against corrosion. The chromium oxide (Cr<sub>2</sub>O<sub>3</sub>) that forms on the steel surface can cover the voids between FeCO<sub>3</sub> crystals and improve the protective properties of such steels. According to one study [33], the authors noted at around 80°C, pH 5.8, and flow rate higher than 4.0 m/s, mild steel without Cr addition suffers severe mesa attack, where mesa attack is defined as a small exposed area that will be anodic to the surrounding area protected by an FeCO<sub>3</sub> layer (galvanic corrosion). They speculated that if chromium content is greater than 0.5%, Cr<sub>2</sub>O<sub>3</sub> can be easily reformed on locally corroded areas.

From previous studies it can be concluded that the size of ferrite and pearlite grains, and also the size, shape, and distribution of iron carbides, can be considered as an important factors that influence corrosion. Heat treatment and chemical composition of steel are the main factors that need to be considered to control the iron carbide formation on mild steel. The steel surface condition (freshly polished or corroded) also can be considered as an important factor.

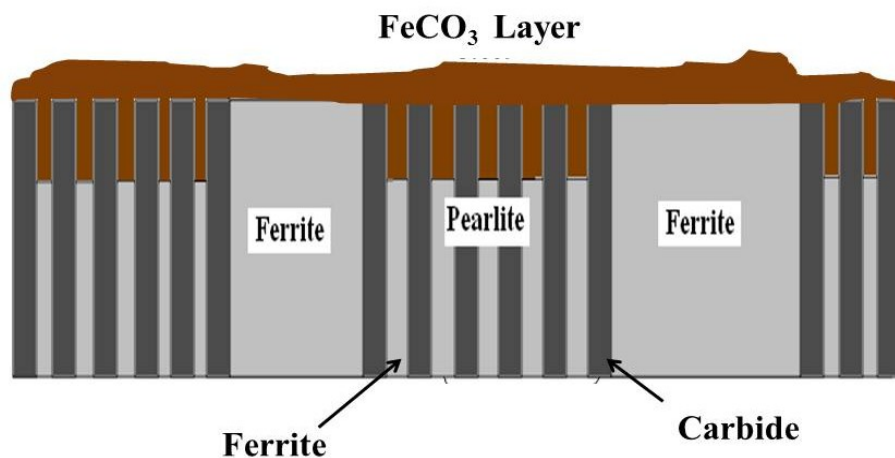


Figure 2: Mechanism of FeCO<sub>3</sub> development for F/P steels.

### 2.3.2 Corrosion Inhibitors and Metallurgical Characteristics

The use of corrosion inhibitors, usually nitrogen-containing surface active compounds that preferentially adsorb at a metal surface, are the most effective method to control mild steel corrosion in the oil and gas industry. The mechanism of inhibitor adsorption is also poorly understood. One study [31] discussed the effect of microstructure and alloying elements of mild steels on CO<sub>2</sub> corrosion with corrosion inhibitor behavior. The authors found that cathodic corrosion inhibitor efficiency can be detrimentally affected if the steel structure is primarily cementite-type rather than ferrite; however, inhibitor efficiency on a virgin steel surface is high. They state that when mild steel is corroded more iron carbides will be exposed which lead to an increase in the cathodic area. The large cathodic areas can detrimentally affect the inhibitor efficiency if the actual type of mild steel is not considered. There is no clear explanation how copper with carbon can affect inhibitor efficiency. Another study [7] found that increasing the Cr content can detrimentally affect the efficiency of a corrosion inhibitor; the authors

proposed that the chromium enrichment of the  $\text{FeCO}_3$  layers and the inhomogeneous distribution of chromium in ferrite and pearlite could be the reason for poor inhibitor performance.

## CHAPTER 3: HYPOTHESIS AND RESEARCH OBJECTIVES

### 3.1 Hypothesis

The central hypothesis that was tested is that the protective properties and adherence of protective layers on mild steel are dependent on the carbide content, grain size/distribution and related metallurgical characteristics, i.e., on the microstructure and chemical composition of mild steel.

### 3.2 Research Objective

The primary objective of this research is to study and model CO<sub>2</sub> corrosion phenomena as related to metallurgical characteristics of mild steel, with a focus on mechanisms that lead to localized corrosion.

Specifically, the objectives of this study are as follows:

- Select five different pipeline steels with different chemical composition and microstructure and investigate the effect of their metallurgy on the properties of formed FeCO<sub>3</sub> corrosion product layer and related corrosion phenomena.
- Relate CO<sub>2</sub> corrosion to metallurgical characteristics of mild steel, with a focus on flow and mechanisms that lead to localized corrosion.
- Model corrosion phenomena as relating to the metallurgical characteristics of mild steel.

## CHAPTER 4: METALLOGRAPHIC ANALYSIS

### 4.1 Introduction

Any steel with carbon content between 0.02wt% and 0.3wt% is considered mild steel or low carbon steel. To understand the microstructure of any steel, the chemical composition and/or the type of manufacturing and heat treatment (mechanical and thermodynamic processes) should be determined.

The pipeline steels have different grades and different mechanical properties because they contain different chemical compositions. The microstructure of the steels can be formed to more than one phase depending on its chemical composition and previous heat treatment. Many different microstructures, such as ferrite/pearlite, tempered martensite, and bainite can be obtained by controlling the cooling rate of hot steel from the austenite temperature. The controlled cooling rate process determines the type of heat treatment techniques that are used to achieve a desired microstructure. As such, these heat treatment processes are normalizing, quenching/tempering (Q&T), spheroidizing, full annealing, and process annealing. From the Fe-C phase diagram, shown in Figure 3, for mild steel or low carbon steel, the phase that is present above the critical eutectoid temperature  $A_3$  is austenite. When alpha iron is heated above the critical eutectoid temperature  $A_3$ , the iron phase will be transformed from a body-centered cubic (BCC) to a face-centered cubic (FCC) unit cell structure to become gamma iron or austenite. The austenite can dissolve as much as 2.04% by mass carbon at 1,146 °C. When steel cools down below the  $A_3$  transformation point, ferrite grains start to form. The remaining austenite becomes richer in carbon. When the temperature reaches the  $A_1$  transformation

line at  $727^{\circ}\text{C}$ , the remaining austenite will be transformed to pearlite. Here, the resulting microstructure is shown by light grains of ferrite and dark grains of pearlite, which both have BCC structure. However, if the steel cooled rapidly from austenite, the austenite will not have sufficient time to transform into ferrite and pearlite. Here, the resulting structure will be martensite [59].

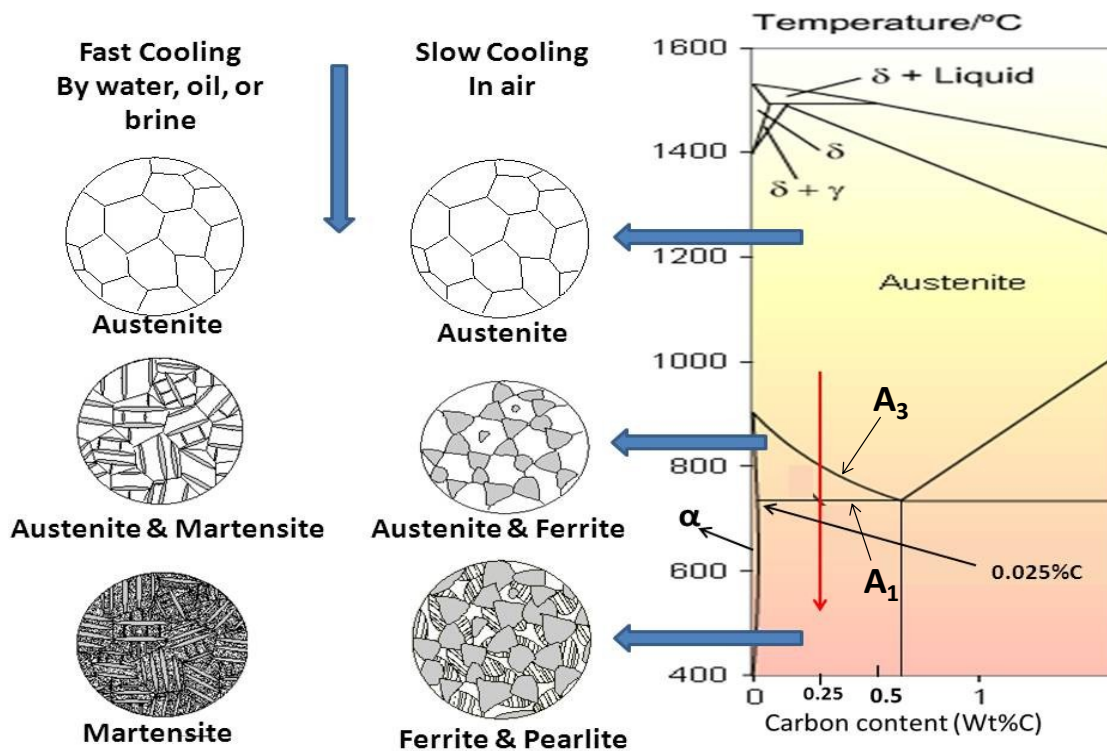


Figure 3: Fe-C phase diagram shows the phase transformation from austenite to ferrite/pearlite (slow cooling) and from austenite to martensite (fast cooling), where; white = ferrite, gray = pearlite [60].

Continuous cooling transformation (CCT) diagrams are constructed to determine the microstructure of steel during continuous cooling from austenite. CCT diagrams determine the structure of steel at different temperatures as a function of time. The cooling rate of steel determines the desired microstructure, which can be martensite at fast cooling rates, bainite, and/or ferrite/pearlite at lower cooling rates. The CCT diagrams are affected by the carbon content (wt% C). However the molybdenum content (wt% Mo) of the steel can also affect the CCT diagram. Increasing wt% C and wt% Mo shifts the transformation curves shown in the CCT diagrams to the right side. Figure 4 and Figure 5 [61] show the structural change for 0.4wt% C steel during a continuous fast cooling rate from austenite to martensite, and this type of cooling is called quenching. Here, after increasing the temperature to about  $50^{\circ}\text{C}$  above  $A_3$ , the steel is cooled very quickly by oil, water, or brine, depending on the carbon content of steel and the desired martensitic microstructure is formed. Figure 6 and Figure 7 show the structural change for 0.4wt% C steel during a continuous slow cooling rate from austenite to ferrite/pearlite, and this type of cooling is called normalizing. Here, after increasing the temperature to about  $50^{\circ}\text{C}$  above  $A_3$ , the steel cooled slowly at room temperature.

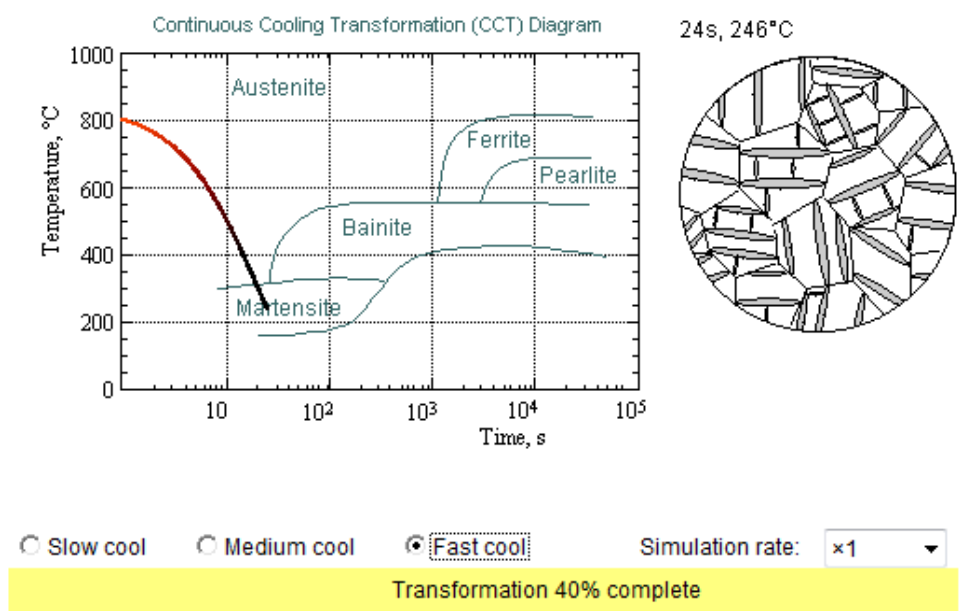


Figure 4: CCT diagram for 0.4wt% C steel shows the phase transformation from austenite to martensite in the fast cooling processes.

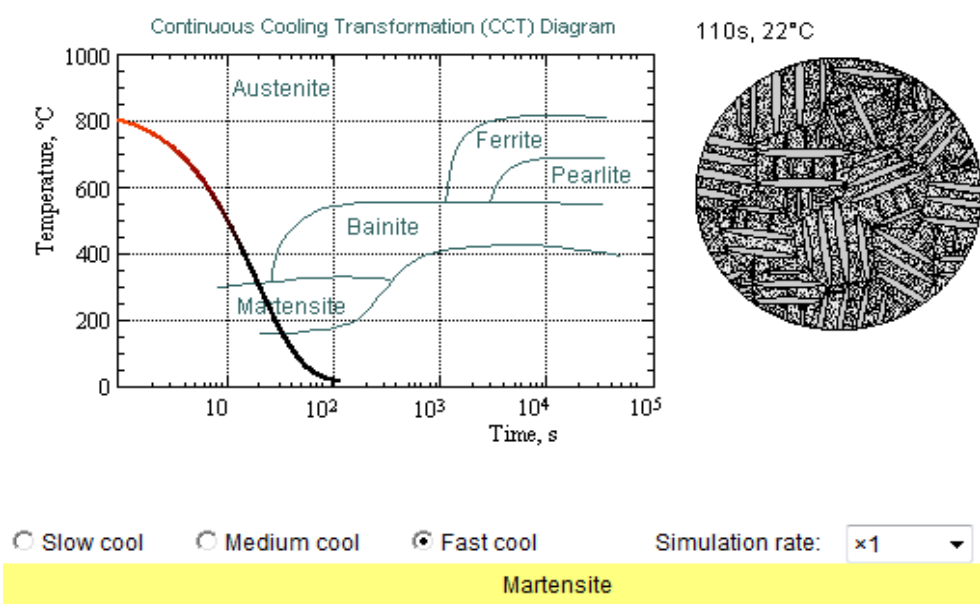


Figure 5: CCT diagram for 0.4wt% C steel shows the final obtained microstructure (martensite) in the fast cooling processes.

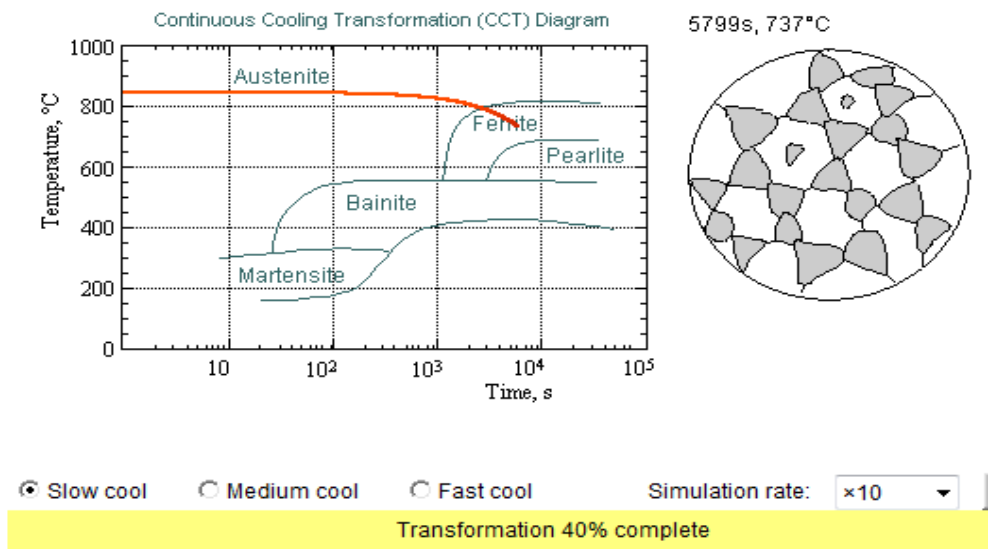


Figure 6: CCT diagram for 0.4wt% C steel shows the phase transformation from austenite to ferrite in the slow cooling processes.

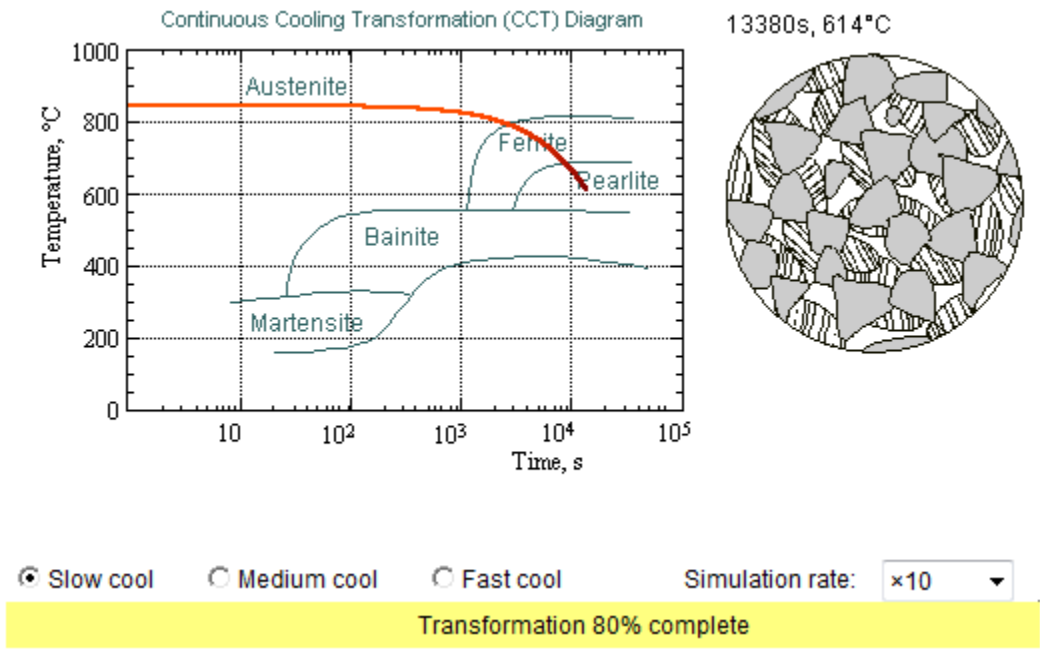


Figure 7: CCT diagram for 0.4wt% C steel shows the phase transformation from austenite to ferrite/pearlite in the slow cooling processes.

## 4.2 Chemical Composition of Chosen Steels

The steels to be tested were X52, X65I, X65II, X70, and A106GRB. The steels were chosen in order to obtain corrosion and iron carbonate layer formation information from steels with different microstructural and compositional characteristics. The steels were submitted to Laboratory Testing Inc. [62] for chemical composition evaluation and three of them (X65I, X65II, X70) were found to be in conformance to UNS G15130. A106GRB was in conformance to UNS G10290, and X52 was in conformance to UNS G15250. The Unified Numbering System (UNS) of Ferrous Metals and Alloys UNS [63] determines the alloying composition requirements of the *American Iron and Steel Institute* (AISI) and *Society of Automobile Engineers (SAE) carbon and alloy steels*; the requirements for UNS designation vs. sample analysis are shown in Table 1 and Table 2.

Table 1: Chemical Composition of X65I, X65II, and X70 Steels.

(UNS G15130)					
Element	Requirements		X65I wt%	X65II wt%	X70 wt%
	Min	Max			
Al			0.037	0.024	0.033
C	0.10	0.16	0.14	0.07	0.071
Cr			0.14	0.052	0.23
Cu			0.12	0.27	0.018
Mn	1.10	1.40	1.18	1.31	1.38
Mo			0.14	0.026	0.094
Ni			0.38	0.10	0.092
P		0.04	0.010	0.008	0.011
S		0.05	0.004	0.006	0.004
Si			0.24	0.27	0.13
Ti			0.005	0.016	0.007
V			0.056	0.025	0.05
Fe	Balance				

Table 2: Chemical Composition of A106GRB and X52 Steels.

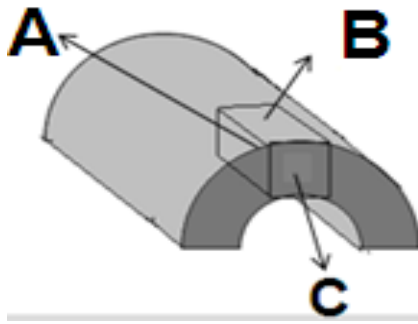
Element	A106GRB (UNS G10290)			X52 (UNS G15250)		
	Requirements		wt%	Requirements		wt%
	Min	Max		Min	Max	
Al			0.031			0.056
C	0.25	0.31	0.27	0.23	0.29	0.26
Cr			0.069			0.037
Cu			0.089			0.006
Mn	0.60	0.90	0.82	0.80	1.10	1.01
Mo			0.003			0.004
Ni			0.049			0.024
P		0.03	0.014		0.04	0.010
S		0.05	0.003		0.05	0.012
Si			0.27			0.023
Ti			0.002			0.002
V			0.003			0.063
Fe	Balance					

#### 4.3 Microstructure of Chosen Steels

Three sections from different planes were cut from each material, Figure 8, and mounted in Bakelite\* for metallographic analysis using polishing and etching procedures described in APPENDIX A [64]. Metallurgical studies were conducted using an Alicona Infinite Focus Microscope (IFM) with subsequent data analysis with ImageJ software.

---

\*Trade name for plastic mounting material. Bakelite is a synthetic resin. The Bakelite powder is used with specimens for mounting of samples.



a-Samples cut from 3 orientations



b-Mounted in Bakelite

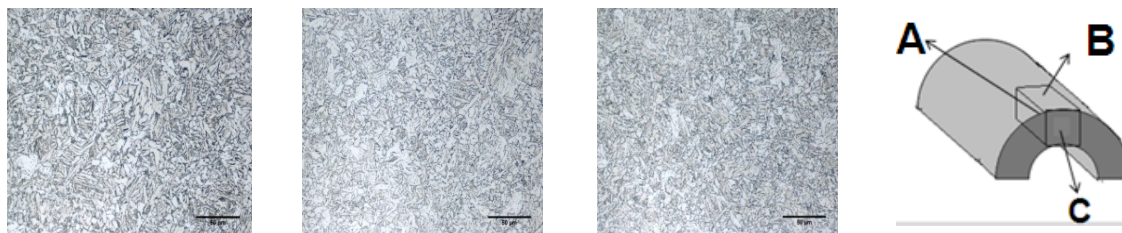
Figure 8: Preparation of samples for metallographic analysis.

Micrograph images of all steels had previously been taken by Chevron Corp [65]. The acquired micrograph images taken using the ICMT's Infinite Focus Microscopy (IFM) were then compared with those obtained by Chevron Corp using similar analytical techniques to demonstrate and validate our 'in-house' ability to determine the microstructure of the steels. Specific procedures used in microstructural analysis are described in APPENDIX A. Micrograph images of cross-sectioned samples were also analyzed with the same techniques after using polishing and etching procedures, also described in APPENDIX A, to show the relationship between the formed  $\text{FeCO}_3$  layer(s) and microstructure of the steel.

The micrograph images were examined to determine the microstructure of these steels by comparing the obtained images with a collection of micrographs of various materials which have been contributed by people working in the field of materials science and technology, through the Micrograph Library, University of Cambridge [66] and by review of the obtained results with S. Smith[67]. The microstructures of these steels are described below:

X65I: This steel contains a medium amount of carbon (0.14wt% C). The microstructure of planes A, B, and C are the same as shown in Figure 9. As shown in Figure 10, the structure of this steel is similar to the martensite structure that is shown in Figure 5. The microstructure of X65I is quenched and tempered (Q&T) and consists of tempered martensite. Although the tempered martensite is not expected with 0.14wt% C, the 0.14wt% Mo shifts the transformation curves shown in the CCT diagrams to the right side and facilitates the formation of tempered martensite, see Figure 4 and Figure 5 [61]. Here, the carbon that is trapped in the martensite is released during tempering to increase ductility and relieve the internal stresses. Releasing the carbon is conducted by increasing the temperature of the steel below the  $A_1$  transformation temperature, Figure 3, and then cooling it in air (tempering).

X70: This steel contains a very low amount of carbon (0.071wt%C). The microstructure of planes A, B, and C are the same as shown in Figure 11. As shown in Figure 12, the structure of this steel is also similar to the martensite structure that is shown in Figure 5. The microstructure of X70 is quenched and tempered (Q&T) and consists of tempered martensite. As shown before, the curves of the CCT diagrams of steels with low carbon content will be shifted to the left side, which perhaps prevents the formation of martensite at rapid cooling rates. However, some addition of Mo can shift the curves to the right and facilitate the formation of martensite [61]. Table 1 shows that Mo content in X65I and X70 is much higher than other steels. The microstructure of X65I and X70 are slightly different; the difference could be due to the different carbon content.



Plane A.

Plane B.

Plane C.

Figure 9: X65I steel, plane A, B, C microstructures.

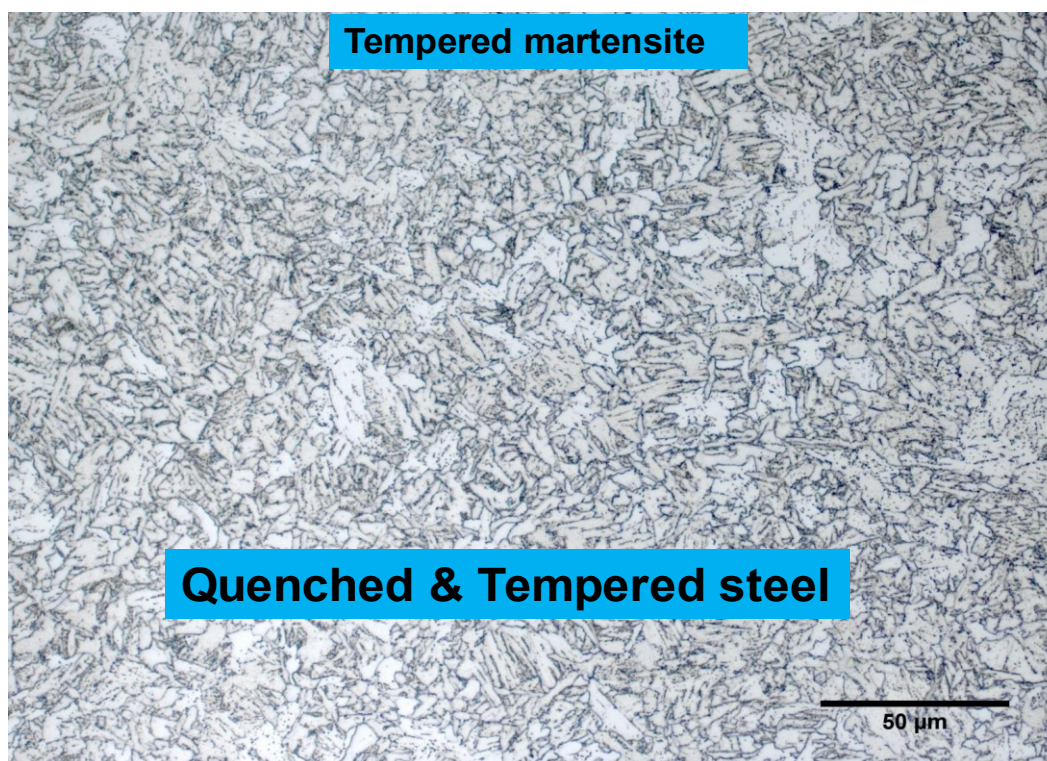
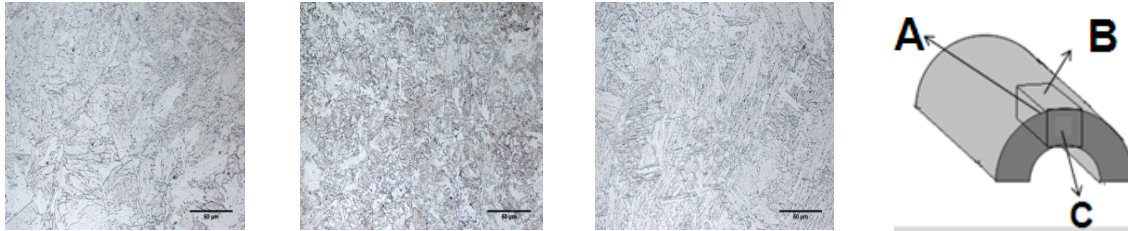


Figure 10: X65I steel, microstructure consists of tempered martensite.



Plane A.

Plane B.

Plane C.

Figure 11: X70 steel, plane A, B, C microstructures.

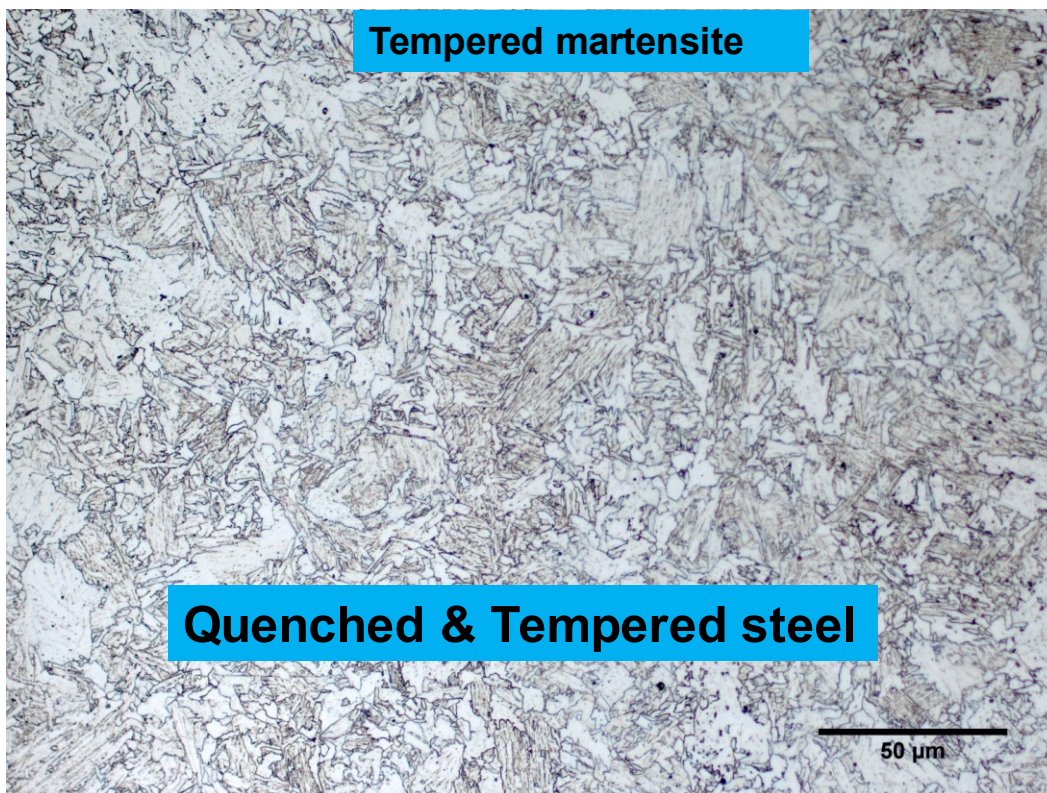


Figure 12: X70 steel, microstructure consists of tempered martensite.

X65II: This steel contains a very low amount of carbon (0.07 wt% C). As shown in Figure 13, there are significant differences in the microstructure between planes B, C, and plane A. As shown in Figure 14, plane B and plane C consist of light grains of ferrite with some dark pearlite. The structure of this plane is similar to the ferrite/pearlite

structure shown in Figure 7. However, plane A consists of thick, light colored bands of ferrite and thin, dark colored bands of pearlite, which indicate that the steel was probably hot rolled, followed by air cooling to room temperature, Figure 14. The microstructure of X65II is normalized hot rolled steel. As shown in Figure 14, some of the pearlite bands contain yellow grains, which could be related to Cu or Mn alloying elements.

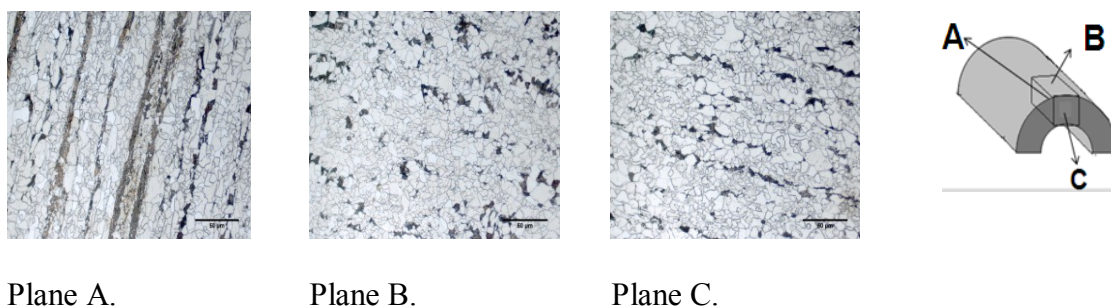
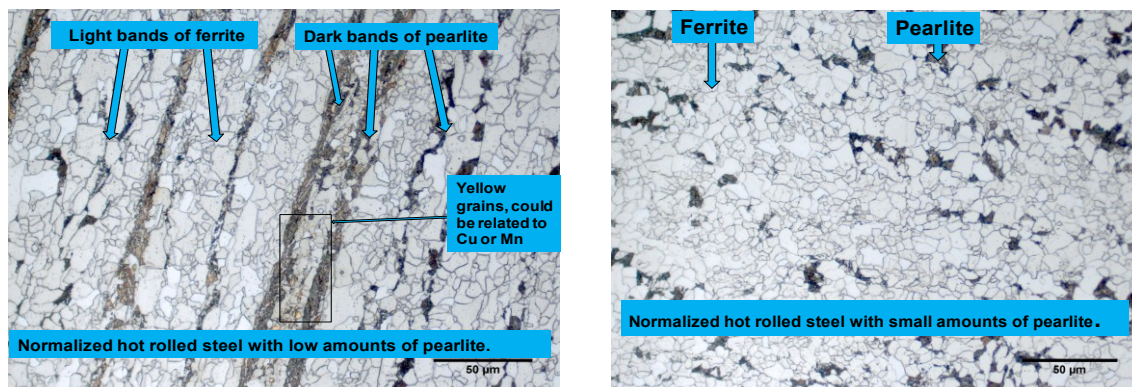


Figure 13: X65II steel, plane A, B, C microstructures.



Plane-A steel, microstructure consists of thick light colored bands of ferrite and thin dark colored bands of pearlite.

Plane-B steel, microstructure consists of small bright ferrite with low amounts of pearlite.

Figure 14: X65II steel, there is difference in the microstructure between plane A and B.

X52: This steel contains higher amounts of carbon (0.26 wt% C). The microstructure of planes A, B, and C are the same as shown in Figure 15. As shown in Figure 16, the structure of this steel is similar to the ferrite/pearlite structure that shown in Figure 7. The steel was normalized by increasing its temperature to 50°C above  $A_3$  then letting it cool in air. The microstructure of X52 consists of large, dark grains of pearlite surrounded by large, light grains of ferrite as shown in Figure 16.

A106GRB: This steel contains higher amounts of carbon (0.27 wt% C). The microstructure of planes A, B, and C are the same as shown in Figure 17. As shown in Figure 18, the structure of this steel is also similar to the ferrite/pearlite structure shown in Figure 7. The microstructure of A106GRB consists of large, dark grains of pearlite surrounded by large, light grains of ferrite as shown in Figure 17.

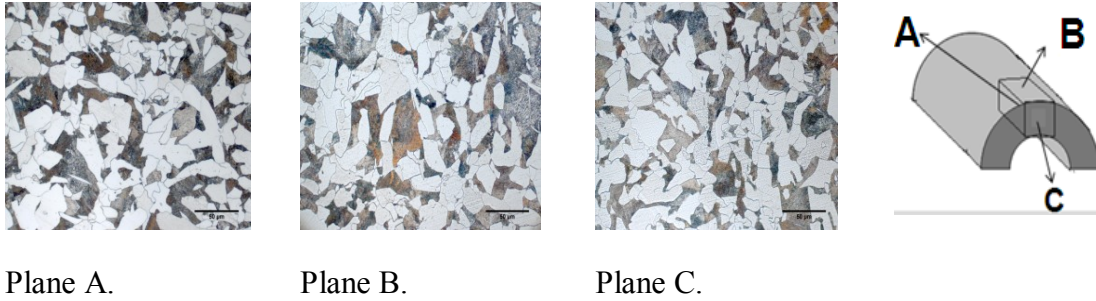


Figure 15: X52 steel, plane A, B, C microstructures.

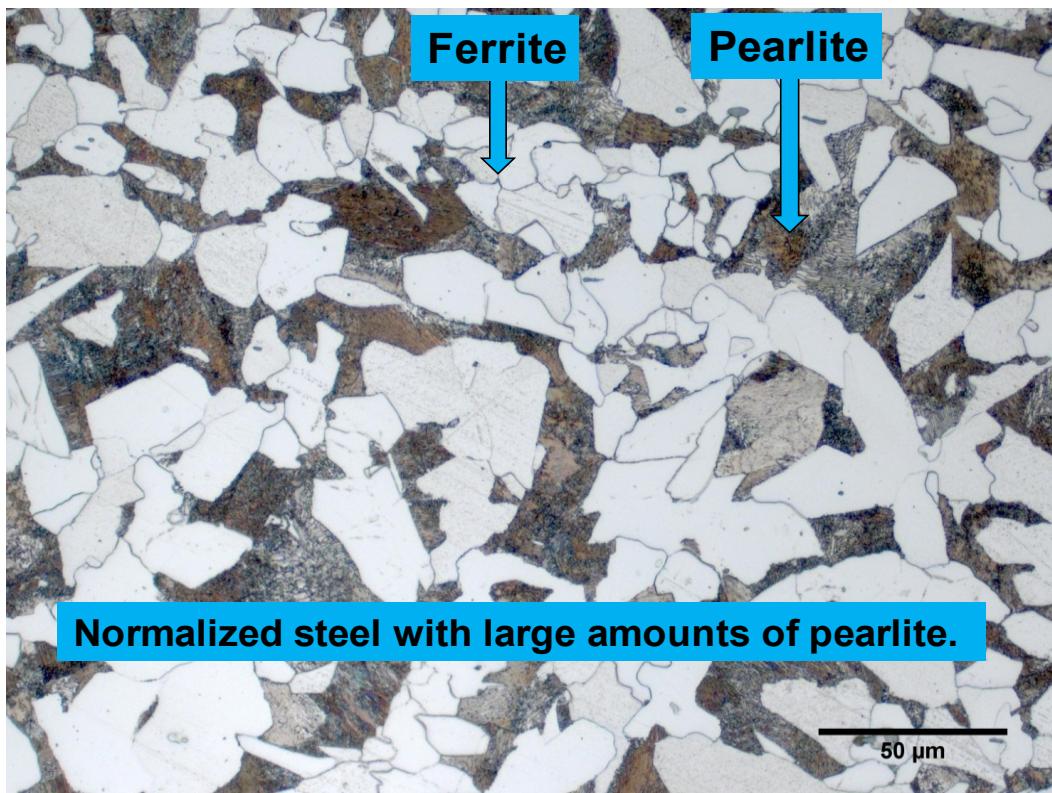


Figure 16: X52 steel, microstructure consists of large dark pearlite surrounded by large bright ferrite.



Plane A.

Plane B.

Plane C.

Figure 17: A106GRB, plane A, B, C microstructures.

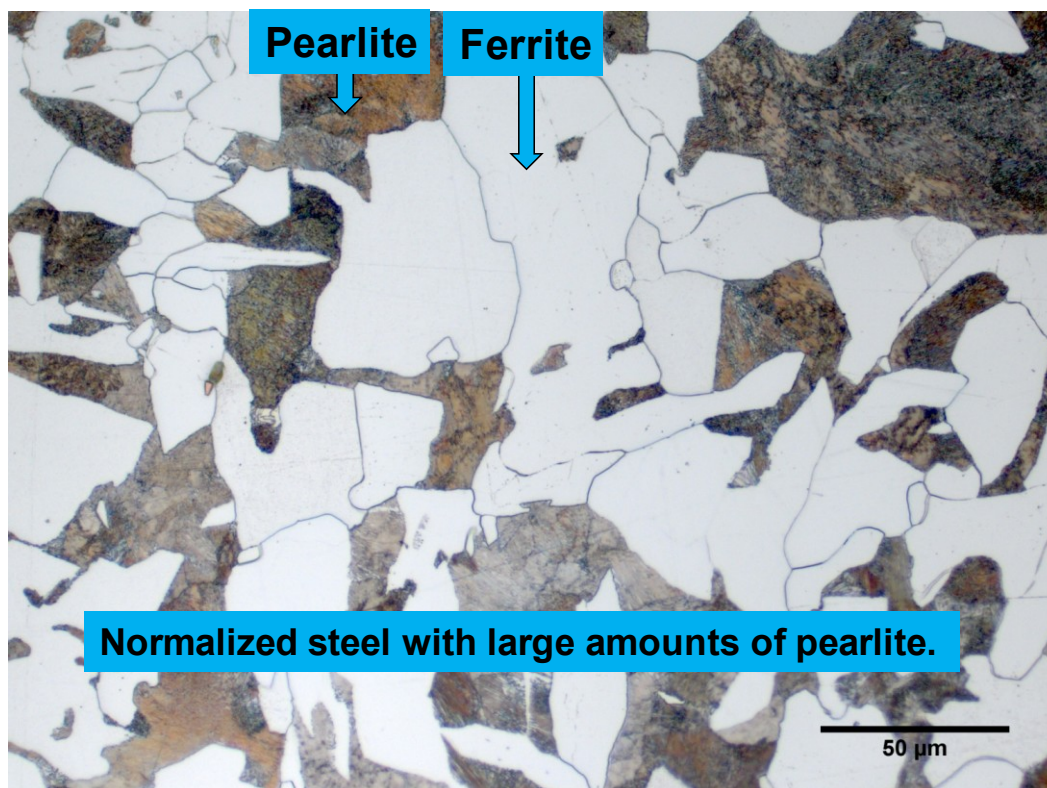


Figure 18: A106GRB steel, microstructure consists of large dark pearlite surrounded by large bright ferrite.

As shown above, different steel microstructures are obtained for experimentation. There are two steels with large amounts of pearlite, one ferritic steel with a small amount of pearlite and two Q&T steels. As S. Smith [67] commented, this broad variety of

microstructures provides a good base to study the possibility of localized corrosion, so these steels were used during the next phase of corrosion tests. A summary of chosen steel microstructures with heat treatment is shown in Table 3.

Table 3: Microstructure and Heat Treatment of the Tested Steels.

Steel	Carbon content wt%	Microstructure	Heat treatment
X65I	0.14	Tempered Martensite	Quenched & Tempered
X70	0.071		
X65II	0.07	Ferrite with small amount of pearlite	Normalized hot rolled
X52	0.27	Large dark grains of pearlite surrounding by large light grains of ferrite	Normalized
A106GRB	0.26		

#### 4.4 Grain Size

In addition to microstructure, the grain sizes of these steels, which are thought to have an effect on corrosion behavior [68], were determined using two different methods. These are summarized below and further described in APPENDIX B.

##### 4.4.1 Intercept Method, ASTM E112 Standard

The intercept method [69] is also known as the Heyn Method. The basic steps to determine grain size are described as:

- 1- Apply number of lines of known total length L, see APPENDIX B, Figure B1.
- 2- Count total intercepts between test lines and grain boundaries P.

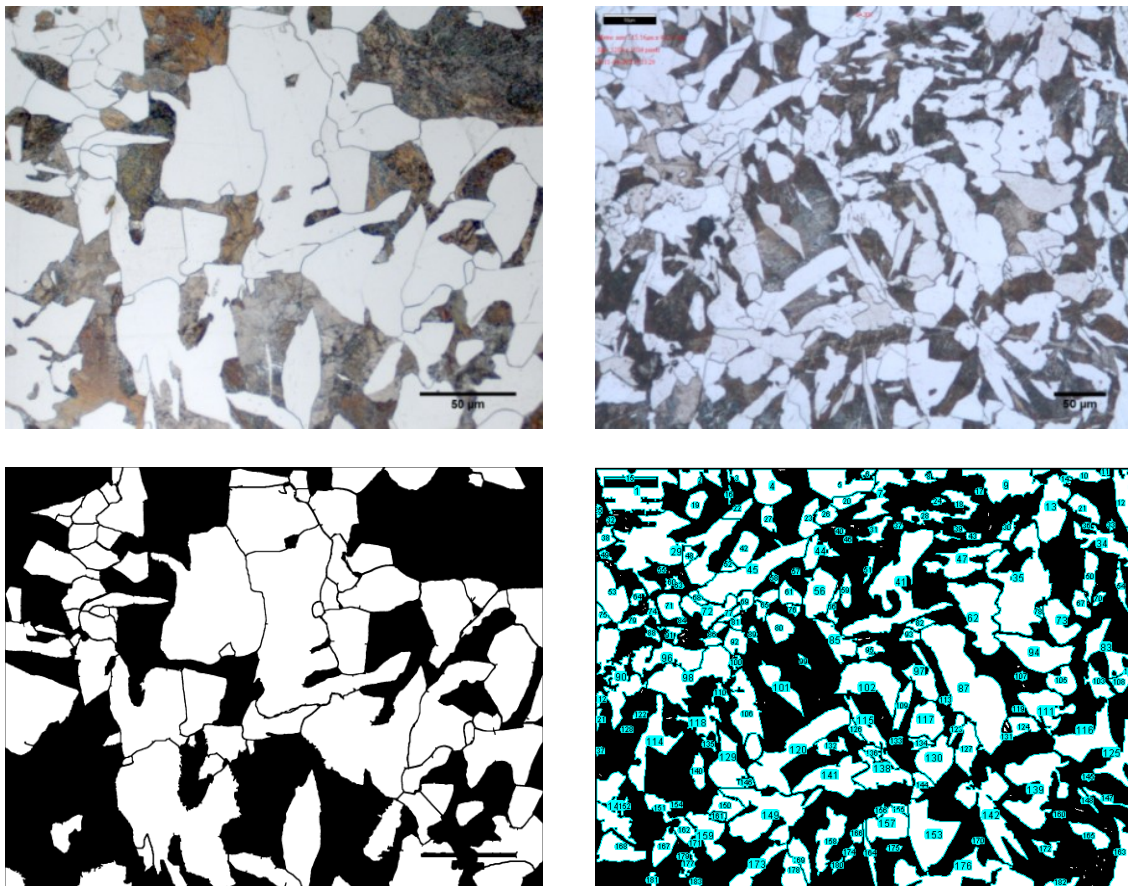
- 3- Define grain size number from chart shown in APPENDIX B, Figure B2.
- 4- Obtain grain diameter and area from table shown in APPENDIX B, Figure B3.

#### 4.4.2 *ImageJ Software*

ImageJ [70] is a public domain, Java-based image processing program that has features that allow measurement of the grain size of steels. In addition to grain size, it can be used to calculate grain diameter, average grains per  $\text{mm}^2$ , average grains per  $\text{mm}^3$ , and fraction of the total area. The software supports standard image processing functions such as contrast manipulation, sharpening, smoothing, edge detection and median filtering. An example screenshot which contains several windows and applications of ImageJ software is shown in APPENDIX B, Figure B4. The first step to measure grain size is to set the scale by selecting *Analyze* and *SetScale*, then converting the image to grayscale by selecting *Image* then *Type 8-bit*. The image is then converted to black and white to define grain edges by selecting *Make Binary*, APPENDIX B, see Figure B5. Finally, the grain size and area fraction are defined by selecting *Analyze Particles*.

The grain sizes of the normalized steels (X52, A106GRB) were determined using IFM. Even though no differences were observed in the materials' microstructures by using the two imaging techniques, there are significant differences between the grain size measurements obtained from IFM images and those obtained from Chevron Corp. images, as shown in Figure 19. The results obtained using ImageJ software [70] on the 200X IFM image are more accurate than those obtained with the 500X optical microscope image. Note that the results obtained using the intercept method, according to the ASTM E112 standard procedure [69] are the same for both magnifications. Using the

intercept method results as the standard value for this measurement, the ImageJ results for the 200X image only vary by 37% as compared to the 88% from analysis of the 500X optical microscopy image. In this case it is obviously due to the large grain size with respect to the image size that has caused the problem; ImageJ software was used for analysis as it has been shown to be a more comprehensive method, with the stipulation that the grain size should not be larger than 0.24% of the image dimensions. Table 4 shows a comparison between the grain size of X52 and A106GRB normalized steels.



a-Optical microscopy (500X)

b-IFM (200X)

Figure 19: Comparison between images that obtained by optical microscopy and IFM.

Table 4: Grain Sizes of X65II, X52, and A106GRB Steels.

		X52		A106GRB	
		Microstructure			
		Normalized steel with large amounts of pearlite.			
	Magnification	500X	200X	500X	200X
Intercept method ASTM E112 standard	Nominal Grain Diameter $d \mu\text{m}$	15	16	27	27
	Average Grain Size $\mu\text{m}^2$	225	252	713	713
	Average Grains per $\text{mm}^3 \times 10^3$	237	200	41	41
	Average grains per $\text{mm}^2 \times 10^3$	4.4	3.97	1.4	1.4
ImageJ	Grain size $\mu\text{m}^2$	188	235	379	518
	Area fraction Ferrite/pearlite	56	38.6	50.4	44.7

## CHAPTER 5: GENERAL CORROSION EXPERIMENTS

### 5.1 Introduction

This introductory set of corrosion experiments was conducted using a rotating cylinder electrode (RCE) in a glass cell (small scale system), as shown in Figure 20, and disk shaped samples in a Thin Chanel Flow Cell (TCFC, medium scale system), as shown in Figure 23. The TCFC has many advantages over the RCE. Although RCE experiments involve small volumes and small surface areas, challenges arise due to centrifugal forces, shaft vibration, and electrical contact problems during electrochemical measurements; there are also difficulties in reaching a high wall shear stress. In order to achieve the objectives of this work, RCE experiments were primarily carried out in order to validate initial TCFC tests, where RCE experiments in a glass cell are widely accepted and have been thoroughly tested [71]. After validation, TCFC cell experiments were conducted to study the effect of alloying elements and microstructure on the corrosion rate in a non-film forming environment. APPENDIX C contains detailed schematics of the TCFC system.

### 5.2 Tests done in a Glass Cell with a Rotating Cylinder Electrode (RCE)

#### 5.2.1 *Sample Materials*

Rotating cylinder electrodes (RCE) (0.5”D, 0.5” L) were machined from each steel and used in glass cell experiments.

#### 5.2.2 *Experimental Method*

An aqueous electrolyte was prepared from deionized water with a concentration of 1wt. % NaCl. The solution was initially deoxygenated by bubbling with CO<sub>2</sub>. This

procedure assured that the dissolved oxygen levels were kept below 20 ppb. The pH of the solution was adjusted by adding deoxygenated acid (HCl) or base (NaHCO<sub>3</sub>) in sufficient quantity to reach the desired pH. The test matrix is shown in Table 5. Before being tested, all samples were sequentially polished with abrasive paper of 250, 400 then 600 grit and flushed with isopropanol during the polishing, then immersed into isopropanol filled ultrasonic bath, and finally air dried.

A Gamry potentiostat was used to conduct the electrochemical measurements. Ag/AgCl probe was used as the reference electrode. Open-circuit potential (OCP) was first measured and sufficient time allowed for stabilization of the sample potential. This was important in order to ensure a correct reading of the linear polarization resistance (LPR) measurement, especially since a large fluctuation in OCP values (greater than 10% of the applied potential for LPR measurement) would yield inaccurate polarization resistance ( $R_p$ ) values. The sample potential was polarized from -5 mV to +5 mV with respect to the OCP at a scan rate of 0.125 mV/s. LPR measurements were carried out three times during each experiment. Prior to each LPR measurement, OCP was measured for five minutes to ensure that the potential of the sample had returned to its original reading and was stable. The corrosion current of each measurement was calculated using Equation 17:

$$I_{corr} = \frac{B}{R_p} \quad (17)$$

Where:

$I_{corr}$  - is the corrosion current (A)

$B$  – is the Stern-Geary coefficient (V)

$R_p$  - is the polarization resistance ( $\Omega$ )

The Stern-Geary coefficient ( $B$  value) may vary from 0.013 to 0.052 V depending on metal and electrolyte. Here it is suggested to use  $B=0.026$  V, assuming that the corrosion rate was not purely under charge-transfer control [72], since this value is usually validated with weight loss corrosion measurements in such environments.  $B=0.026$  V can be calculated using values of 0.12 V/decade for both the anodic and cathodic Tafel coefficients:

$$B = \frac{\beta_a * \beta_c}{2.3 * (\beta_a + \beta_c)} \quad (18)$$

Where  $\beta_a, \beta_c$  are anodic and cathodic Tafel coefficients (V/decade)

The corrosion rate of each LPR measurement was calculated using Equation 19:

$$CR = \frac{I_{corr} * K * EW}{d * A} \quad (19)$$

Where:

$I_{corr}$  - is the corrosion current (Amps) calculated from Equation 17

$K$  - is the conversion factor that defines the corrosion rate units ( $K=3272$  for mm/y units)

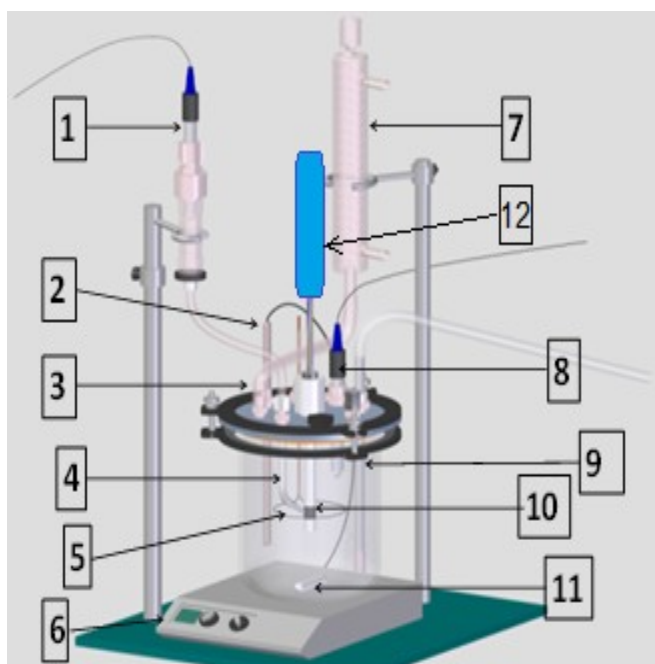
$EW$  - is the equivalent weight (grams/equivalent)

$d$  - is the density of the sample (grams/cm<sup>3</sup>)

$A$  - is the sample surface area (cm<sup>2</sup>)

Table 5: Test Matrix: Glass Cell Experiments (Uniform Corrosion).

Parameters	Conditions
Temperature	25 °C, 80°C
Total pressure	1 bar
CO <sub>2</sub> Partial pressure	0.95, 0.5 bar
Solution	1 wt.% NaCl
pH	4.0
RCE Material	X52, X65I, X65II, X70, A106GRB
Velocity	1000 RPM
Test time	2 hours
Measurement methods	LPR



1. Reference electrode.
2. Temperature probe.
3. Gas outlet.
4. Luggin capillary.
5. Platinum counter electrode.
6. Hot plate.
7. Condenser.
8. pH electrode.
9. CO<sub>2</sub> sparge tube.
10. Sample.
11. Magnetic stir bar.
12. Rotating motor

Figure 20: Schematic image of glass cell used to conduct the corrosion experiments.

### 5.2.3 Results and Discussion

The CO<sub>2</sub> corrosion of each steel was studied at pH 4.0, 1000 rpm, two different temperatures (25°C, 80°C), and respective partial pressures of CO<sub>2</sub> (0.95 bar, 0.5 bar). Corrosion rate data are shown in Figure 21 and Figure 22. The corrosion rates range between 1.8 and 2.3 mm/y at 25°C and between 5.4 and 7.8 mm/y at 80°C. The glass cell LPR measurements were taken three times. The variation of corrosion rates (at 25°C, 80°C) within steels and between steels was analyzed using ANOVA method. The variation analysis shows that there are bigger differences in corrosion rates between different steels than within the same steel. However, this variation in corrosion rates between steels is not the same at 25°C and 80°C, see Figure 21 and Figure 22. The overall difference in corrosion rates is considered to be insignificant. From LPR results, there is no clear effect of microstructure and chemical composition of steel on general corrosion rate since the variation of corrosion rates are not the same at 25°C, 80°C. As expected, in an environment where corrosion product layer does not form, mild steels of similar composition should exhibit the same mechanisms for general corrosion.

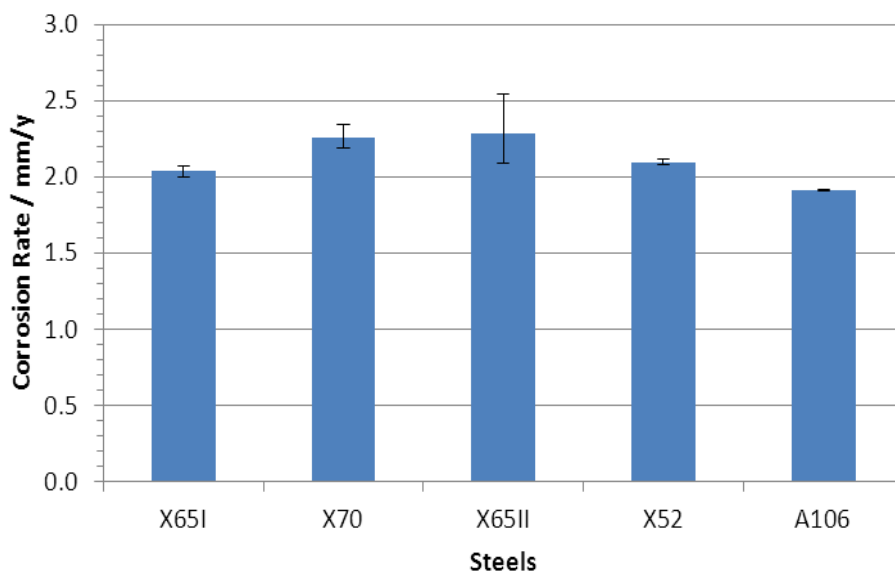


Figure 21: RCE corrosion rate at 25°C, 0.95 bar CO<sub>2</sub>, pH 4.0, 1000 rpm, and B=26 mV/decade.

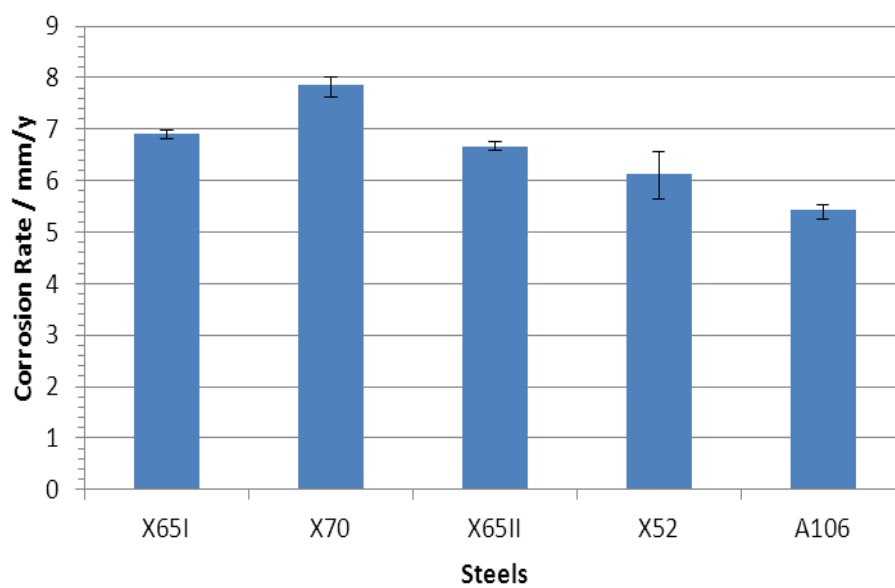


Figure 22: RCE corrosion rate at 80°C, 0.5 bar CO<sub>2</sub>, pH 4.0, 1000 rpm, and B=26 mV/decade.

### 5.3 Tests done in the Thin Channel Flow Cell (TCFC) System

#### 5.3.1 *Sample Materials*

Ten disk shaped samples (1.25”D, 0.25”L) were machined (two from each steel), with specific dimensions to fit the corrosion coupon holders used in TCFC experiments, see Figure 23.

Electrodes for linear polarization resistance (LPR) measurements were machined and assembled for each steel. Each LPR electrode consists of a concentric ring electrode as a working electrode made from the same steel being tested and a pin electrode as a reference electrode made from 306 stainless steel. LPR electrodes are used as electrochemical probes to measure the corrosion rate by the LPR technique in TCFC experiments.

#### 5.3.2 *Experimental Method*

An aqueous electrolyte was prepared from deionized water with a concentration of 1wt. % NaCl, i.e. the same solution that was used in the glass cell experiments. The solution was initially deoxygenated by bubbling with CO<sub>2</sub>. This procedure assured that the dissolved oxygen levels were kept below 20 ppb. The pH of the solution was adjusted by adding deoxygenated acid (HCl) or base (NaHCO<sub>3</sub>) in sufficient quantity to reach the desired pH.

A Gamry potentiostat was used to conduct the electrochemical measurements. A Ag/AgCl probe was used as the reference electrode. In each experiment, one concentric ring electrode, made from the steel being tested, was used as the electrochemical probe to measure the corrosion rate by the LPR technique. Here again, open-circuit potential

(OCP) was first measured to allow sufficient time for the sample potential to stabilize. The sample potential was polarized from -10 mV to +10 mV with respect to the OCP at a scan rate of 0.125 mV/s. The total time for each experiment was 24 hours, and the LPR measurements were carried out every 4 hours. Prior to each LPR measurement, OCP was measured for five minutes to ensure that the potential of the sample would return to its original reading and be stable. The corrosion rate was calculated, as previously explained, using Equations 18 and 19.

In addition to LPR electrode measurements, two 1.25”D samples from tested steels were used as weight loss samples to measure the corrosion rate by weight loss. The weight loss was converted to corrosion rate by the following Equation 20:

$$\text{Corrosion rate} \left( \frac{\text{mm}}{\text{y}} \right) = \frac{8.76 * 10^4 * W}{A * t * d} \quad (20)$$

Where:

$W$  - is the mass loss (g).

$A$  - is the surface area of the sample (m<sup>2</sup>).

$t$  - is the exposure time (hours).

$D$  - is the density of the sample material (g/m<sup>3</sup>).

$8.76 \times 10^4$  - is the conversion factor.

To determine the velocity in the TCFC equal to the rotational velocity of the RCE that was used in the glass cell experiments, the rotational velocity was converted to linear peripheral velocity (1000rpm = 0.63 m/s). However, the proper way to calculate the velocity in the TCFC that equals the rotational velocity of the RCE is by equating the mass transfer rates in both glass cell and TCFC systems. This was confirmed in a more

detailed analytical study by A. Nor [73]. He reported that the 1000 rpm rotational velocity of the RCE in the glass cell is equal to 1.0 m/s velocity in the TCFC. However, the effect of using the velocity of  $v=0.63$  m/s (linear peripheral velocity of RCE) instead of  $v=1.0$  m/s (as suggested by A. Nor) is considered to be of little consequence.

The test matrix is shown in Table 6.

Table 6: TCFC Experiments (Uniform Corrosion)

Parameters	Conditions
Temperature	25°, 80°C
Total Pressure	1 bar
CO <sub>2</sub> Partial Pressure	0.95, 0.5 bar
Solution	1 wt. % NaCl
pH	4
Material	X65I, X52, X65II, X70, A106 GRB
Velocity	0.63 m/sec
Test time	24 hours
Measurement methods	LPR, weight loss

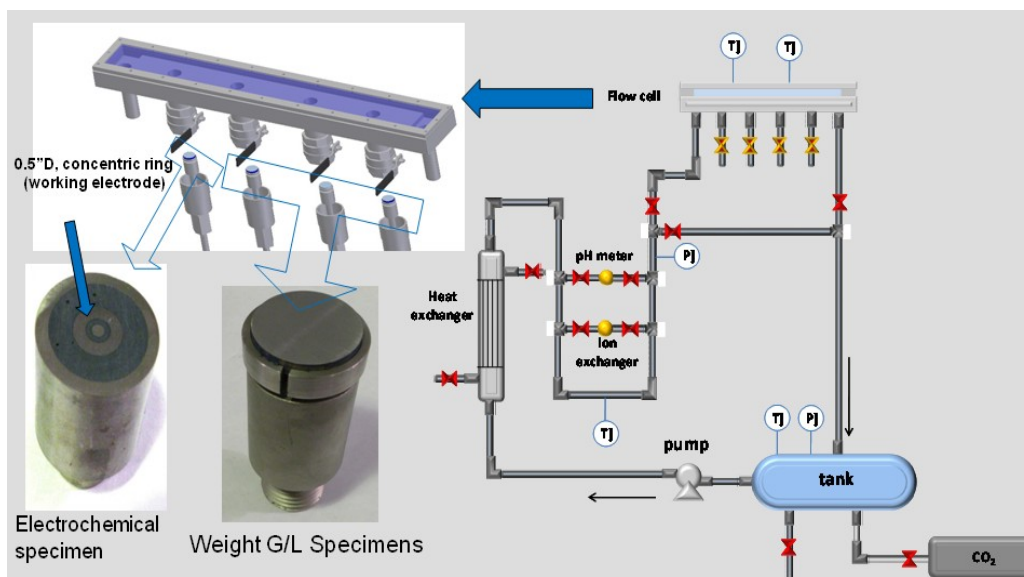


Figure 23: Schematic diagram of the thin channel flow cell (TCFC) system and samples used to conduct corrosion experiments.

### 5.3.3 Results and Discussion

The CO<sub>2</sub> corrosion of each steel was measured at pH 4.0, 0.63 m/s, two temperatures (25°C, 80°C), and two partial pressures of CO<sub>2</sub> (0.95 bar, 0.5 bar). Corrosion rate data are shown in Figure 24 and Figure 25. The corrosion rates measured by LPR range between 1.3 and 3.3 mm/y at 25°C and between 4.5 and 6.1 mm/y at 80°C. The LPR measurements for each steel were taken 6 times. Again, the variation of corrosion rates (at 25°C, 80°C) within steels and between steels was analyzed using ANOVA. The variation analysis shows that there are relatively more difference in corrosion rates between different steels than within the same steel. In addition to LPR measurements, the corrosion rates were also measured using weight loss. The weight loss corrosion rates range between 1.6 and 2.4 mm/y at 25°C and between 6.8 and 9.6 mm/y at 80°C, see Figure 24 and Figure 25. Here, the variation analysis of the weight loss

corrosion rates at 25°C shows that there is no difference in corrosion rates within and between steels. On the other hand, the variation analysis of the weight loss corrosion rates at 80°C shows that there is relatively more difference in corrosion rates between different steels than within the same type of steel. Here also, the difference in corrosion rates is considered to be insignificant, where the variation in corrosion rates between different steels is not the same at 25°C and 80°C.

As shown in Figure 24 and Figure 25, there are differences between corrosion rates of steels measured by LPR and weight loss at 25°C and 80°C. These differences can be due to incorrect  $B$  value used. However, adjusting the  $B$  value will not solve the problem for all steels because the LPR corrosion rate of X65II is less than the weight loss corrosion rate while the LPR corrosion rates of other steels are higher than their weight loss corrosion rates. Here again it is expected that in a non-film forming environment, mild steels of similar composition, such as the ones used here, should exhibit the same corrosion behavior when it comes to general corrosion.

Figure 26 and Figure 27 show a comparison between the RCE and TCFC corrosion rates measured by LPR at 25°C and 80° C. The variation of corrosion rates within steels and between steels was analyzed using ANOVA. The variation of corrosion rates (at 25°C, 80°C) within steels is relatively high. It is thought that these variations in the results could be caused by many factors, such as the centrifugal forces and shaft vibration in the glass cell RCE, and the flow fluctuation in the TCFC. Given the complexity of the corrosion process, it was concluded that the agreement between results obtained from the RCE and TCFC experiments, see Figure 26 and Figure 27, could be

considered as sufficient for the purposes of the present study which focused on conditions where protective iron carbonate layers form.

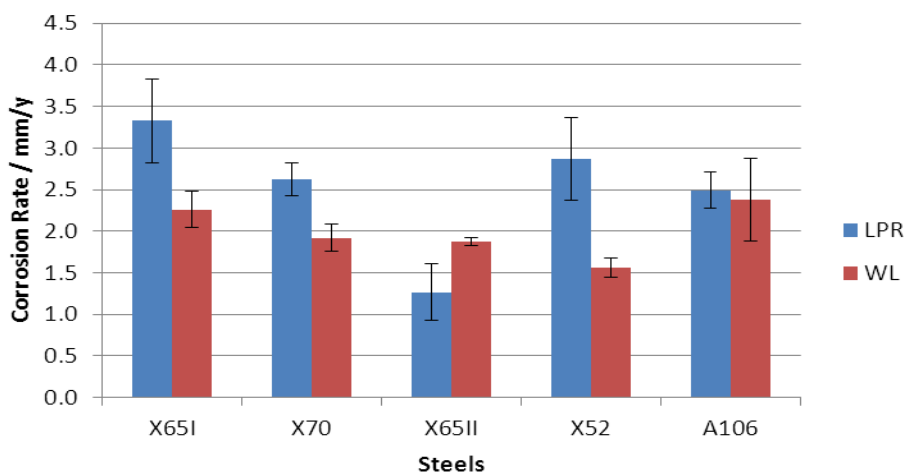


Figure 24: TCFC corrosion rate measured by LPR, weight loss (WL), at 25°C, 0.95 bar CO<sub>2</sub>, pH 4.0, 0.63 m/s, B=26 mV/decade.

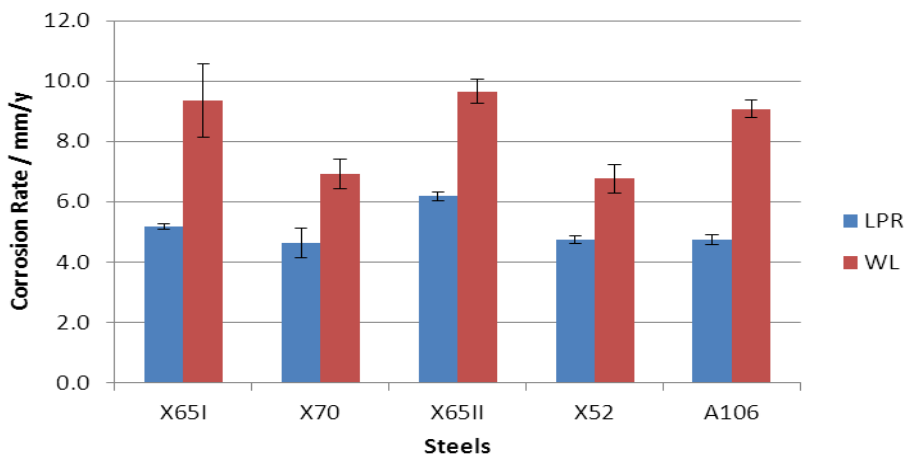


Figure 25: TCFC corrosion rate measured by LPR, weight loss (WL), at 80°C, 0.5 bar CO<sub>2</sub>, pH 4.0, 0.63 m/s, B=26 mV/decade.

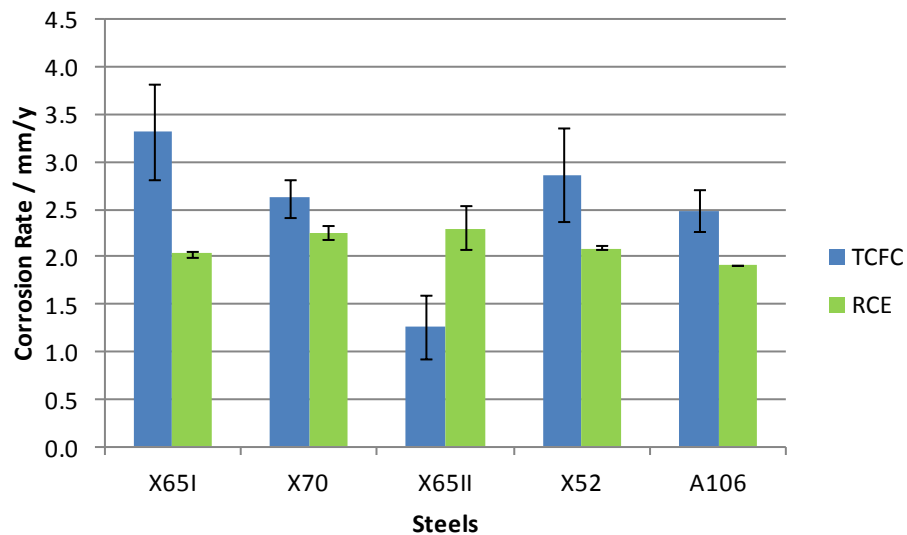


Figure 26: Comparison between RCE & TCFC corrosion rates measured by LPR, at 25°C, 0.95 bar CO<sub>2</sub>, pH 4.0, 0.63m/s, B=26 mV/decade.

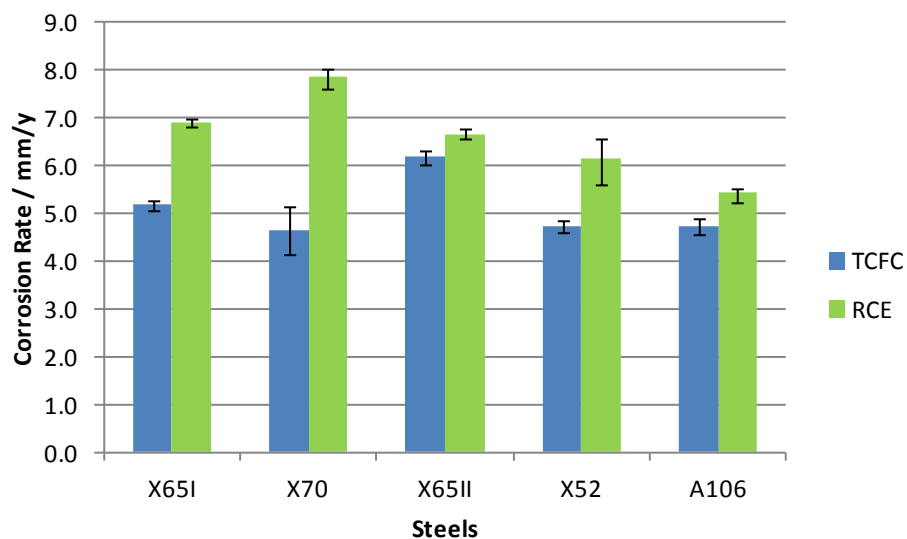


Figure 27: Comparison between RCE & TCFC corrosion rates measured by LPR, at 80°C, 0.5 bar CO<sub>2</sub>, pH 4.0, 0.63 m/s, B=26 mV/decade.

#### 5.4 Summary

For the purposes of the present study, there were no significant differences between results from experiments conducted in a glass cell and in the TCFC. Although the microstructures of steels were different, no significant systematic variation in general corrosion for all steels with different composition and microstructure was observed at pH 4.0, even with varying temperature and velocity. Since RCE experiments in a glass cell are widely accepted and have been thoroughly tested [71], it was considered that this validates the use of the TCFC so that it can be used to further study corrosion at high flow rates which are not achievable by RCE in glass cells. In the author's opinion, the reason for the lack of effect of steel composition and microstructure on general corrosion rate is because no corrosion product layer was formed at pH 4.0, so there was no significant effect of alloying elements and microstructure on the corrosion rate in a undersaturated environment.

## CHAPTER 6: FLOW EFFECT EXPERIMENTS

### 6.1 Introduction

The intensity of the fluid flow can affect the formation and protectiveness of corrosion product layers of  $\text{FeCO}_3$ , [38]-[47], which is also dependent on the microstructure and chemical composition of the steel [29], [33], [57]. If the flow rates are high, and so are the wall shear stresses, the influence of flow can be significant and its effects can cause local breakdown of the corrosion product layers of  $\text{FeCO}_3$  [35], [41], [45], [74] leaving uncovered portions of the steel surface directly exposed to the aggressive environment. This local breakdown of the  $\text{FeCO}_3$  layer can also lead to localized corrosion, which may be more dangerous than uniform corrosion for pipe integrity.

To generate high wall shear stresses as can be found in field applications [75] or higher, a Thin Channel Flow Cell (TCFC) is used, which is illustrated in Chapter 5. The TCFC can be used to conduct corrosion tests at low flow rates as well as at very high flow rates (up to 17 m/s). The combination of this high velocity and the thin channel (3mm height) allows the generation of high wall shear stresses (up to 535Pa). The TCFC also provides a more uniform distribution of wall shear stress on the test sample as compared to the submerged impinging jet, where the distribution of wall shear stress that is produced by the flow impingement of a jet on a flat surface is not uniform [75], [76]. Although fluid velocities in the oil and gas industry may be much lower than 17 m/s, some studies have indicated that multiphase flow can generate very high wall shear stresses. One study [76] shows that the wall shear stress of slug flow with a superficial liquid velocity of 1.0 m/s and gas velocity of 4.8 m/s can generate a high wall shear stress

up to  $7.4 \times 10^7$  Pa. It was reported that the bubble impacts that are produced from slug flow are able to destroy the corrosion product layer.

## 6.2 Wall Shear Stress Determination

To determine the hydrodynamic forces that can cause a breakdown of the  $\text{FeCO}_3$  layer, these forces should be expressed in terms of wall-shear stress rather than flow rate or velocity. The mean shear stress developed on the bottom wall of the TCFC was determined at  $25^\circ\text{C}$  using three different methods:

- Wall shear stress sensor.

The wall shear stress (WSS) was measured at different flow rates using an instrumented sensor (Lenterra Company [77]). This probe was installed in one of the TCFC ports employing a special holder.

- By measurement of the pressure drop between two points.

The wall shear stress was calculated using Equation 21. The pressure difference between two points in the TCFC (locations 1 and 2, Figure 28) was measured using a digital differential pressure gauge.

$$\tau = \frac{(p_1 - p_2) * h * w}{(2 * (h + w) * l)} \quad (21)$$

Where:

$\tau$  - is the mean shear stress at the wall (Pa)

$p_1$  - is the pressure measured at the location 1 (Pa)

$p_2$  - is the pressure measured at the location 2 (Pa)

$h$  - is the height of TCFC (m)

$w$  - is the width of TCFC (m)

$l$  - is the length between the locations 1 and 2 in the TCFC (m)

- By using a correlation

Dean's correlation was developed to calculate the mean wall shear stress in rectangular ducts [78]. The mean wall shear stress ( $\tau$ , Equation 24) can be calculated using a friction factor ( $C_f$ , Equation 22), which depends on the Reynolds number ( $Re_h$ , Equation 23), based on the mean flow rate of the TCFC.

$$C_f = 0.073 * Re_h^{-0.25} \quad (22)$$

$$Re_h = \frac{h*v*\rho}{\mu} \quad (23)$$

$$\tau = \frac{f*\rho*v^2}{2} \quad (24)$$

Where:

$C_f$  - is the Dean's friction factor of the channel

$Re_h$  - is the Reynolds number

$v$  - is the mean fluid velocity in the TCFC calculated from volumetric flow measurements in a 1" pipe (m/s)

$\rho$  - is the density of the fluid, which is a function of temperature (kg/m<sup>3</sup>)

$\mu$  - is the dynamic viscosity of the fluid, which is a function of temperature(kg/m s)

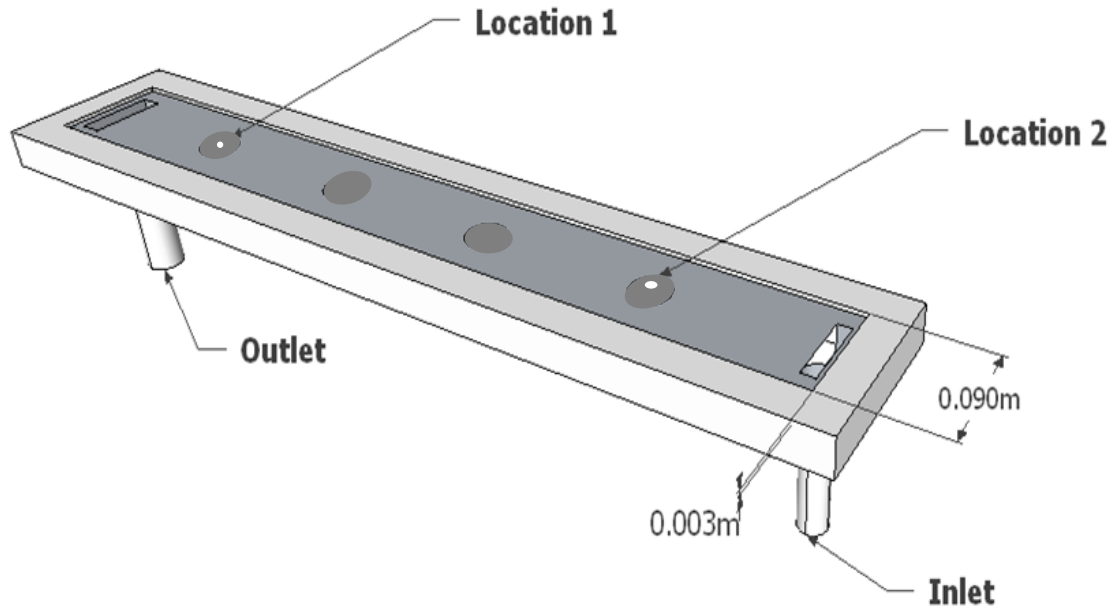


Figure 28: Schematic diagram of the thin channel flow cell (TCFC) used to conduct pressure drop measurement.

Figure 29 shows the comparisons between the three methods that were used to determine the wall shear stress values. From the chart it is clear that data collected by direct measurement agree with those determined by calculation using Dean's correlation. However, the data that were determined by pressure drop measurement do not agree well with those that were determined by direct measurement and calculation using Dean's correlation. This could be related to the effect of disturbed flow that was generated around the pressure measurement points, and the relatively short length of the TCFC, see Figure 28.

The maximum wall shear stress generated in the TCFC was calculated at 80°C, using Dean's correlation to be 535 Pa. Table 7 shows the physical properties of water and

Reynolds number at 535 Pa, where the Reynolds number is calculated using the height of the TCFC instead of the hydraulic diameter.

Table 7: Physical Properties of Water and Reynolds Number at Shear Stress of 535 Pa.

Temperature (°C)	$\mu$ of water (kg/m.s)	$\rho$ of water (kg/m <sup>3</sup> )	Velocity (m/s)	friction factor $C_f$	$Re_h$ Numbers
80	$3.5 \times 10^{-4}$	971.63	17	0.00378	139085

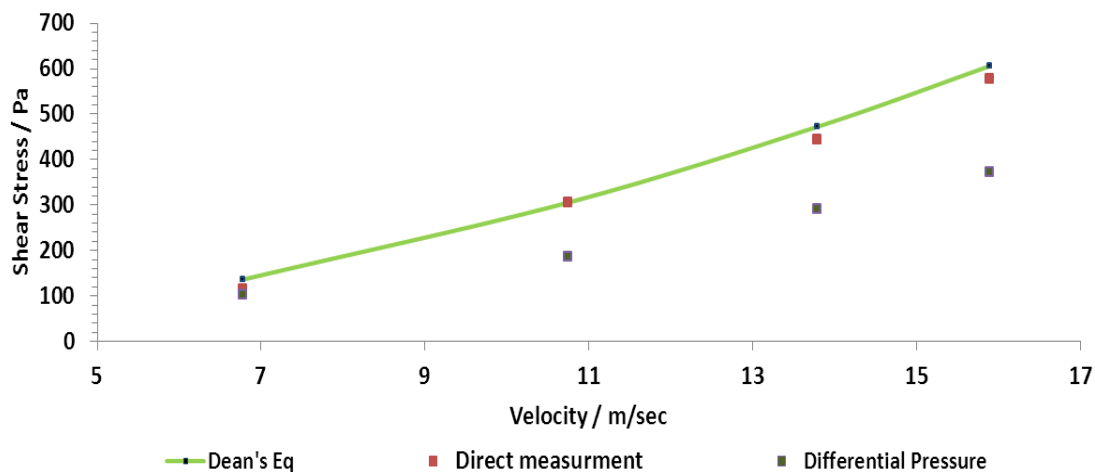


Figure 29: Wall shear stresses in the TCFC measured at 25° C with different methods for various flow velocities.

### 6.3 Effect of Flow on Formed $FeCO_3$ Corrosion Product Layer

#### 6.3.1 Introduction

As shown previously in Chapter 2, the  $FeCO_3$  corrosion product layer can form if the saturation value of  $FeCO_3$  in the bulk is sufficiently high [16]. This layer can be adherent and in good contact with the steel surface. In this chapter, the  $FeCO_3$  layer was generated on each steel under supersaturated conditions ( $FeCO_3$  saturation value  $>1$ ) and

low flow rate (4 m/s,  $\tau=35$  Pa). Supersaturated conditions  $\text{CO}_2$  were obtained by adjusting the concentration of  $\text{Fe}^{2+}$ , temperature, and pH to the desired levels. In this study some experiments were repeated to make sure that the results can be replicated, as shown later in the text and in APPENDIX D. In addition, one of the experiments was performed without initial addition of  $\text{Fe}^{2+}$ , to determine if this factor enhances the protectiveness of the  $\text{FeCO}_3$  layer.

### 6.3.2 *Experimental Method*

In each experiment three weight loss specimens and one electrochemical probe of each steel were tested separately in the TCFC, which are shown in Figure 23 and described in detail in APPENDIX C. An  $\text{FeCO}_3$  layer is generated on each steel by adjusting the concentration of  $\text{Fe}^{2+}$ , temperature, and pH to the desired levels, as shown in Table 8. In order to accelerate the formation of the  $\text{FeCO}_3$  layer during experiments, the initial concentrations of  $\text{Fe}^{2+}$  ions were increased by addition of ferrous chloride tetrahydrate ( $\text{FeCl}_2 \cdot 4\text{H}_2\text{O}$ ). After addition of the  $\text{FeCl}_2 \cdot 4\text{H}_2\text{O}$ , the  $\text{Fe}^{2+}$  concentration in the solution was measured using a spectrophotometer to insure that the initial concentration of  $\text{Fe}^{2+}$  is between 18-22 ppm. Then the  $\text{Fe}^{2+}$  concentration was monitored to make sure that the solution during the experiment is in a supersaturated condition with respect to  $\text{FeCO}_3$ . An exposure of 2 days was used to ensure the generation of an  $\text{FeCO}_3$  layer with full surface coverage, as determined from LPR measurements and SEM images of samples after 2 days of exposure. During the 2-day layer formation, a flow velocity of 4.0 m/s (35 Pa, wall shear stress) was kept constant. After the layer formed on the steel, the samples were exposed to high wall shear stress (535 Pa) for 3 days.

The following probes were introduced in each experiment:

- One concentric ring probe, described previously (Chapter 5) with the working electrode made from the steel to be tested, was used for the electrochemical measurements of corrosion rate by the LPR technique ( $\pm 10$  mV vs.  $E_{\text{corr}}$ ).
- Three, 1.25" diameter, flat specimens made from the same steel were used in each experiment. One specimen was used to measure the corrosion rate by the weight loss method, at the end of total exposure (5 days). The other two specimens were used to conduct top surface and cross-section analysis of the  $\text{FeCO}_3$  layers after 2 (low wall shear stress) and 5 days of exposure (2 days of low shear stress and 3 days of high shear stress).

All samples were rinsed immediately in isopropyl alcohol upon removal from the system, and then dried and stored in a desiccator, which contains a continuous flow of  $\text{N}_2$  to prevent oxidation of samples, until surface analyses by infinite focus microscopy (IFM), scanning electron microscopy (SEM) and energy dispersive spectroscopy (EDS) were conducted. In addition to surface analysis, cross-sectional analysis was conducted to examine the structure of the  $\text{FeCO}_3$  layer with respect to the microstructure of the steel of the  $\text{FeCO}_3$ . After analysis of the corrosion product layer, the weight loss samples were descaled using Clarke solution [79]. Average corrosion rates were then measured from the weight loss of samples. Microscopy, using IFM and SEM, was then conducted to characterize corrosion morphology.

### 6.3.3 Results

For all steels tested, the general corrosion rate as measured by LPR started out high and then, due to formation of the  $\text{FeCO}_3$  layer, it was reduced to less than 1.0 mm/y

after 2 days of exposure, see Figure 30. Increasing the wall shear stress caused the  $\text{FeCO}_3$  layer to fail in certain locations. Some steels suffered localized corrosion, as shown in details later in the text and these experiments were repeated, see APPENDIX D.

Table 8: Test Matrix: The Effect of High Wall Shear Stress ( $\tau = 535 \text{ Pa}$ ) on Adhesion and Protection from an  $\text{FeCO}_3$  Layer Formed at Low Wall Shear Stress ( $\tau = 35 \text{ Pa}$ ).

Parameters	Step 1	Step 2
	$\text{FeCO}_3$ layer formation	$\text{FeCO}_3$ layer removal
Temperature	80°C	80°C
Total pressure	2.0 bar	2.0 bar
$\text{CO}_2$ Partial pressure	1.5 bar	1.5 bar
pH	6.6	6.6
Solution	1.0 wt. % NaCl	
Materials	X52, X65I, X65II, X70, A106 GRB	
Measurement methods	LPR, weight loss	
Surface morphology	IFM, SEM and EDS	
Test time	2 days	3 days
Velocity	4 m/s	17m/s
Wall shear stress	35 Pa	535 Pa
Initial $[\text{Fe}^{2+}]$ concentration	18-22 ppm	

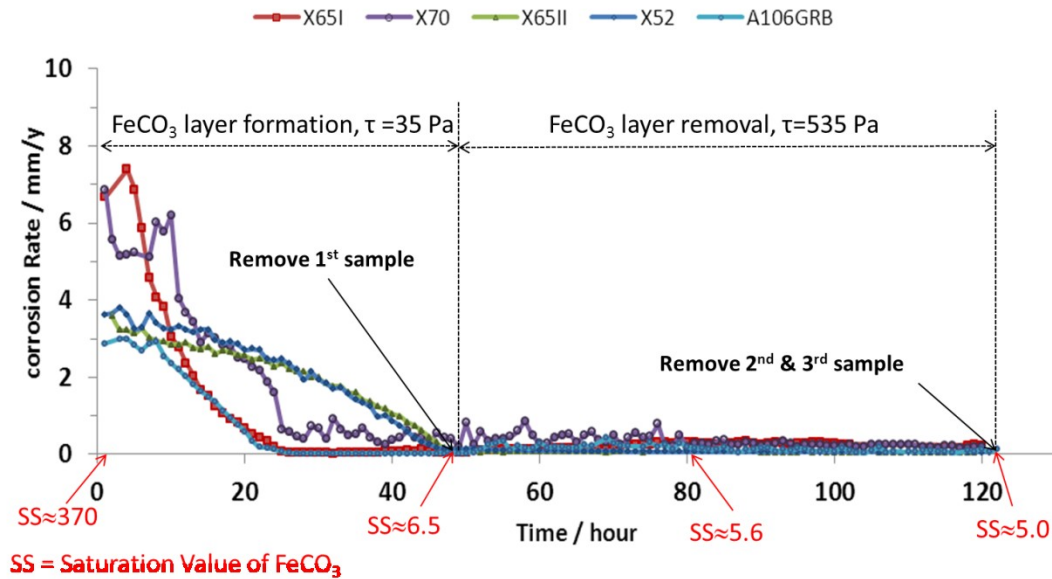


Figure 30: Corrosion rate obtained from LPR measurements versus exposure time at 80°C, 1.5 bar CO<sub>2</sub>, pH 6.6, B=26 mV/decade,  $\tau=35$  Pa for the first 2 days,  $\tau=535$  Pa for another 3 days.

The results of LPR, weight loss, SEM, and IFM of all tested steels were analyzed separately for each steel type.

- X65I steel:

Variation of the LPR corrosion rate of X65I with exposure time is shown in Figure 31. At the beginning of the test, the corrosion rate was 7-8 mm/y. During the FeCO<sub>3</sub> layer formation process the corrosion rate gradually decreased, dropping below 0.1 mm/y after about 24 hours; it remained low during the next 24 hours of exposure with some variation. After 2 days, the first sample was removed from the TCFC to document the developed FeCO<sub>3</sub> layer and then the wall shear stress was increased to 535 Pa for the remainder of the experiment. The general corrosion rate as measured by LPR after the wall shear stress was increased to 535 Pa increased by a factor of 2-3, but remained rather

low. This indicates that the steel surface remained mostly covered by a protective  $\text{FeCO}_3$  layer.

The images that were taken by SEM upon removal of the samples from the system after the first 2 days of exposure show that the sample was fully covered with a dense corrosion product layer with discrete crystals, as seen in Figure 32 and Figure 34. The appearance of the crystals as well as the elemental analyses by EDS, see Figure 33, suggest that this is an  $\text{FeCO}_3$  layer. This was confirmed in a more detailed study analytical study by Fajardo [80],[81], where Raman, XPS and XRD compositional analyses were done to complement the EDS elemental results.

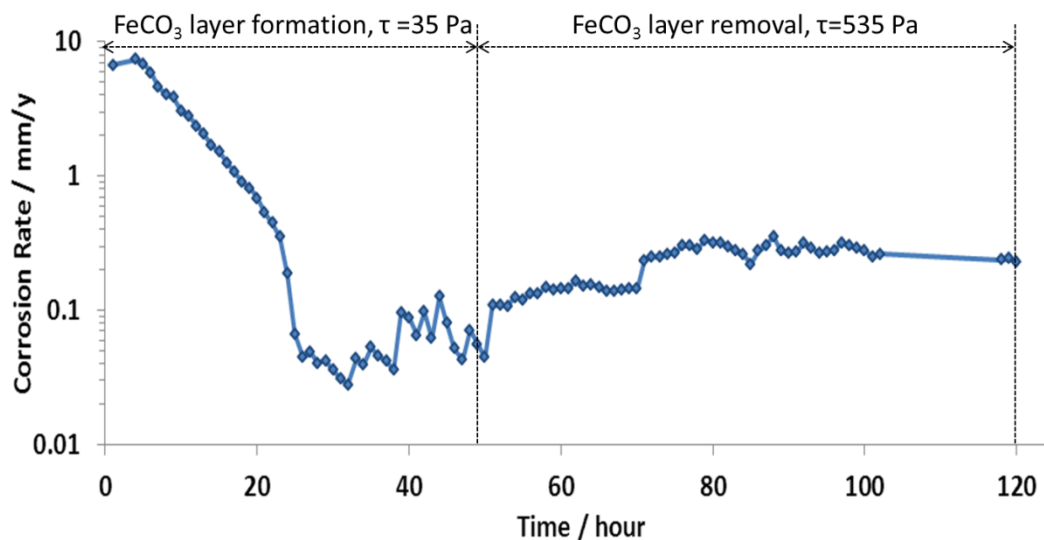


Figure 31: LPR Corrosion rate of X651 steel during 5 days of exposure at 80°C, 1.5 bar  $\text{CO}_2$ , pH 6.6,  $B=26$  mV/decade,  $\tau= 35$  Pa for the first 2 days,  $\tau= 535$  Pa for another 3 days.

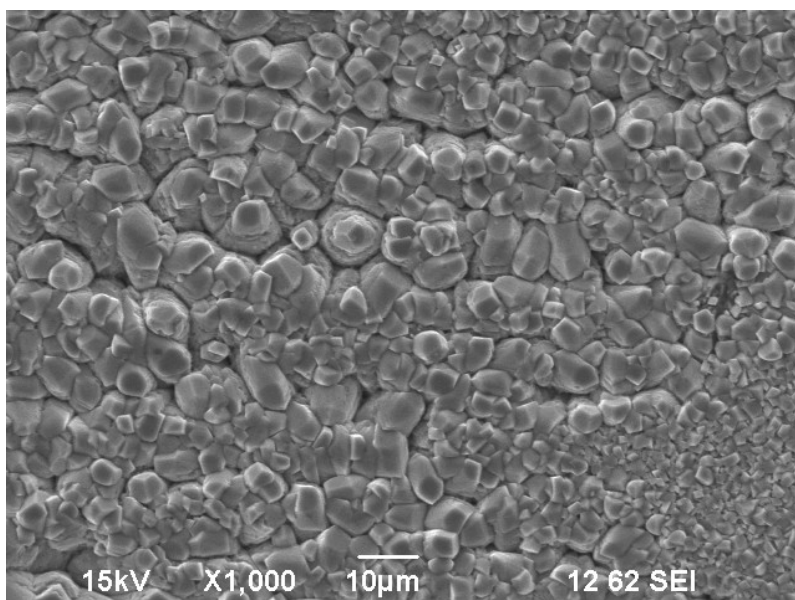


Figure 32: SEM top surface analysis of  $\text{FeCO}_3$  layer after 2 days of exposure at  $80^\circ\text{C}$ , X65I steel, 1.5 bar  $\text{CO}_2$ , pH 6.6,  $\tau = 35$  Pa for the first 2 days.

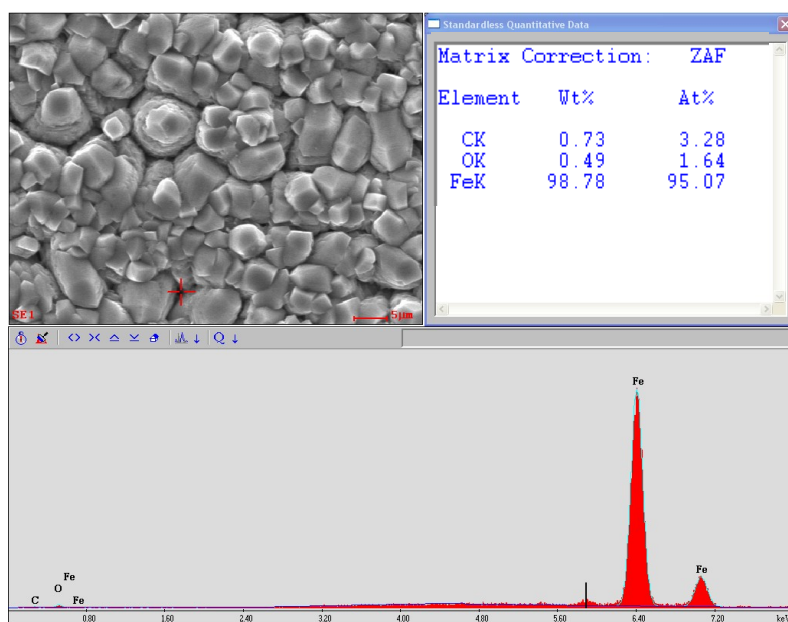


Figure 33: SEM & EDS top surface analysis of  $\text{FeCO}_3$  layer after 2 days of exposure at  $80^\circ\text{C}$ , X65I steel, 1.5 bar  $\text{CO}_2$ , pH 6.6,  $\tau = 35$  Pa for the first 2 days.

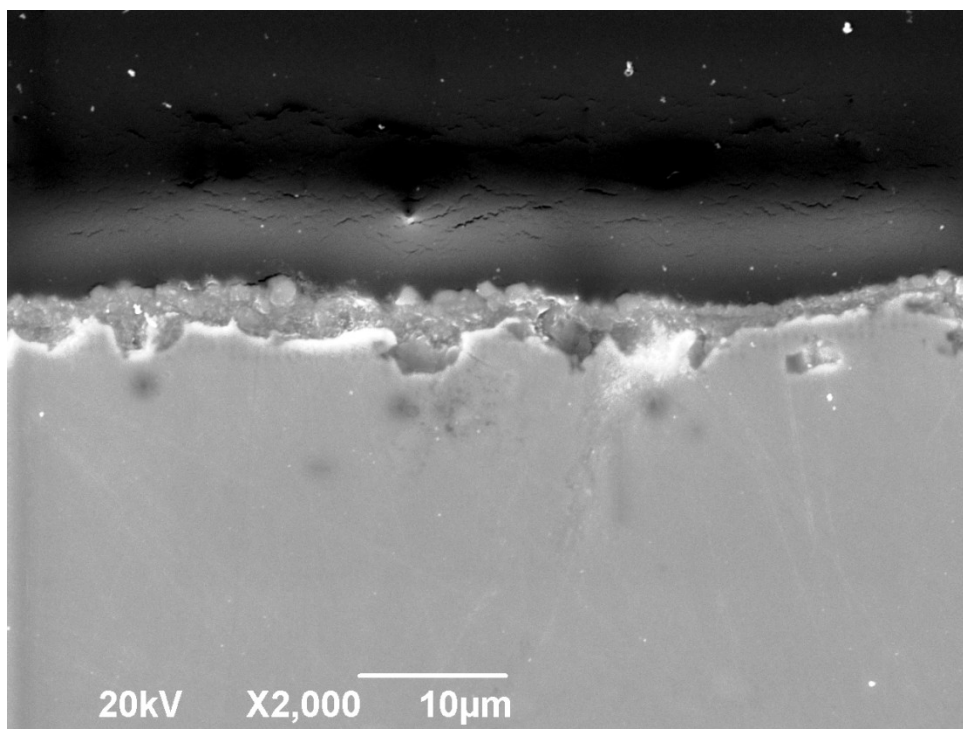


Figure 34: SEM cross section analysis of  $\text{FeCO}_3$  layer after 2 days of exposure at  $80^\circ\text{C}$ , X65I steel, 1.5 bar  $\text{CO}_2$ , pH 6.6,  $\tau = 35$  Pa for the first 2 days.

After 5 days of exposure the average corrosion rate measured by weight loss was found to be 2.1 mm/y, Figure 35, which was almost double the value obtained from integration in time of the CR values from LPR data. This suggests that probably the B value used here was underestimated. As mentioned before in chapter 5, the corrosion rate assumed was not purely under charge-transfer control, where is the mechanical removal of the  $\text{FeCO}_3$  layer that caused by flow can increase the corrosion rate. On the other hand, in layer forming conditions the anodic curves may not show linear behavior near  $E_{\text{corr}}$ , where the anodic passivation current could affect the LPR measurements.

Images that were taken by SEM and analysis done by EDS upon removal of the samples from the system at the end of exposure to the high wall shear stress showed that

the steel sample remained mostly covered by a dense  $\text{FeCO}_3$  layer, as shown in Figure 36 and Figure 37 respectively. However, comparison of SEM images before and after the increase in wall shear stress show that the  $\text{FeCO}_3$  crystals were removed from some small areas after the wall shear stress increased, see Figure 36. This shows the presence of voids and holes compared with the sample before the wall shear stress increase, Figure 32. These voids could be caused from the detachment of larger  $\text{FeCO}_3$  crystals by high wall shears stress. This detachment of these crystals could expose the steel beneath and cause localized corrosion. In addition to the top surface analysis, the IFM analysis of the surface after de-scaling the sample shows many pits with different sizes. In particular, Figure 38 shows the sample after 5 days of exposure, which contains many pits with different sizes. The IFM analysis shows the deepest pit with 70  $\mu\text{m}$  in depth and about 500  $\mu\text{m}$  in width, see Figure 38. As shown in Figure 39, the penetration rate of the deepest pit is compared with final corrosion rate measured by LPR, where the final corrosion rate represents the actual corrosion rate for longer periods of time. Here the deepest pit penetration rate is calculated to be 5 mm/y. The deepest pit penetration rate is very large compared with final corrosion rate that measured by LPR, which is 0.3 mm/y. The final corrosion rate is assumed to be the true corrosion rate corresponding to longer periods of exposure.

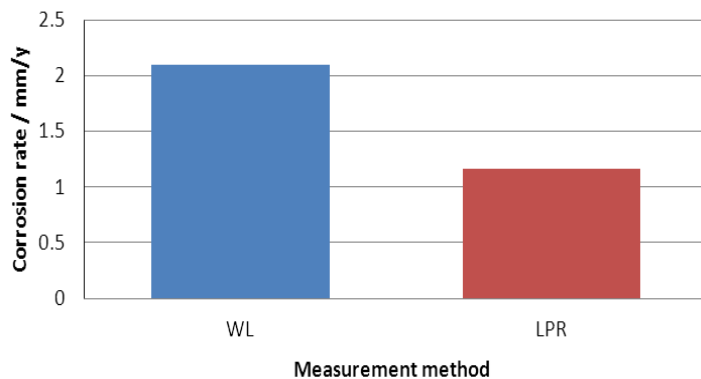


Figure 35: Comparison between corrosion rates measured by weight loss (WL) and integrated LPR after 5 days of exposure at 80°C, X65I steel, 1.5 bar CO<sub>2</sub>, pH 6.6, B=26 mV/decade,  $\tau = 35$  Pa for the first 2 days,  $\tau = 535$  Pa for another 3 days.

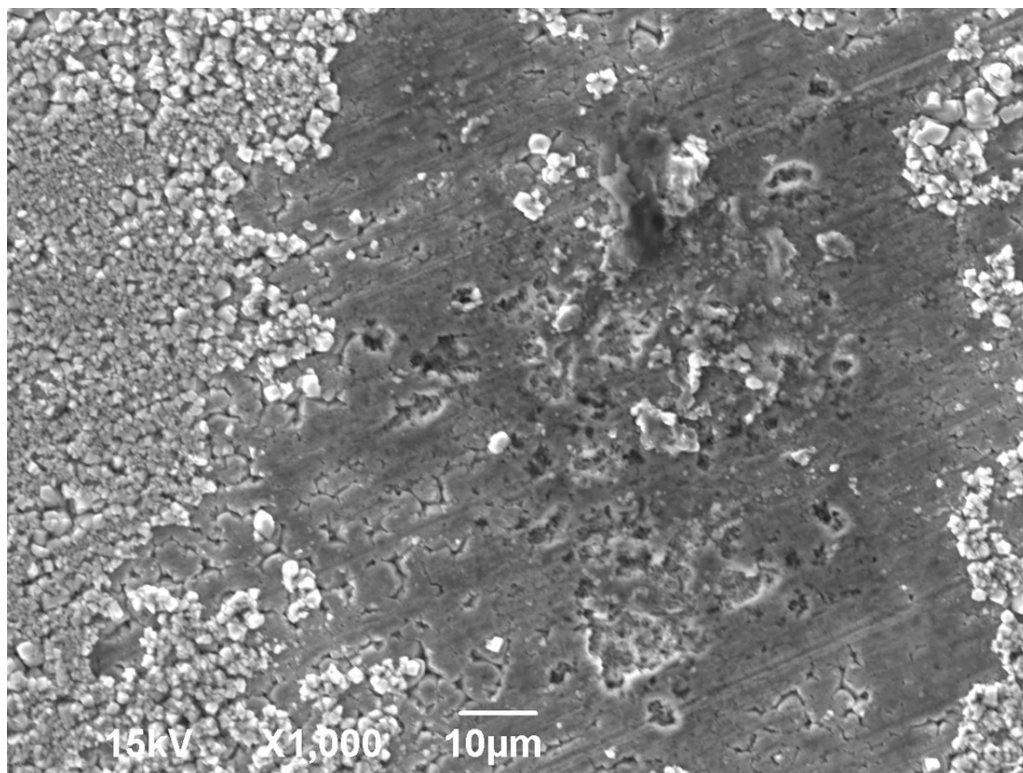


Figure 36: SEM top surface analysis of FeCO<sub>3</sub> layer after 5 days of exposure at 80°C, X65I steel, 1.5 bar CO<sub>2</sub>, pH 6.6,  $\tau = 35$  Pa for the first 2 days,  $\tau = 535$  Pa for another 3 days.

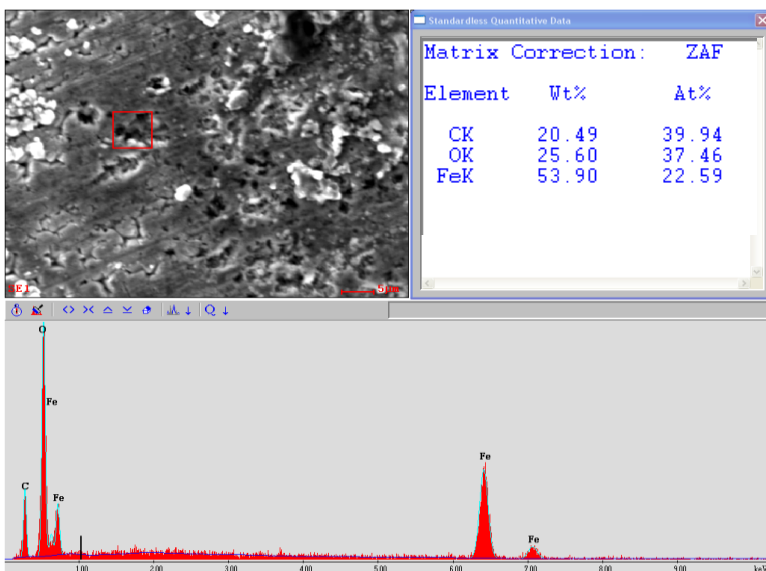


Figure 37: SEM & EDS top surface analysis of  $\text{FeCO}_3$  layer after 5 days of exposure at  $80^\circ\text{C}$ , X65I steel, 1.5 bar  $\text{CO}_2$ , pH 6.6,  $\tau = 35$  Pa for the first 2 days,  $\tau = 535$  Pa for another 3 days.

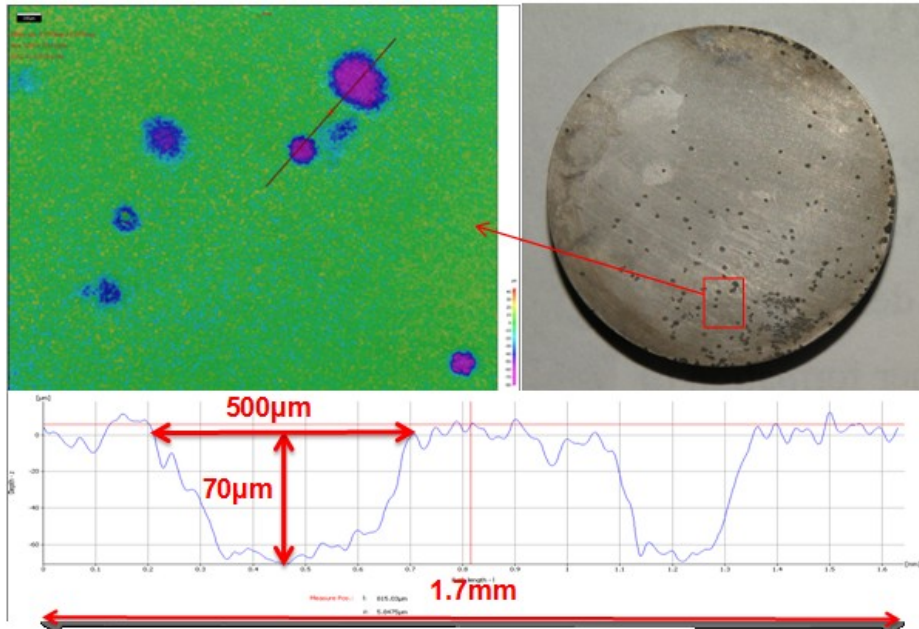


Figure 38: IFM image of descaled sample after 5 days of exposure at  $80^\circ\text{C}$ , X65I steel, 1.5 bar  $\text{CO}_2$ , pH 6.6,  $\tau = 35$  Pa for the first 2 days,  $\tau = 535$  Pa for another 3 days. Size of the deepest pit is  $500\mu\text{m}$  in width &  $70\mu\text{m}$  in depth.

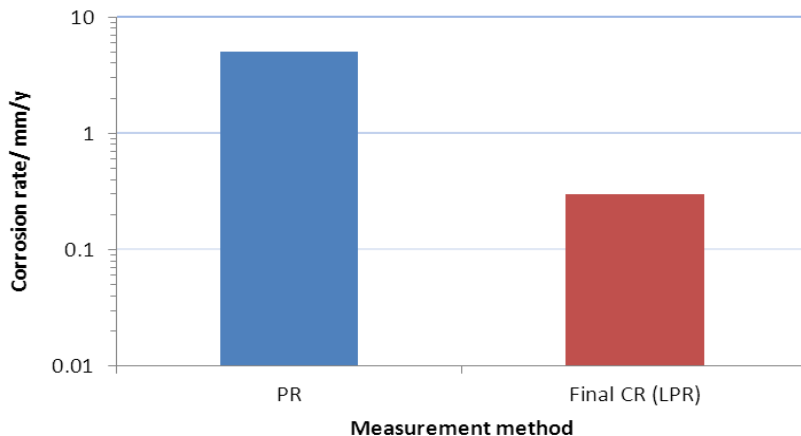


Figure 39: Comparison between the final corrosion rate measured by LPR and the penetration rate of the deepest pit on each steel (PR) after 5 days of exposure at 80°C, X65I steel, 1.5 bar CO<sub>2</sub>, pH 6.6, B=26 mV/decade,  $\tau = 35$  Pa for the first 2 days,  $\tau = 535$  Pa for another 3 days.

- X70 steel:

The variation of the LPR corrosion rate of X70 with exposure time is shown in Figure 40. At the beginning, the corrosion rate was about 6 mm/y. During the FeCO<sub>3</sub> layer formation the corrosion rate reduced gradually until reaching a value of less than 0.5 mm/y after about 30 hours and remained the same during the next 2 days of exposure. According to the procedures, the first sample was removed from the TCFC after 2 days to characterize the developed FeCO<sub>3</sub> layer and the wall shear stress was increased to 535 Pa for the remainder of the experiment. No increase in corrosion rate measured by LPR was noted after 2 days, which indicated that the steel surface was fully covered by a protective FeCO<sub>3</sub> layer.

The images that were taken by SEM upon removal of the samples from the system after the first 2 days of exposure show that the sample was fully covered with a dense corrosion product layer with discrete crystals, as seen in Figure 41. The appearance

of the crystals as well as the elemental analyses by EDS, see Figure 42 and Figure 43, suggest that this is an  $\text{FeCO}_3$  layer, [80], [81].

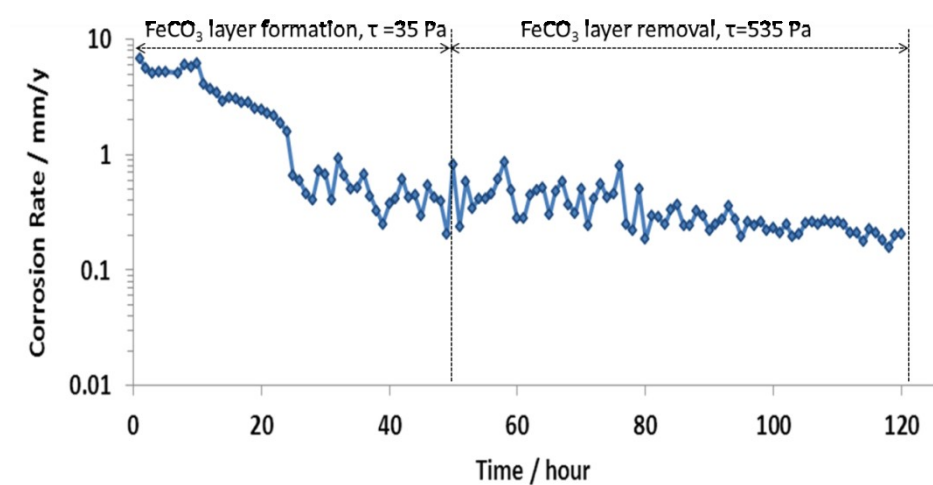


Figure 40: LPR Corrosion Rate of X70 steel during 5 days of exposure at  $80^\circ\text{C}$ , 1.5 bar  $\text{CO}_2$ , pH 6.6,  $B=26$  mV/decade,  $\tau= 35$  Pa for the first 2 days,  $\tau= 535$  Pa for another 3 days.

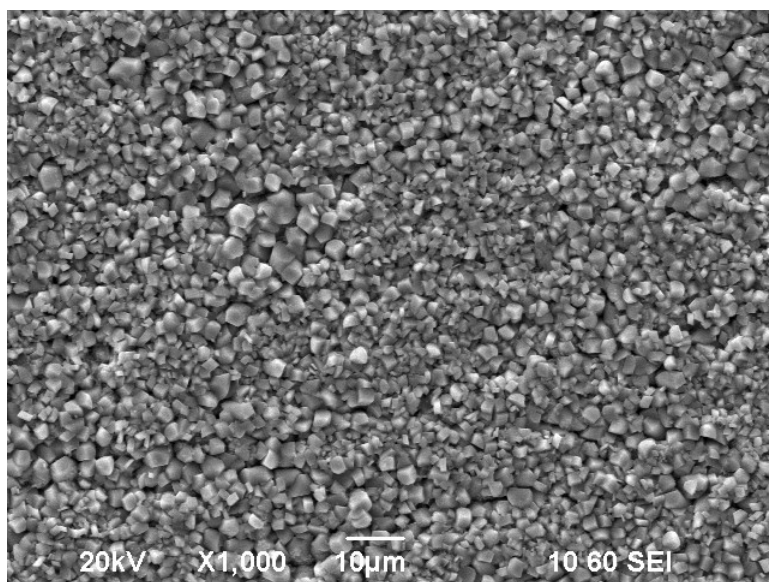


Figure 41: SEM analysis of X70 steel after 2 days of exposure at  $80^\circ\text{C}$ , 1.5 bar  $\text{pCO}_2$ , pH 6.6,  $\tau = 35$  Pa showing top surface view of  $\text{FeCO}_3$  layer.

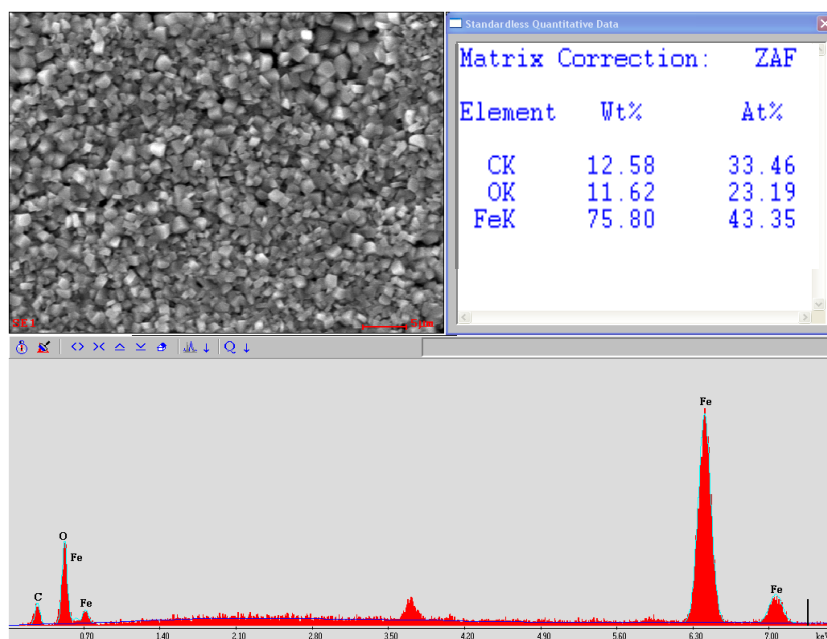


Figure 42: SEM & EDS top surface analysis of X70 steel after 2 days of exposure at 80°C, 1.5 bar CO<sub>2</sub>, pH 6.6,  $\tau=35$  Pa.

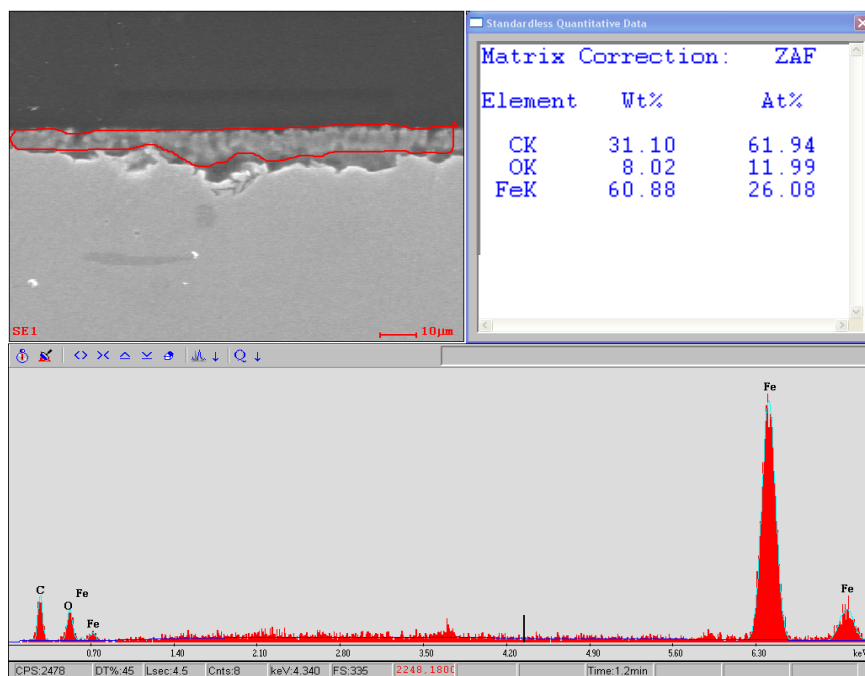


Figure 43: SEM & EDS cross section analysis of X70 steel after 2 days of exposure at 80°C, 1.5 bar CO<sub>2</sub>, pH 6.6,  $\tau=35$  Pa for the first 2 days.

After 5 days of exposure, the time and surface averaged corrosion rate measured by weight loss was found to be 4.0 mm/y, Figure 44, which was almost three times the value obtained from integration of the LPR data. This also suggests that probably the B value used here was also underestimated. Here again, it was assumed that the corrosion rate was not purely under charge-transfer control, where is the mechanical removal of the  $\text{FeCO}_3$  layer that caused by flow can increase the corrosion rate. On the other hand, in layer forming conditions the anodic curves may not show linear behavior near  $E_{\text{corr}}$ , where the anodic passivation current could affect the LPR measurements.

The images that were taken by SEM and EDS upon removal of the samples from the system after 5 days of exposure show that the sample was not fully covered with an  $\text{FeCO}_3$  layer; there are large areas where the layer was removed by flow, Figure 45 and Figure 46. The comparison between samples before and after wall shear stress increases, Figure 41 and Figure 45, show that regions of the  $\text{FeCO}_3$  layer were locally removed; however, these local areas where the  $\text{FeCO}_3$  layer was removed did not show an indication of further localized corrosion beneath the bare areas. The top surface analysis by SEM and EDX also shows the main element is the substrate material, indicating the surface is not well covered by an  $\text{FeCO}_3$  layer in these areas, Figure 46.

The IFM analysis of the surface after de-scaling the sample does show some corroded zones in the same area where layer is removed. Figure 47 shows pitting corrosion with 50  $\mu\text{m}$  in depth and about 200  $\mu\text{m}$  in width. As shown in Figure 48, the penetration rate of the deepest pit was compared with the final corrosion rate as measured by LPR, where this final corrosion rate represents an actual corrosion rate that would be

maintained for longer periods of time. Here the deepest pit penetration rate is calculated to be 3.6 mm/y, more than 10 times the final LPR corrosion rate which is 0.2 mm/y, and is considered to be localized corrosion.

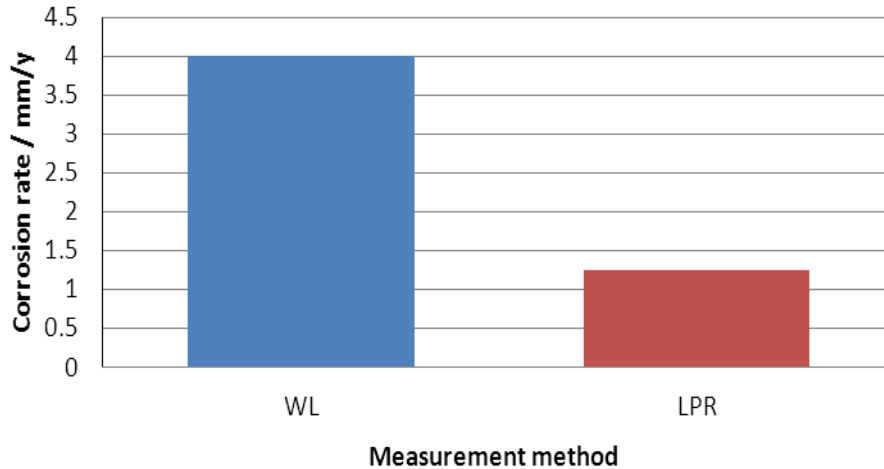


Figure 44: Comparison between corrosion rates of X70 measured by weight loss (WL) and integrated LPR after 5 days of exposure at 80°C, 1.5 bar CO<sub>2</sub>, pH 6.6, B=26 mV/decade,  $\tau=35$  Pa for the first 2 days,  $\tau=535$  Pa for another 3 days.

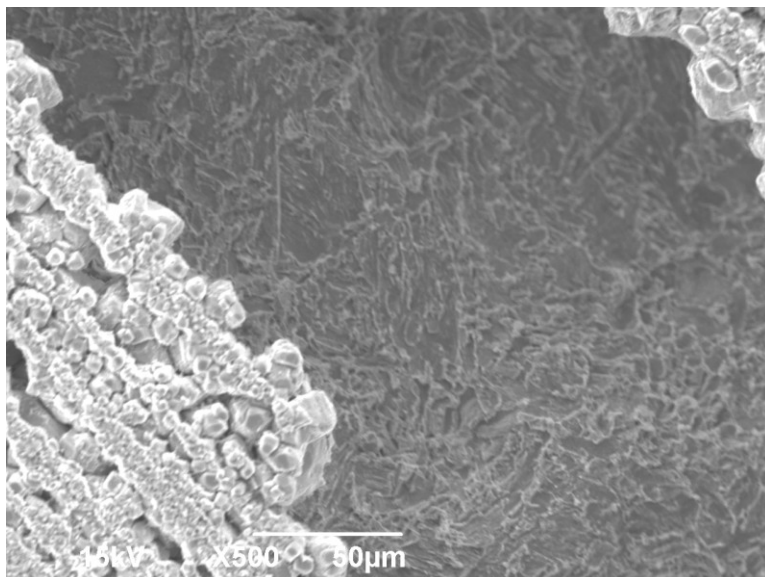


Figure 45: SEM top surface analysis of  $\text{FeCO}_3$  layer after 5 days of exposure at  $80^\circ\text{C}$ , X70 steel, 1.5 bar  $\text{CO}_2$ , pH 6.6,  $\tau= 35$  Pa for the first 2 days,  $\tau= 535$  Pa for another 3 days.

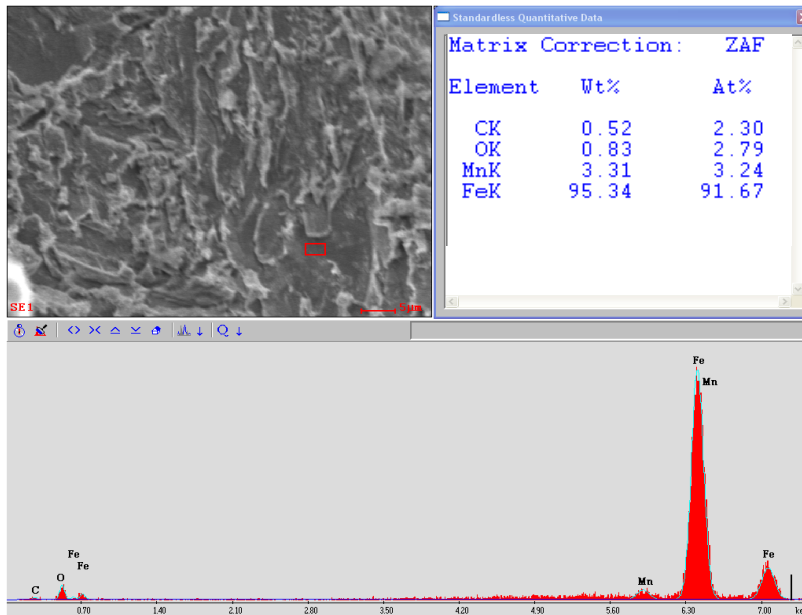


Figure 46: SEM & EDS top surface analysis of  $\text{FeCO}_3$  layer after 5 days of exposure at  $80^\circ\text{C}$ , X70 steel, 1.5 bar  $\text{CO}_2$ , pH 6.6,  $\tau= 35$  Pa for the first 2 days,  $\tau= 535$  Pa for another 3 days.

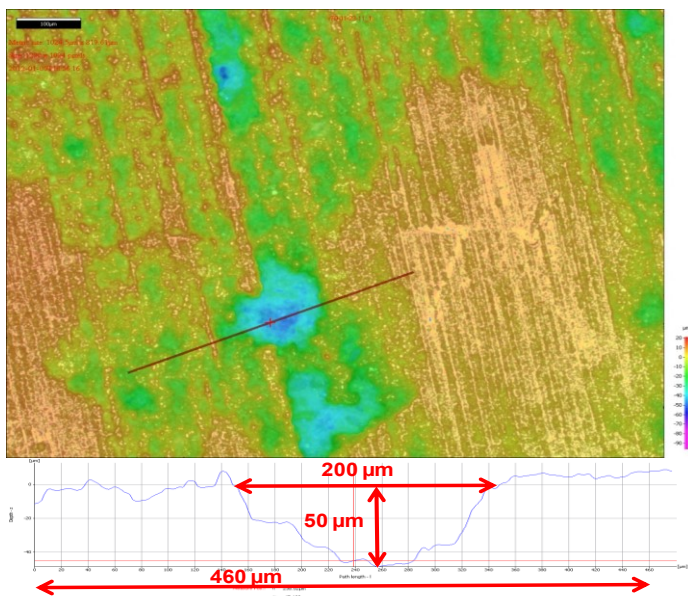


Figure 47: IFM image of de-scaled sample after 5 days of exposure at 80°C, X70 steel, 1.5 bar CO<sub>2</sub>, pH 6.6,  $\tau= 35$  Pa for the first 2 days,  $\tau= 535$  Pa for another 3 days, Size of the deepest pit is 200 $\mu\text{m}$  in width & 50  $\mu\text{m}$  in depth.

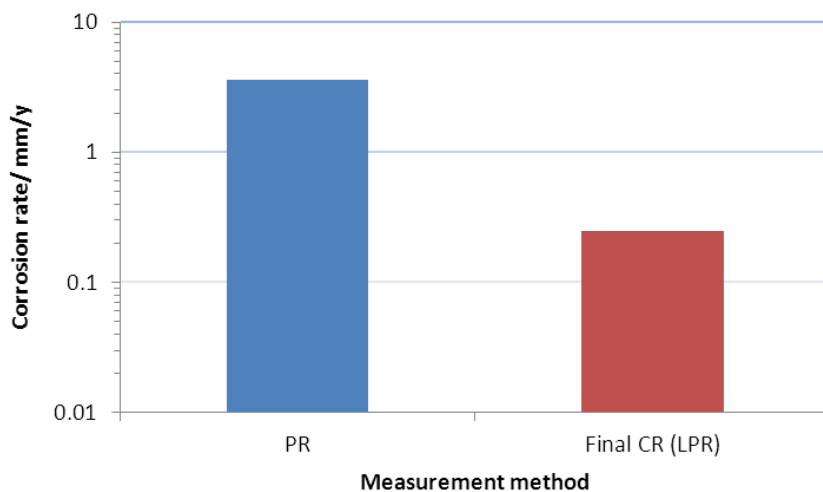


Figure 48: Comparison between the final corrosion rate measured by LPR and penetration rate of the deepest pit on each steel (PR) after 5 days of exposure at 80°C, X70 steel, 1.5 bar CO<sub>2</sub>, pH 6.6, B=26 mV/decade,  $\tau= 35$  Pa for the first 2 days,  $\tau= 535$  Pa for another 3 days.

- X70 steel, without initial  $\text{Fe}^{2+}$  addition:

Because X70 steel in the previous test suffered from local breakdown of the  $\text{FeCO}_3$  layer more than the other steels, a new experiment was conducted without initial addition of  $\text{FeCl}_2 \cdot 4\text{H}_2\text{O}$  to determine how this affects layer growth and if this enhances the protectiveness of the  $\text{FeCO}_3$  layer. From the previous test, the results show that the breakdown of the  $\text{FeCO}_3$  layer can be related to the topography of the surface.

When X70 is exposed to an environment with 1.5 bar  $\text{CO}_2$ , pH 6.6,  $80^\circ\text{C}$ , and without initial addition of  $\text{Fe}^{2+}$ , the  $\text{FeCO}_3$  layer took a longer time to completely cover the surface. Variation in the LPR corrosion rate values over time for the X70 material without initial addition of  $\text{Fe}^{2+}$  is shown in Figure 49. At the beginning, the corrosion rate was about 4.0 mm/y. During the  $\text{FeCO}_3$  layer formation, the corrosion rate gradually decreased until stabilizing at a value of less than 0.1 mm/y after about 7 days. After 8 days, when it was ensured that the entire surface is covered by an  $\text{FeCO}_3$  layer, the first sample was removed from the TCFC for surface characterization and the wall shear stress was increased to 535 Pa for 3 days more. Again, no increase in corrosion rate was measured by LPR after increasing wall shear stress. This indicates that the steel surface - remained fully covered by an  $\text{FeCO}_3$  layer.

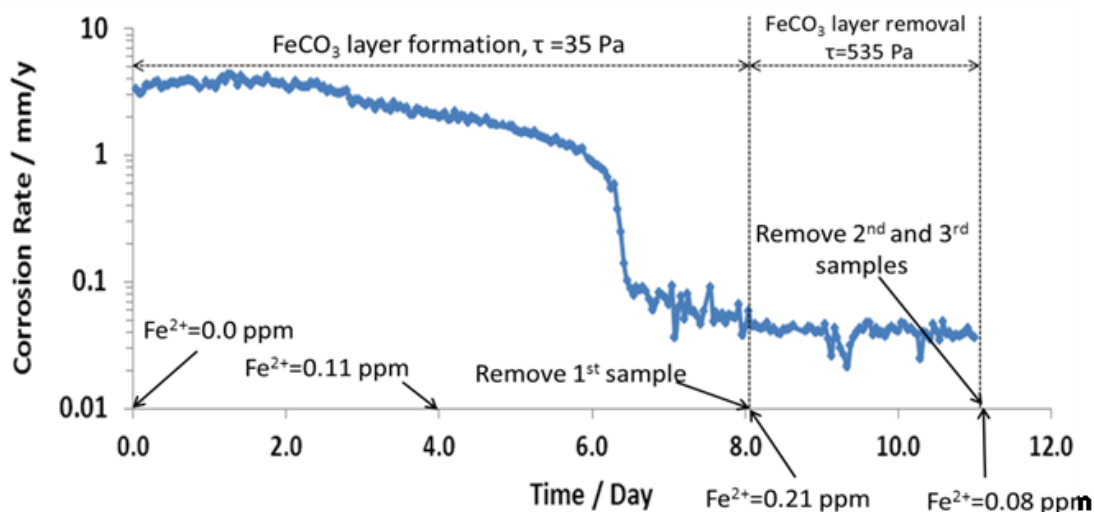


Figure 49: LPR Corrosion Rate of X70 steel (without initial  $\text{Fe}^{2+}$  additions) during 11 days of exposure at  $80^\circ\text{C}$ , 1.5 bar  $\text{CO}_2$ , pH 6.6,  $B=26$  mV/decade,  $\tau=35$  Pa for the first 8 days,  $\tau=535$  Pa for another 3 days.

The top surface and cross-section analysis by SEM and EDS upon removal of the samples from the system after 8 days of exposure show that the sample was fully covered with an  $\text{FeCO}_3$  layer and the thickness of the layer was much higher than the one formed with initial addition of  $\text{Fe}^{2+}$ . Figure 50 and Figure 51 show the comparison between the  $\text{FeCO}_3$  that formed with and without addition of  $\text{Fe}^{2+}$  ions.

After 11 days of exposure the average corrosion rate measured by weight loss was found to be 1.0 mm/y, Figure 52, which was almost the same as obtained from the integration in time of the LPR data (1.4 mm/y). The images that were taken by SEM and EDS upon removal of the samples from the system after 11 days of exposure show that the sample was still fully covered with the  $\text{FeCO}_3$  layer, and there is not any noticeable breakdown. Figure 53 and Figure 54, show a comparison between the effect of high wall shear stress on the  $\text{FeCO}_3$  layer that formed *with* and *without* initial addition of  $\text{Fe}^{2+}$ . This

comparison shows that the layer formed without addition of  $\text{Fe}^{2+}$  is more protective and better attached to the steel surface.

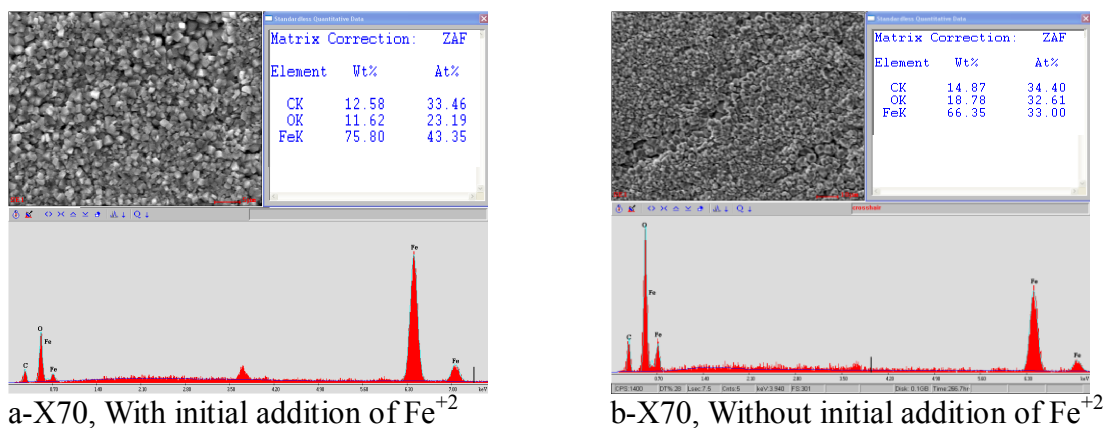


Figure 50: Comparison between SEM & EDS top surface analysis of  $\text{FeCO}_3$  layer at  $80^\circ\text{C}$ , X70 steel, 1.5 bar  $\text{CO}_2$ , pH 6.6,  $\tau= 35$  Pa for the  $\text{FeCO}_3$  layer formation.

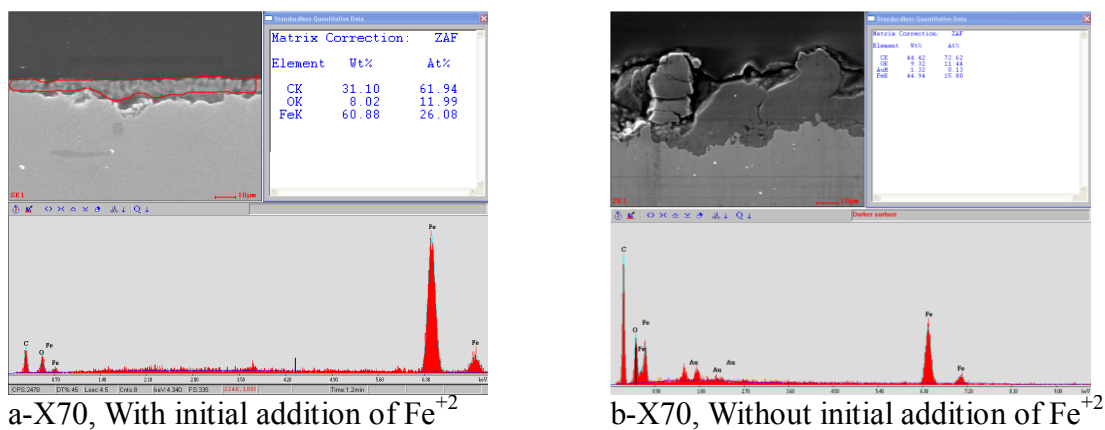


Figure 51: Comparison between SEM & EDS cross section analysis of  $\text{FeCO}_3$  layer at  $80^\circ\text{C}$ , X70 steel, 1.5 bar  $\text{CO}_2$ , pH 6.6,  $\tau= 35$  Pa for the  $\text{FeCO}_3$  layer formation.

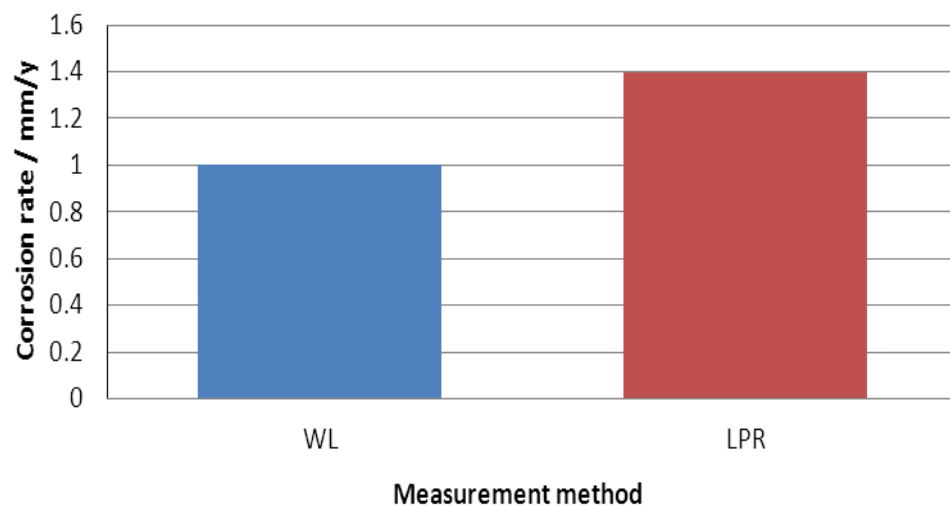


Figure 52: Comparison between corrosion rates measured by weight loss (WL) and integrated LPR (without initial  $\text{Fe}^{2+}$  additions), after 5 days of exposure at  $80^\circ\text{C}$ , X70 steel, 1.5 bar  $\text{CO}_2$ , pH 6.6,  $B=26$  mV/decade,  $\tau=35$  Pa for the  $\text{FeCO}_3$  layer formation,  $\tau=535$  Pa for the  $\text{FeCO}_3$  layer removal.

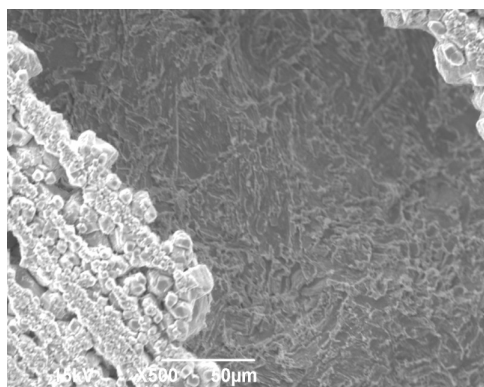
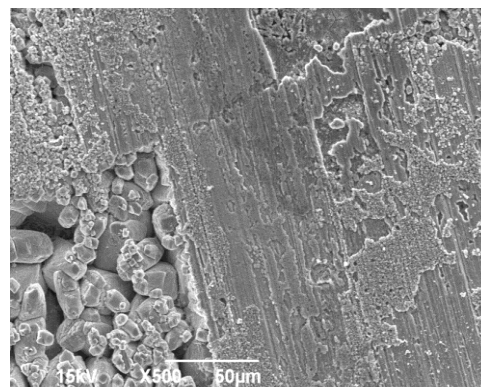
a-X70, With initial addition of  $\text{Fe}^{+2}$ b-X70, Without initial addition of  $\text{Fe}^{+2}$ 

Figure 53: Comparison between SEM top surface analysis of  $\text{FeCO}_3$  layer At  $80^\circ\text{C}$ , X70 steel, 1.5 bar  $\text{CO}_2$ , pH 6.6,  $\tau = 35$  Pa for the  $\text{FeCO}_3$  layer formation,  $\tau = 535$  Pa for the  $\text{FeCO}_3$  layer removal.

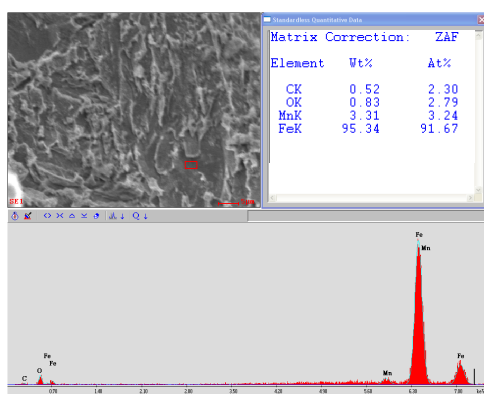
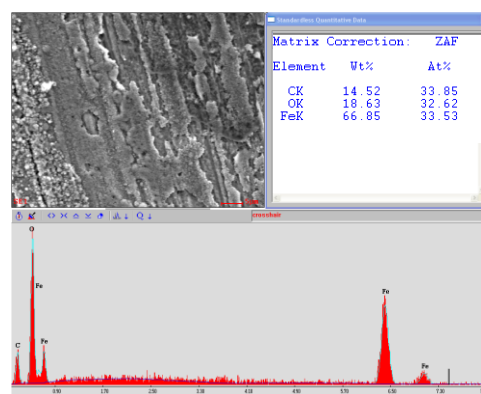
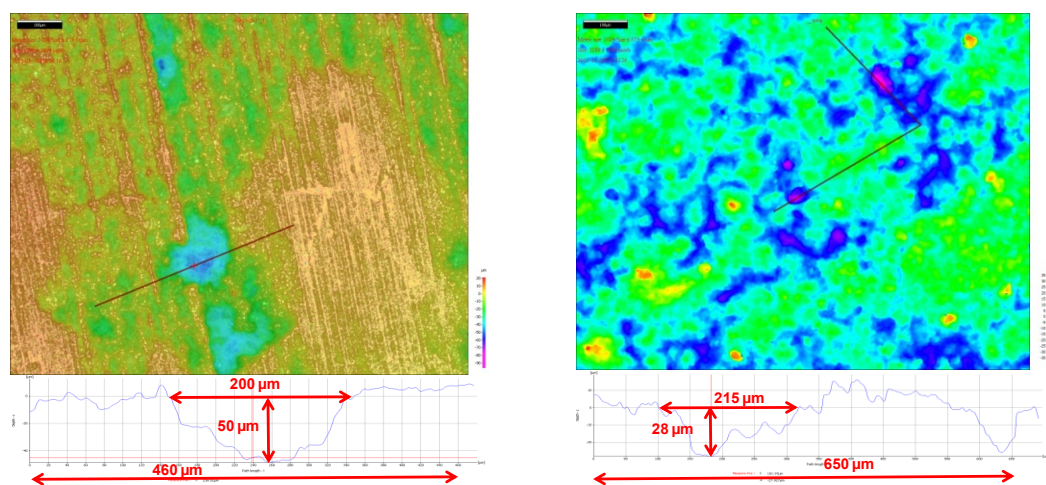
a-X70, With initial addition of  $\text{Fe}^{+2}$ b-X70, Without initial addition of  $\text{Fe}^{+2}$ 

Figure 54: Comparison between SEM & EDS top surface analysis of  $\text{FeCO}_3$  layer at  $80^\circ\text{C}$ , X70 steel, 1.5 bar  $\text{CO}_2$ , pH 6.6,  $\tau = 35$  Pa for the  $\text{FeCO}_3$  layer formation,  $\tau = 535$  Pa for the  $\text{FeCO}_3$  layer removal.

Additionally, the IFM analysis of the sample after de-scaling the sample shows a few corroded zones with different sizes. Figure 55 shows the deepest pit found with 28  $\mu\text{m}$  in depth and about 215  $\mu\text{m}$  in width, which is equal to a pit penetration rate of 0.9 mm/y. These pits could be classified as localized corrosion since the pit penetration rate

is still higher than final corrosion rate, which is 0.03 mm/y. Figure 56 shows the LPR final corrosion rates compared with the deepest pit penetration rate.



a-X70, With initial addition of  $\text{Fe}^{2+}$

b-X70, Without initial addition of  $\text{Fe}^{2+}$

Figure 55: Comparison between IFM images of descaled sample at  $80^\circ\text{C}$ , X70 steel, 1.5 bar  $\text{CO}_2$ , pH 6.6,  $\tau = 35$  Pa for the  $\text{FeCO}_3$  layer formation,  $\tau = 535$  Pa for the  $\text{FeCO}_3$  layer removal. Size of the deepest pit  $200\mu\text{m}$  in width &  $50\mu\text{m}$  in depth.

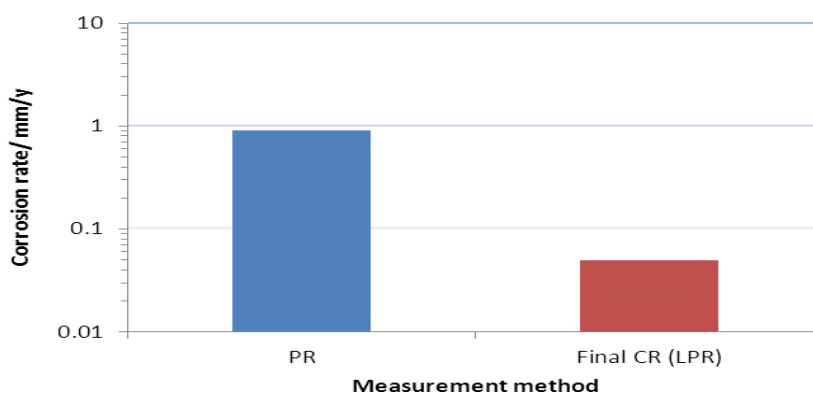


Figure 56: Comparison between corrosion rates of X70 steel without addition of  $\text{Fe}^{2+}$ , measured by weight loss (WL), integrated LPR, and penetration rate of the deepest pit on each steel (PR) after 5 days of exposure at  $80^\circ\text{C}$ , 1.5 bar  $\text{CO}_2$ , pH 6.6,  $B=26$  mV/decade,  $\tau = 35$  Pa for the  $\text{FeCO}_3$  layer formation,  $\tau = 535$  Pa for the  $\text{FeCO}_3$  layer removal.

- X65II steel:

For this particular hot rolled steel, after high wall shear stress was applied on the previously formed  $\text{FeCO}_3$  layer, pitting corrosion higher than seen on the other steels was observed. This phenomenon could be initiated even before increasing the wall shear stress. So another experiment was conducted under the same conditions and using the same procedure to determine if pitting was caused as a result of the high wall shear stress or if it was due to metallurgical factors such as the presence of inclusions.

Variation of the LPR corrosion rate of X65II with exposure time is shown in Figure 57. At the beginning, the corrosion rate was high (4-5 mm/y); during the  $\text{FeCO}_3$  layer formation, the corrosion rate gradually reduced until reaching 0.1 mm/y after about 40 hours and remained the same during the remaining exposure time. After 2 days, the first sample was removed from the TCFC in order to characterize the developed  $\text{FeCO}_3$  layer. The wall shear stress was then increased to 535 Pa for the remainder of the experiment. However, no increase in corrosion rate measured by LPR was noted after 2 days. This indicates that the steel surface remained fully covered by an  $\text{FeCO}_3$  layer.

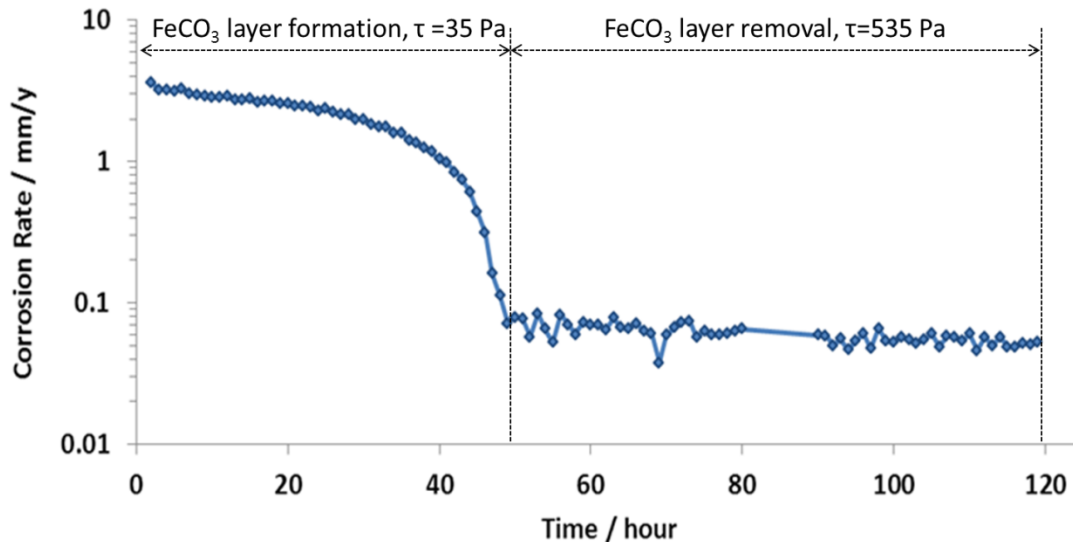
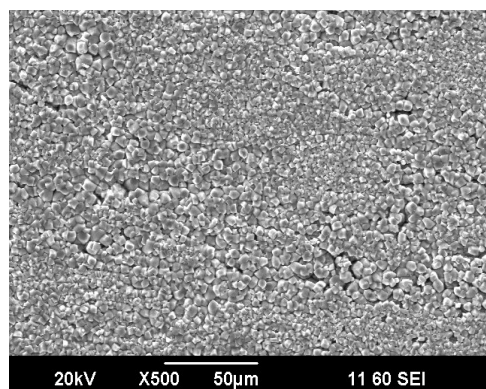


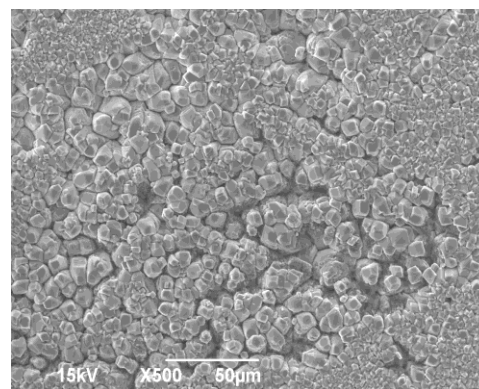
Figure 57: LPR Corrosion rate of X65II steel during 5 days of exposure at 80°C, 1.5 bar CO<sub>2</sub>, pH 6.6, B=26 mV/decade,  $\tau= 35$  Pa for the FeCO<sub>3</sub> layer formation,  $\tau= 35$  Pa for the first 2 days,  $\tau= 535$  Pa for another 3 days.

Analysis of the images that were taken by IFM and SEM (with EDS) after 2 and 5 days of exposure for both experiments (I & II) are shown below.

The SEM images that were taken after 2 days of exposure show that the sample was fully covered with an FeCO<sub>3</sub> layer see Figure 58 (Experiment I). The top surface and cross-section analysis by SEM and EDS also show the sample was fully covered with a FeCO<sub>3</sub> layer, see Figure 59 and Figure 60 (Experiment I). However, the top surface image in the second experiment shows that there were some voids or defects in the FeCO<sub>3</sub> layer, which indicate potential areas for localized corrosion to have occurred beneath the FeCO<sub>3</sub>.

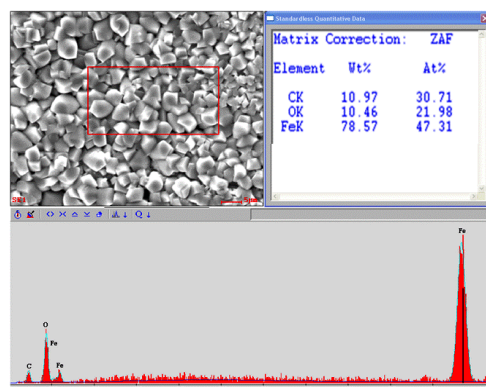


Experiment I

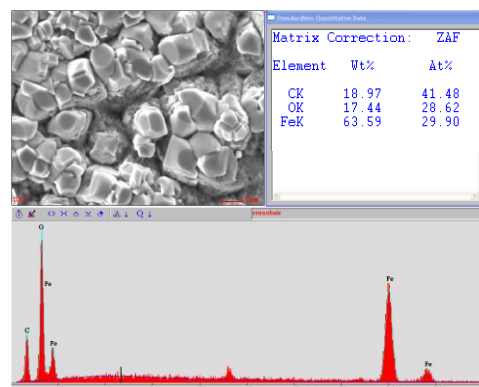


Experiment II

Figure 58: SEM top surface analysis of  $\text{FeCO}_3$  layer after 2 days of exposure at  $80^\circ\text{C}$ , X65II steel, 1.5 bar  $\text{CO}_2$ , pH 6.6,  $\tau = 35$  Pa for the first 2 days.



Experiment I



Experiment II

Figure 59: SEM & EDS top surface analysis of  $\text{FeCO}_3$  layer after 2 days of exposure at  $80^\circ\text{C}$ , X65II steel, 1.5 bar  $\text{CO}_2$ , pH 6.6,  $\tau = 35$  Pa for the first 2 days.

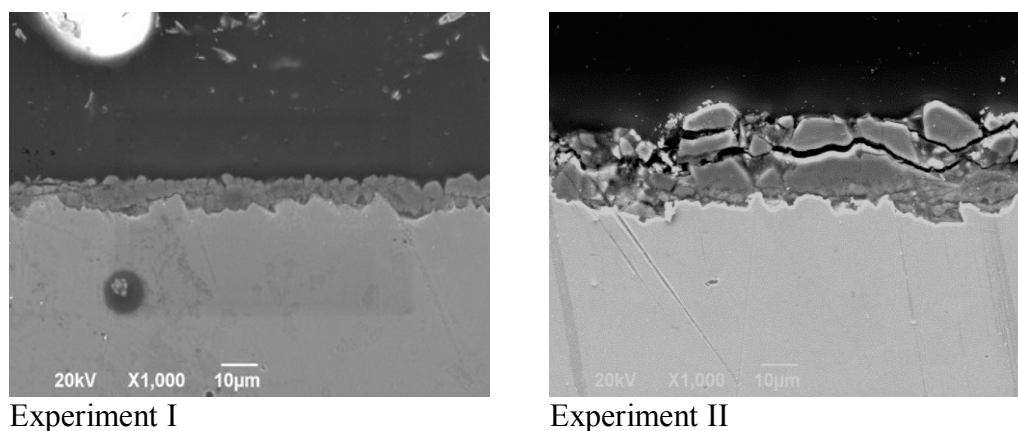


Figure 60: SEM & EDS cross section analysis of  $\text{FeCO}_3$  layer after 2 days of exposure at  $80^\circ\text{C}$ , X65II steel, 1.5 bar  $\text{CO}_2$ , pH 6.6,  $\tau= 35$  Pa for the first 2 days.

In addition to the top and cross-section analyses, the IFM analysis of the sample in the second experiment, conducted after descaling, shows several pits with different sizes. Figure 61 shows a pit with  $35 \mu\text{m}$  in depth and  $275 \mu\text{m}$  in width. This indicates that the pitting initiated before increasing the wall shear stress.

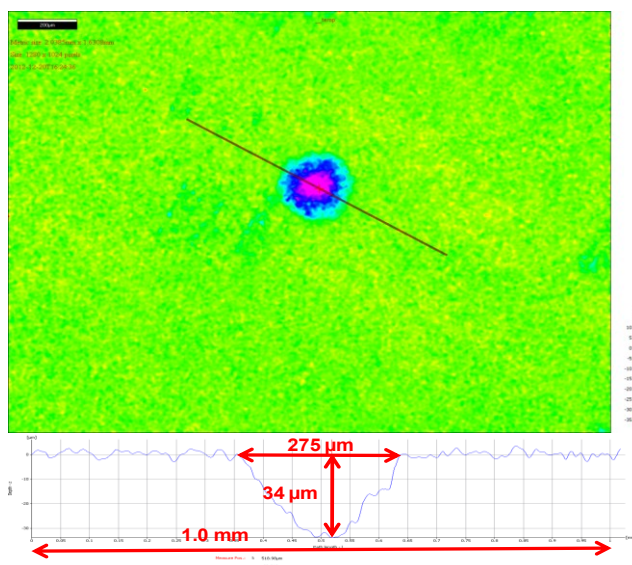


Figure 61: Experiment II, IFM image of  $\text{FeCO}_3$  layer after 2 days of exposure at  $80^\circ\text{C}$ , X65II steel, 1.5 bar  $\text{CO}_2$ , pH 6.6,  $\tau= 35$  Pa.

After 5 days of exposure, the two remaining samples were removed and the weight loss corrosion rate was found to be 1.3 mm/y, as shown in Figure 62. This was almost the same as obtained from the integration over time of the LPR data (0.9 mm/y). From the first experiment, it was found that X65II suffered from severe pitting corrosion after 5 days of exposure. Figure 67 shows a pit with 80  $\mu\text{m}$  in depth that is equivalent to a 5.8 mm/y pit penetration rate, which is very high compared to other steels. In the second experiment, one sample was removed after two days of exposure at low wall shear stress to conduct IFM analysis of sample after descaling.

The images that were taken by SEM upon removal of the samples from the system after 5 days of exposure show that the samples remained mostly covered by an  $\text{FeCO}_3$  layer, as shown in Figure 63. However, the comparison of SEM images before, Figure 58, and after, Figure 63, the increase in wall shear stress shows that the  $\text{FeCO}_3$  layer degraded after the exposure at high wall shear stress showing more voids or defects. Analysis of a void zone in the  $\text{FeCO}_3$  layer by EDS is consistent with the steel (Fe) substrate material. This indicates that the hole may have provided bulk solution access to the metal surface, Figure 64. The cross section analysis by SEM of both experiments show pits, especially in the sample tested in experiment II, including a large pit that is 100  $\mu\text{m}$  in depth and 300  $\mu\text{m}$  in width, Figure 65.

As shown in chapter 4, the microstructure of the X65II consists of banded ferrite-pearlite as a consequence of the manufacturing process, which produces light colored bands of ferrite and some dark bands of pearlite with some inclusions. It is possible that

this feature may be related to the occurrence of localized corrosion as was found by other studies [29].

In addition to the top and cross-section analyses, the IFM analysis of the samples in both experiments after descaling show that the deepest pit (Experiment II) was with 110  $\mu\text{m}$  in depth and about 250  $\mu\text{m}$  in width, see Figure 66. As shown in Figure 67, the penetration rate of the average deepest pits (in Experiment I, II) was compared with final corrosion rate that measured by LPR, where the final corrosion rate is assumed to be the actual corrosion rate for longer periods of exposure. Here the deepest pit penetration rate is calculated to be 6.9 mm/y, which is much higher than the final LPR corrosion rate which is 0.1 mm/y.

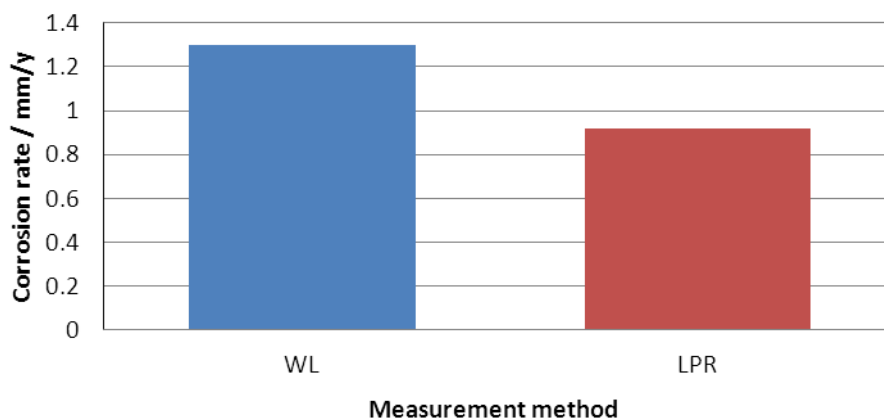
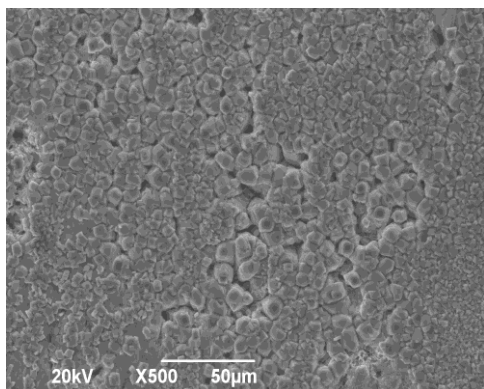
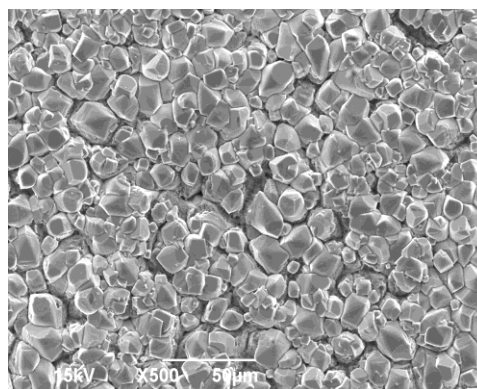


Figure 62: Comparison between corrosion rates measured by weight loss (WL) and integrated LPR after 5 days of exposure (Experiment I), at 80°C, X65II steel, 1.5 bar CO<sub>2</sub>, pH 6.6, B=26 mV/decade,  $\tau= 35$  Pa for the FeCO<sub>3</sub> layer formation,  $\tau= 35$  Pa for the first 2 days,  $\tau= 535$  Pa for another 3 days.

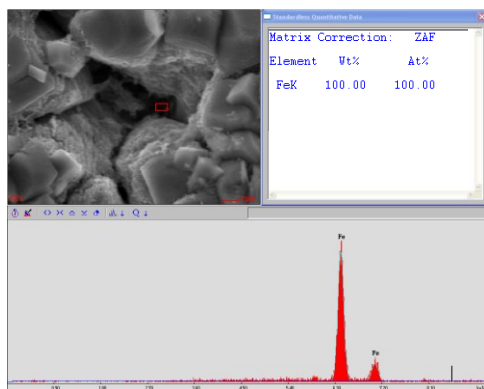


Experiment I

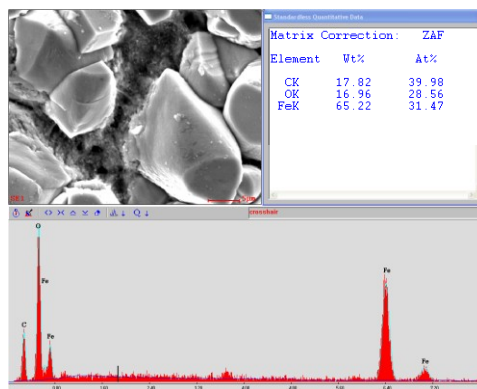


Experiment II

Figure 63: SEM top surface analysis of  $\text{FeCO}_3$  layer after 5 days of exposure at  $80^\circ\text{C}$ , X65II steel, 1.5 bar  $\text{CO}_2$ , pH 6.6,  $\tau = 35$  Pa for the first 2 days,  $\tau = 535$  Pa for another 3 days.

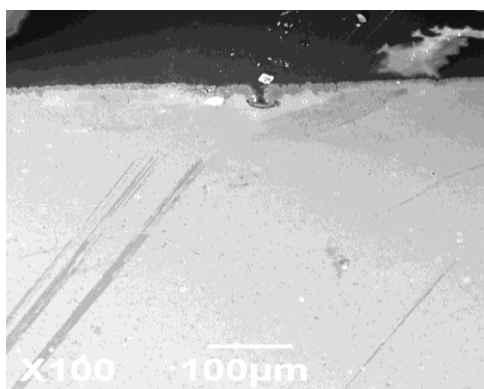


Experiment I

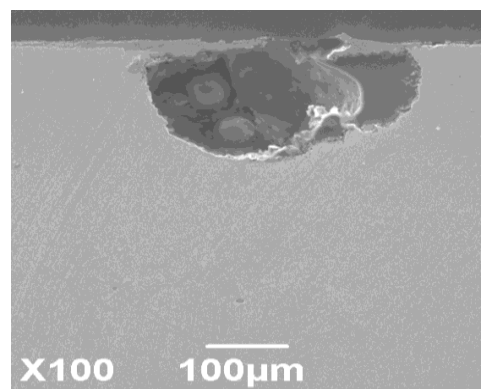


Experiment II

Figure 64: SEM& EDS top surface analysis of  $\text{FeCO}_3$  layer after 5 days of exposure at  $80^\circ\text{C}$ , X65II steel, 1.5 bar  $\text{CO}_2$ , pH 6.6,  $\tau = 35$  Pa for the first 2 days,  $\tau = 535$  Pa for another 3 days.

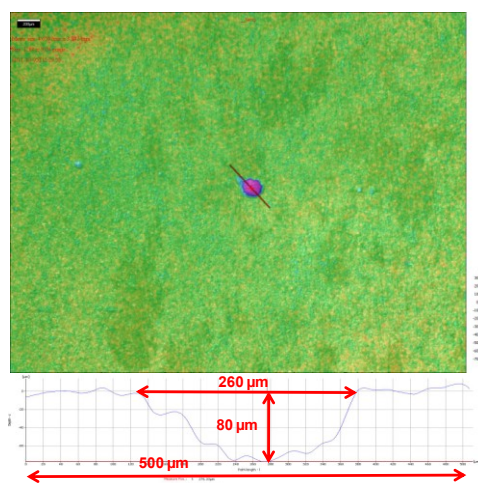


Experiment I

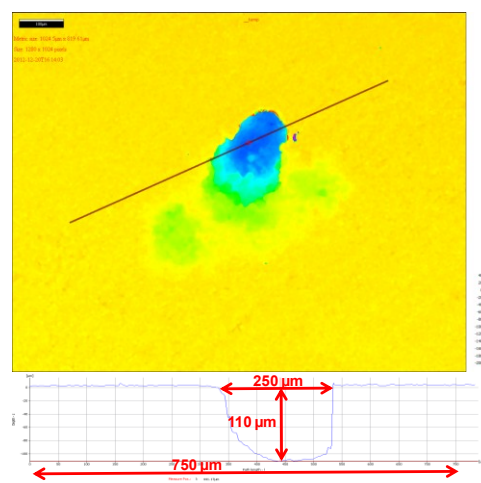


Experiment II

Figure 65: SEM cross section analysis of  $\text{FeCO}_3$  layer after 2 days of exposure at  $80^\circ\text{C}$ , X65II steel, 1.5 bar  $\text{CO}_2$ , pH 6.6,  $\tau = 35$  Pa for the first 2 days,  $\tau = 535$  Pa for another 3 days.



Experiment I



Experiment II

Figure 66: IFM image of descaled sample after 5 days of exposure at  $80^\circ\text{C}$ , X65II steel, 1.5 bar  $\text{CO}_2$ , pH 6.6,  $\tau = 35$  Pa for the first 2 days,  $\tau = 535$  Pa for another 3 days. Size of the deepest pit  $250\mu\text{m}$  in width &  $110\mu\text{m}$  in depth.

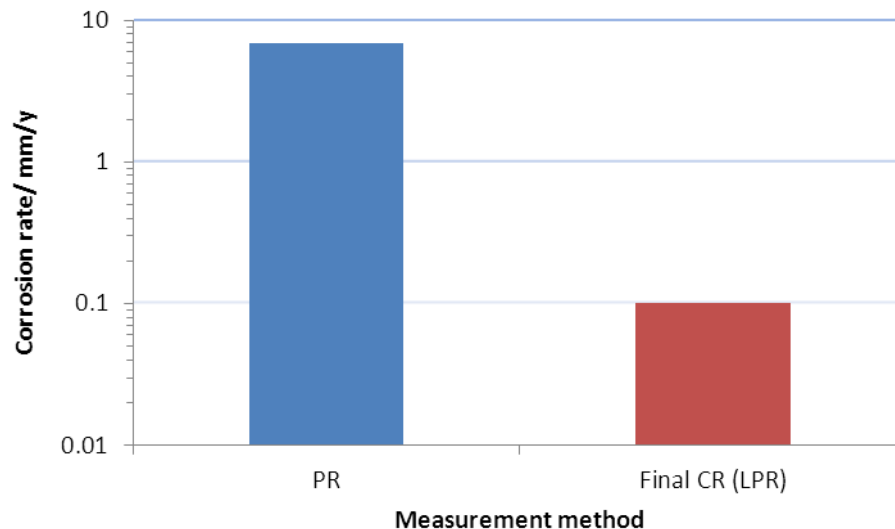


Figure 67: Comparison between corrosion rates measured by weight loss (WL), integrated LPR and average penetration rate of the deepest pits on each steel (Experiments I, II) (PR) after 5 days of exposure at 80°C, X65II steel, 1.5 bar CO<sub>2</sub>, pH 6.6, B =26 mV/decade,  $\tau = 35$  Pa for the first 2 days,  $\tau = 535$  Pa for another 3 days.

- X52 steel:

Variation of the LPR corrosion rate of X52 with exposure time is shown in Figure 68. At the beginning of the test, the corrosion rate was 3-4 mm/y. During the FeCO<sub>3</sub> layer formation process the corrosion rate gradually decreased until reaching 0.2 mm/y after about 44 hours; it remained the same during the next 4 hours of exposure. After 2 days, the first sample was removed from the TCFC in order to characterize the developed FeCO<sub>3</sub> layer. Then the wall shear stress was increased to 535 Pa for the remainder of the experiment. No significant increase in corrosion rate was measured by LPR during the last 3 days of the experiment. This indicates that the steel surface remained mostly covered by a protective FeCO<sub>3</sub> layer.

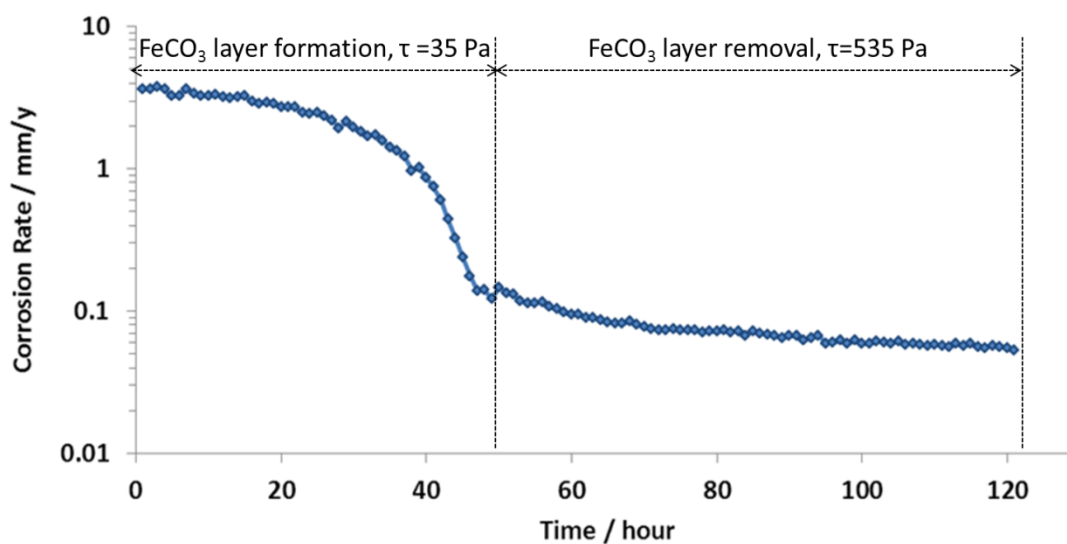


Figure 68: LPR corrosion rate of X52 steel during 5 days of exposure at 80°C, 1.5 bar CO<sub>2</sub>, pH 6.6, B=26 mV/decade,  $\tau=35$  Pa for the first 2 days,  $\tau=535$  Pa for another 3 days.

The images that were taken by SEM upon removal of the samples from the system after the first 2 days of exposure show that the sample was fully covered with a dense FeCO<sub>3</sub> layer as seen in Figure 69. Top surface and cross-section analyses by SEM and EDS also show the sample was fully covered with an FeCO<sub>3</sub> layer, see Figure 70 and Figure 71.

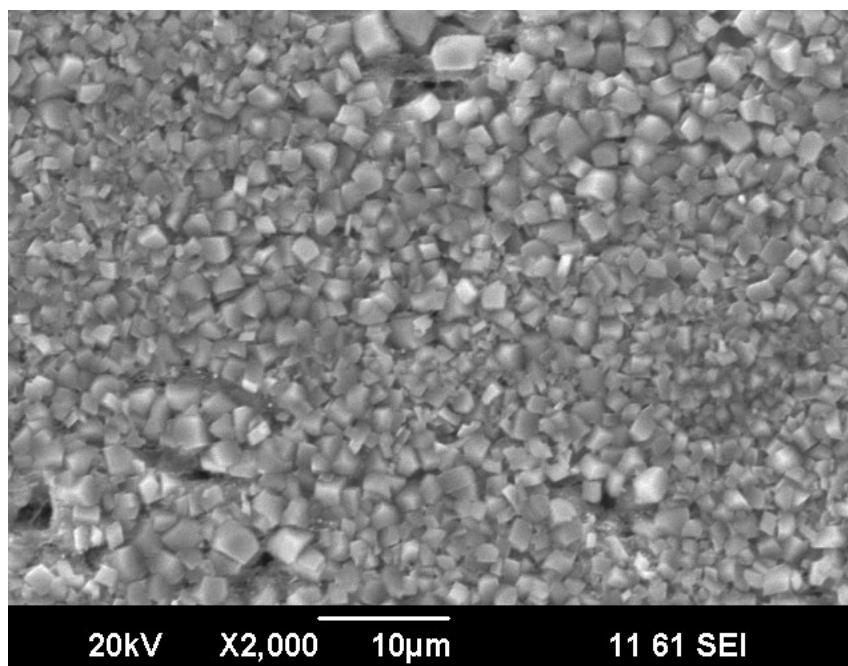


Figure 69: SEM top surface analysis of  $\text{FeCO}_3$  layer after 2 days of exposure at  $80^\circ\text{C}$ , X52 steel, 1.5 bar  $\text{CO}_2$ , pH 6.6,  $\tau = 35$  Pa.

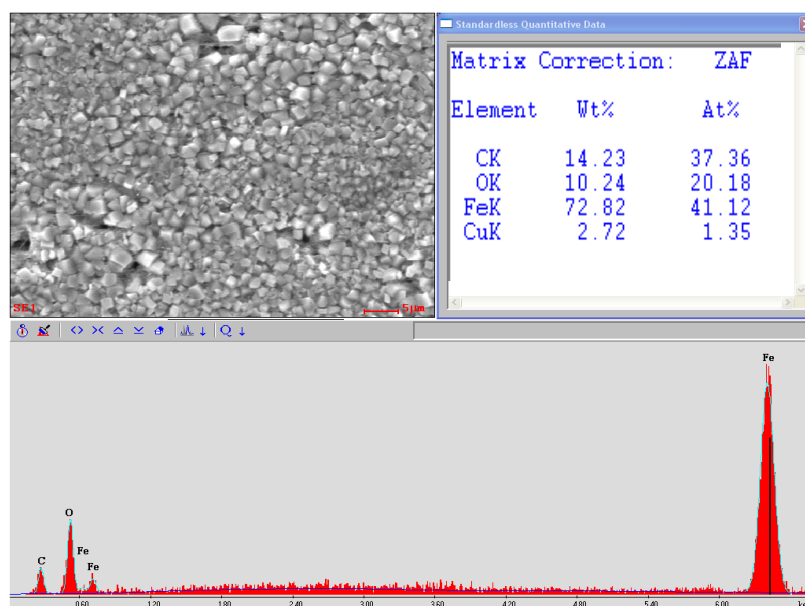


Figure 70: SEM & EDS top surface analysis of  $\text{FeCO}_3$  layer after 2 days of exposure at  $80^\circ\text{C}$ , X52 steel, 1.5 bar  $\text{CO}_2$ , pH 6.6,  $\tau = 35$  Pa.

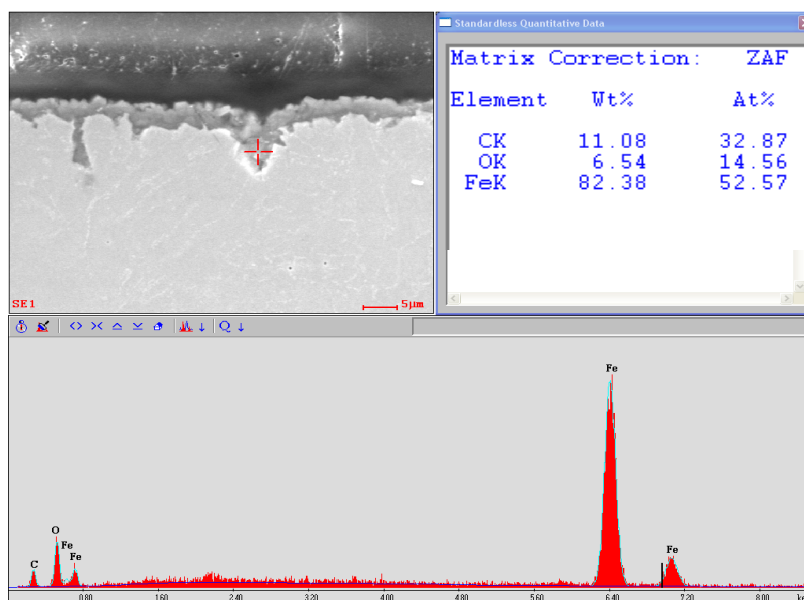


Figure 71: SEM& EDS cross section analysis of  $\text{FeCO}_3$  layer after 2 days of exposure at  $80^\circ\text{C}$ , X52 steel, 1.5 bar  $\text{CO}_2$ , pH 6.6,  $\tau = 35$  Pa for the first 2 days.

After 5 days of exposure, the two remaining samples were removed and the weight loss corrosion rate was found to be 0.8 mm/y, as shown in Figure 72, this was almost the same as obtained from the integration in time of the LPR data (0.6 mm/y).

Images that were taken by SEM and EDS upon removal of the samples from the system after 5 days of exposure showed that the sample remained mostly covered by a dense  $\text{FeCO}_3$  layer, as shown in Figure 73 and Figure 74, respectively. However, the comparison of SEM images before and after the increase in wall shear stress shows that the  $\text{FeCO}_3$  layer after wall shear stress increase, Figure 73, contains more voids or holes compared with the sample before the wall shear stress increase, Figure 69. In addition to the top and cross-section analysis, the IFM analysis of the sample after de-scaling shows few pits with different sizes. Figure 75, shows the deepest pit with 12  $\mu\text{m}$  in depth and about 400  $\mu\text{m}$  in width. As shown in Figure 76, the penetration rate of the deepest pit was

compared with final corrosion rate that measured by LPR. Here the deepest pit penetration rate is calculated to be 0.9 mm/y, which is still high compared with the final LPR corrosion rate which is 0.1 mm/y.

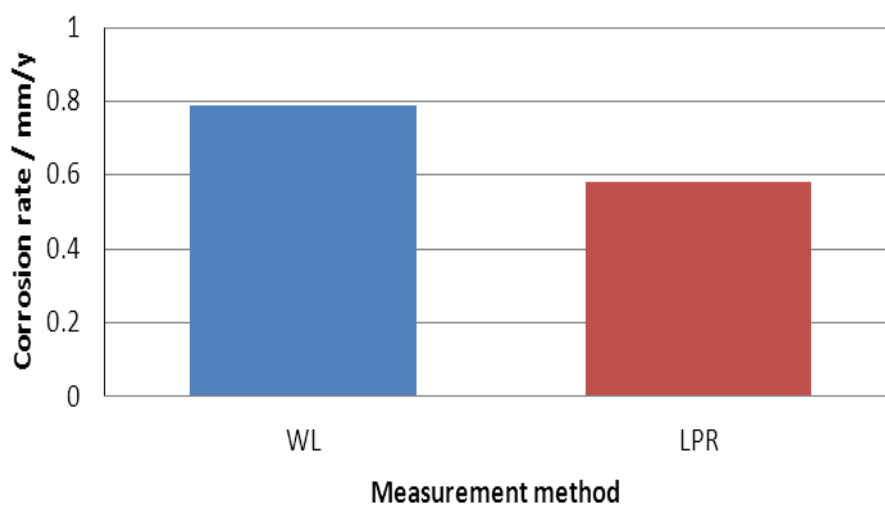


Figure 72: Comparison between corrosion rates measured by weight loss (WL) and integrated LPR after 5 days of exposure at 80°C, X52 steel, 1.5 bar CO<sub>2</sub>, pH 6.6, B=26 mV/decade,  $\tau = 35$  Pa for the first 2 days,  $\tau = 535$  Pa for another 3 days.

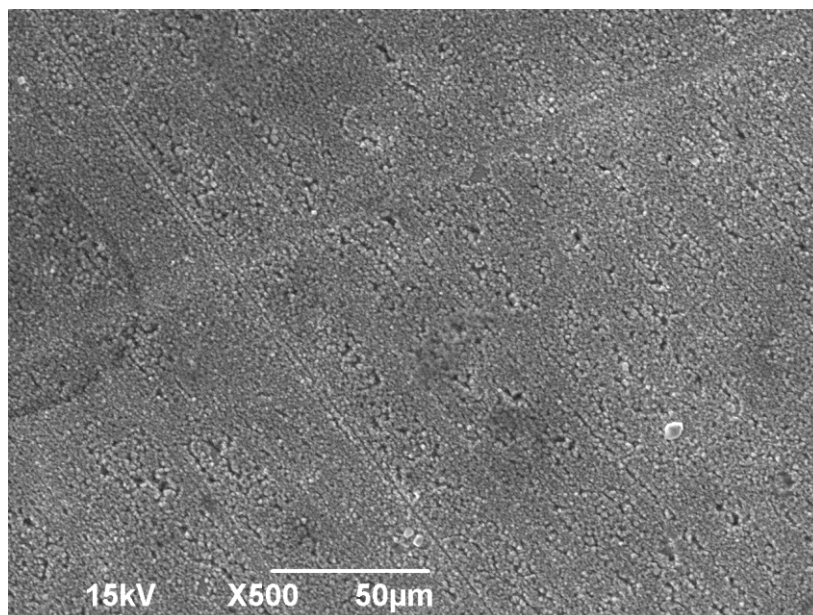


Figure 73: SEM top surface analysis of  $\text{FeCO}_3$  layer after 5 days of exposure at  $80^\circ\text{C}$ , X52 steel, 1.5 bar  $\text{CO}_2$ , pH 6.6,  $\tau=35$  Pa for the first 2 days,  $\tau=535$  Pa for another 3 days.

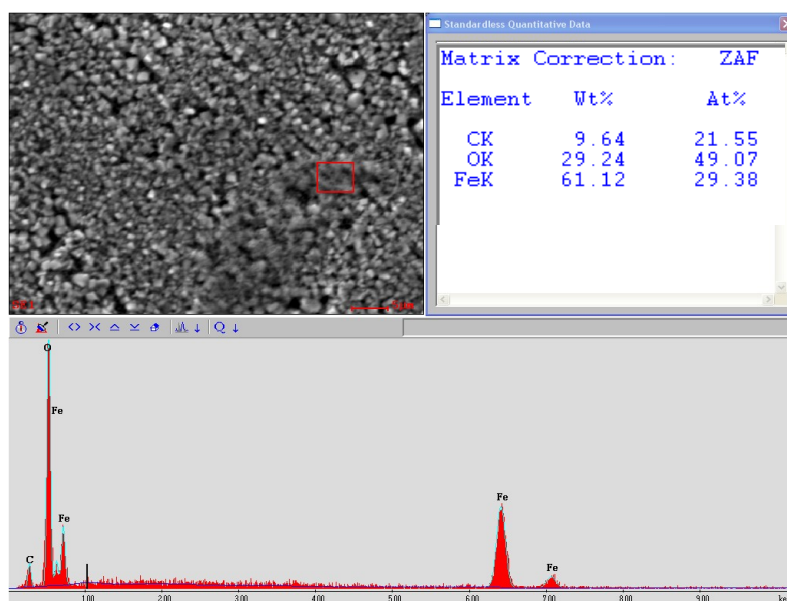


Figure 74: SEM & EDS top surface analysis of  $\text{FeCO}_3$  layer after 5 days of exposure at  $80^\circ\text{C}$ , X52 steel, 1.5 bar  $\text{CO}_2$ , pH 6.6,  $\tau=35$  Pa for the first 2 days,  $\tau=535$  Pa for another 3 days.

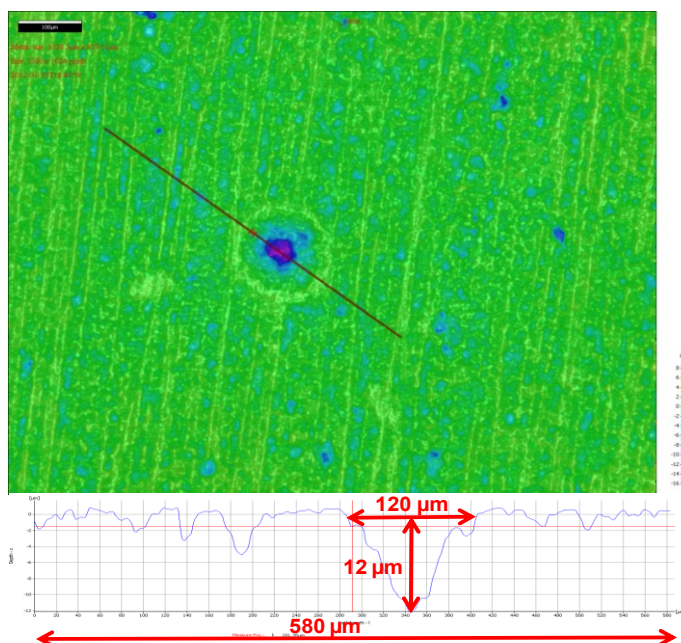


Figure 75: IFM image of de-scaled sample after 5 days of exposure at 80°C, X52 steel, 1.5 bar CO<sub>2</sub>, pH 6.6  $\tau= 35$  Pa for the first 2 days,  $\tau= 535$  Pa for another 3 days, Size of the deepest pit 120 $\mu$ m in width & 12  $\mu$ m in depth.

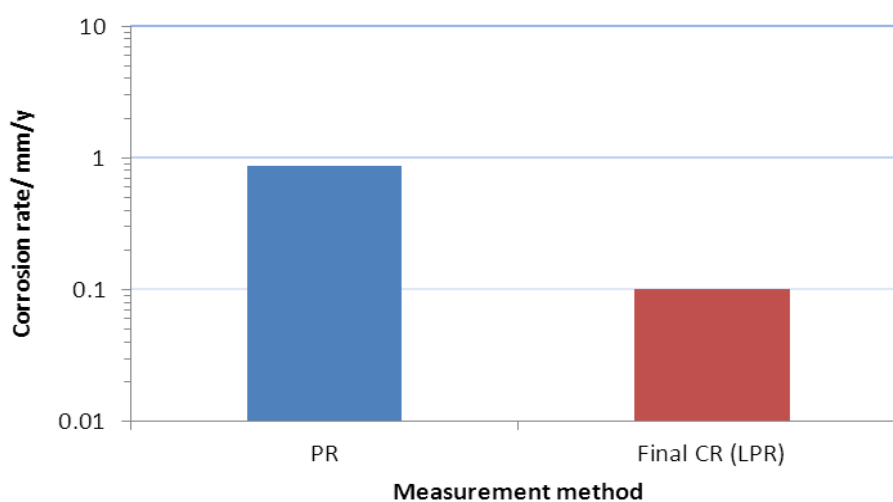


Figure 76: Comparison between corrosion rates measured by weight loss (WL), integrated LPR, and penetration rate of the deepest pit on each steel (PR) after 5 days of exposure at 80°C, X52 steel, 1.5 bar CO<sub>2</sub>, pH 6.6,  $B=26$  mV/decade,  $\tau= 35$  Pa for the first 2 days,  $\tau= 535$  Pa for another 3 days.

- A106GRB steel:

Variation of the LPR corrosion rate of A106GRB with exposure time is shown in Figure 77. At the beginning of the test, the corrosion rate was about 2.5-3.0 mm/y, during the  $\text{FeCO}_3$  formation process the corrosion rate reduced gradually until it reached less than 0.1 mm/y after about 24 hours; it remained the same during the next 24 hours of exposure. After two days, the first sample was removed from the TCFC in order to characterize the formed  $\text{FeCO}_3$  layer. After removal the first sample, the wall shear stress was increased to 535 Pa for the remainder of the experiment. After about 60 hours the corrosion rate increased slightly until reaching 0.5 mm/y; however, there were no indications that the  $\text{FeCO}_3$  layer was destroyed or removed.

The images taken by SEM and EDS upon removal of the samples from the system after 2 days of exposure show that the surface was fully covered with an  $\text{FeCO}_3$  layer, Figure 78 and Figure 79.

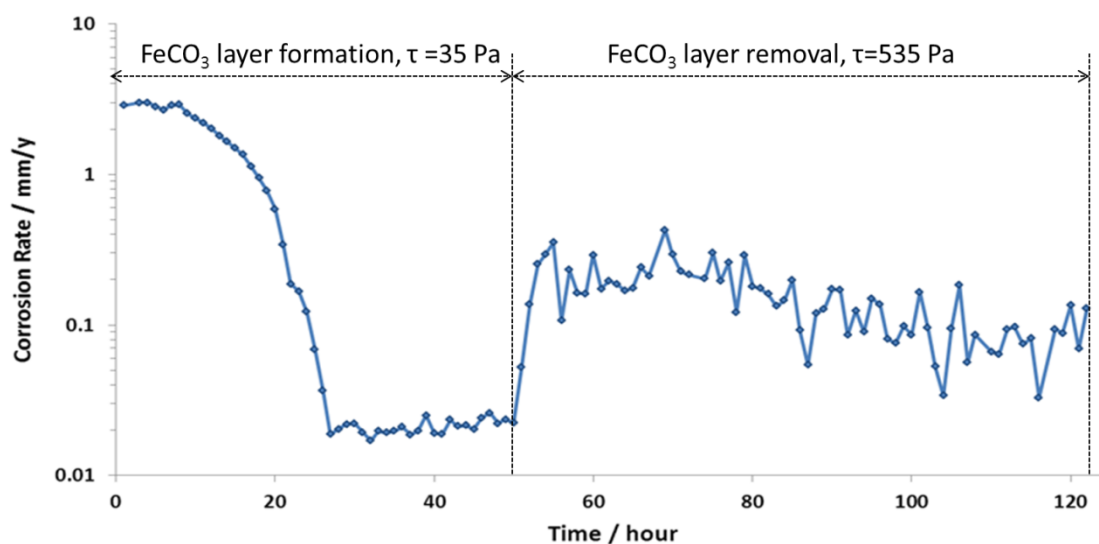


Figure 77: LPR corrosion rate during 5 days of exposure at 80°C, A106GRB steel, 1.5 bar CO<sub>2</sub>, pH 6.6, B=26 mV/decade,  $\tau = 35$  Pa for the first 2 days,  $\tau = 535$  Pa for another 3 days.

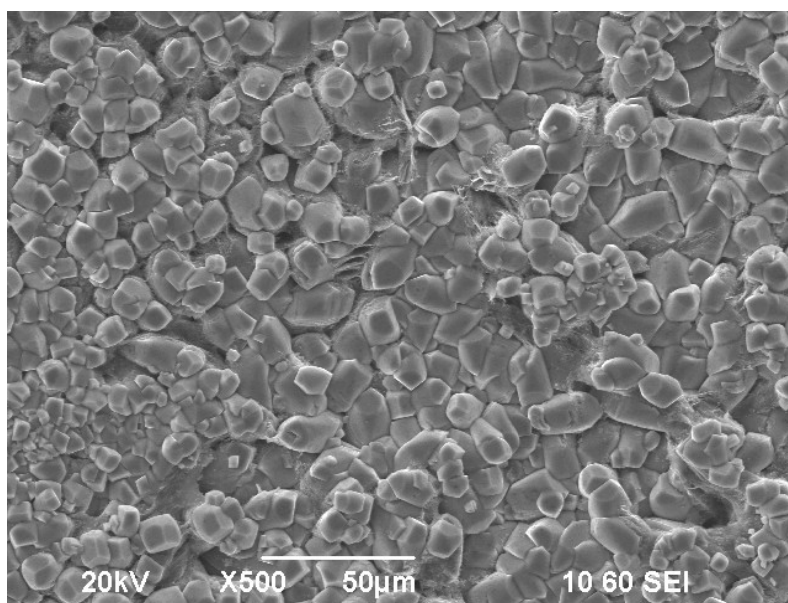


Figure 78: SEM top surface analysis of FeCO<sub>3</sub> layer after 2 days of exposure at 80°C, A106GRB steel, 1.5 bar CO<sub>2</sub>, pH 6.6,  $\tau = 35$  Pa.

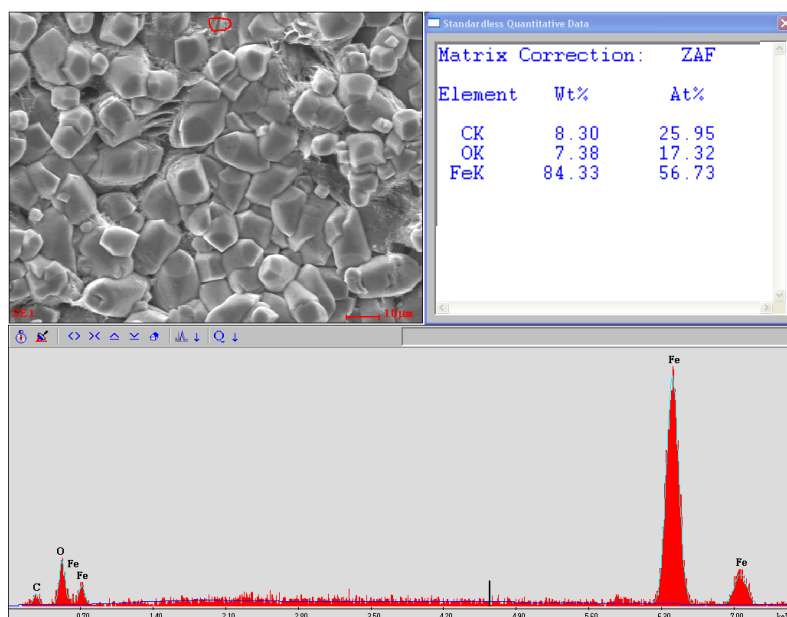


Figure 79: SEM & EDS top surface analysis of  $\text{FeCO}_3$  layer after 2 days of exposure at  $80^\circ\text{C}$ , A106GRB steel, 1.5 bar  $\text{CO}_2$ , pH 6.6,  $\tau = 35$  Pa.

In addition to the top surface analyses, the cross-section sample was etched with 2% Nital (nitric acid and alcohol) and analyzed using SEM to check for any relationship between the microstructure of the steel and the formed  $\text{FeCO}_3$  layer. Figure 80 shows that the sample was fully covered with a protective  $\text{FeCO}_3$  layer, and shows strips/lines of iron carbide extending from the steel substrate into the  $\text{FeCO}_3$  layer from the pearlite grains. This iron carbide structure is thought to enhance the adhesion of the layer at pearlitic surface regions.

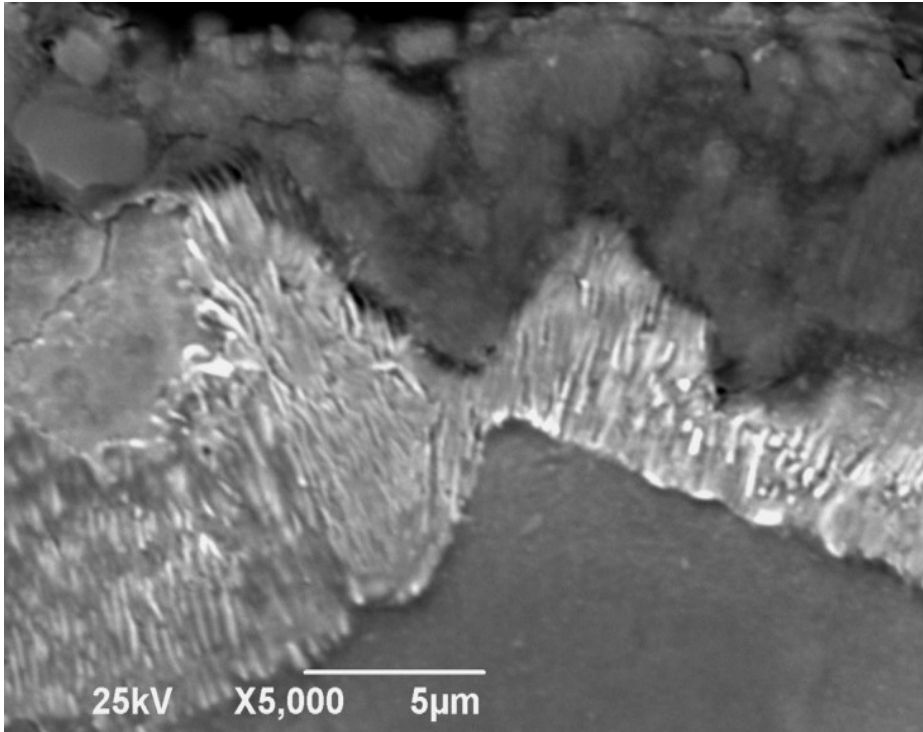


Figure 80: SEM of an etched cross section sample with  $\text{FeCO}_3$  layer & microstructure after 2 days of exposure at  $80^\circ\text{C}$ , A106GRB steel, 1.5 bar  $\text{CO}_2$ , pH 6.6,  $\tau = 35$  Pa.

After 5 days of exposure, the two remaining samples were removed and the weight loss corrosion rate was found to be  $0.75$  mm/y, as shown in Figure 81. This was almost the same as obtained from the integration in time of the LPR data ( $0.65$  mm/y).

The images that were taken by SEM upon removal of the sample from the system after five days of exposure show that the sample was fully covered with an  $\text{FeCO}_3$  layer, Figure 82. This sample was taken after increasing wall shear stress and contains more voids than the sample that was taken before increasing wall shear stress, Figure 78. The top surface and cross-section analyses by SEM and EDS also show that the sample was fully covered by an  $\text{FeCO}_3$  layer, Figure 83 and Figure 84. Additionally, the IFM analysis of the sample after descaling shows small pits with different sizes, Figure 85. As shown

in Figure 86, the penetration rate of the deepest pit was compared to the final corrosion rate measured by LPR. Here the deepest pit penetration rate is calculated to be 2.3 mm/y. The deepest pit penetration rate is very large as compared to the final corrosion rate measured by LPR, which is 0.2 mm/y, where the final corrosion rate is assumed to be the actual corrosion rate for longer periods of time.

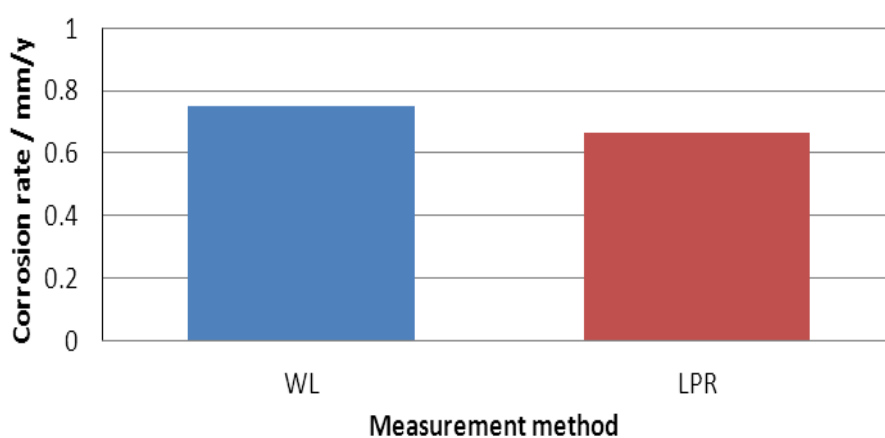


Figure 81: Comparison between corrosion rates measured by weight loss (WL) and integrated LPR after 5 days of exposure at 80°C, A106GRB steel, 1.5 bar CO<sub>2</sub>, pH 6.6, B=26 mV/decade,  $\tau$ = 35 Pa for the first 2 days,  $\tau$ = 535 Pa for another 3 days.

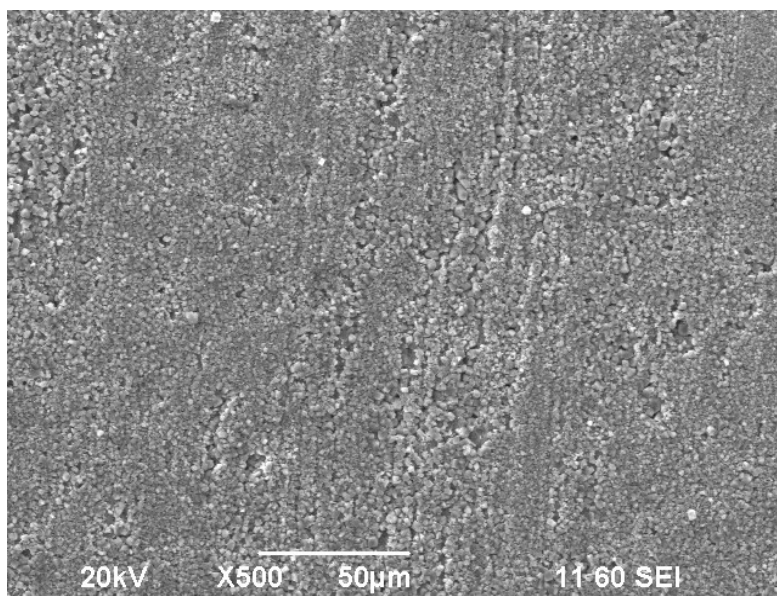


Figure 82: SEM top surface analysis of  $\text{FeCO}_3$  layer after 5 days of exposure at  $80^\circ\text{C}$ , A106GRB steel, 1.5 bar  $\text{CO}_2$ , pH 6.6,  $\tau= 35$  Pa for the first 2 days,  $\tau= 535$  Pa for another 3 days.

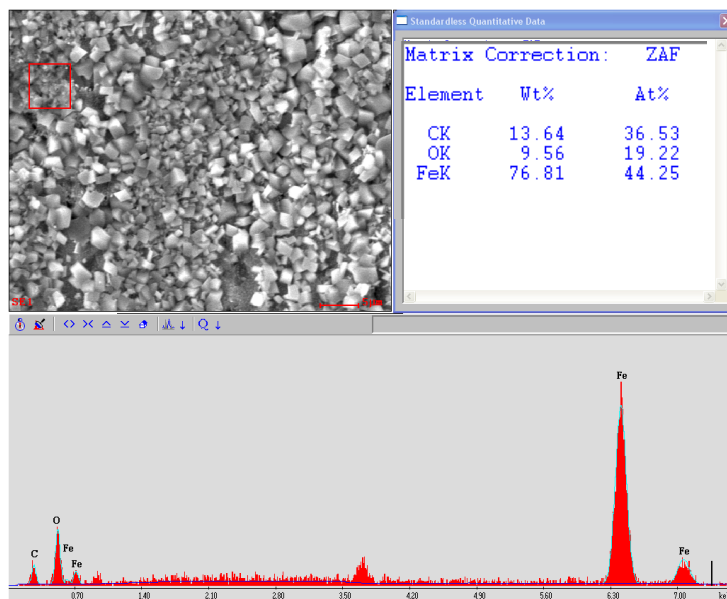


Figure 83: SEM& EDS top surface analysis of  $\text{FeCO}_3$  layer after 5 days of exposure at  $80^\circ\text{C}$ , A106GRB steel, 1.5 bar  $\text{CO}_2$ , pH 6.6,  $\tau= 35$  Pa for the first 2 days,  $\tau= 535$  Pa for another 3 days.

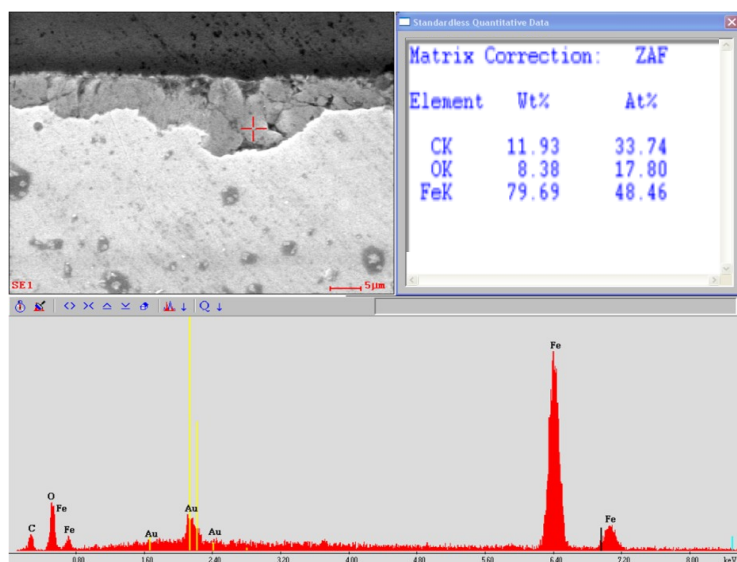


Figure 84: SEM& EDS cross section analysis of  $\text{FeCO}_3$  layer after 5 days of exposure at  $80^\circ\text{C}$ , A106GRB steel, 1.5 bar  $\text{CO}_2$ , pH 6.6,  $\tau = 35$  Pa for the first 2 days,  $\tau = 535$  Pa for another 3 days.

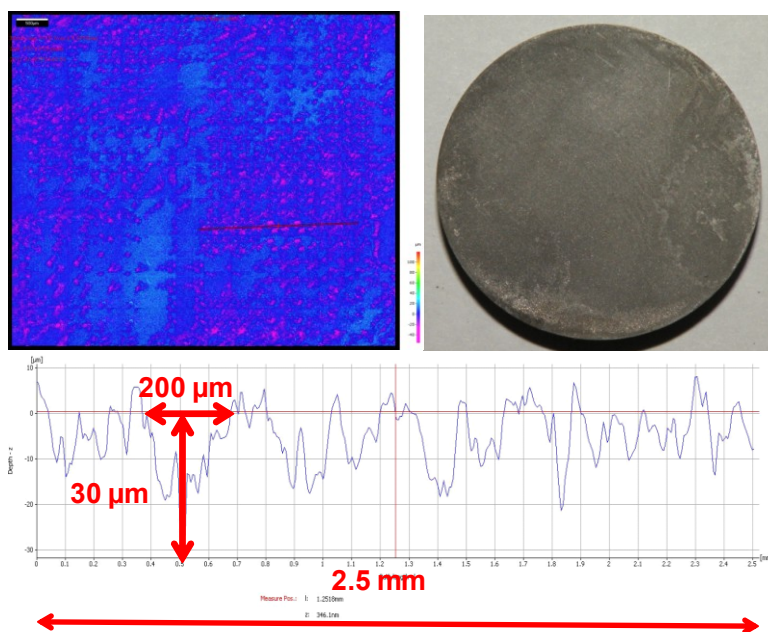


Figure 85: IFM image of de-scaled sample after 5 days of exposure at  $80^\circ\text{C}$ , A106GRB steel, 1.5 bar  $\text{CO}_2$ , pH 6.6,  $\tau = 35$  Pa for the first 2 days,  $\tau = 535$  Pa for another 3 days, Size of the deepest pit 200 $\mu\text{m}$  in width & 30  $\mu\text{m}$  in depth.

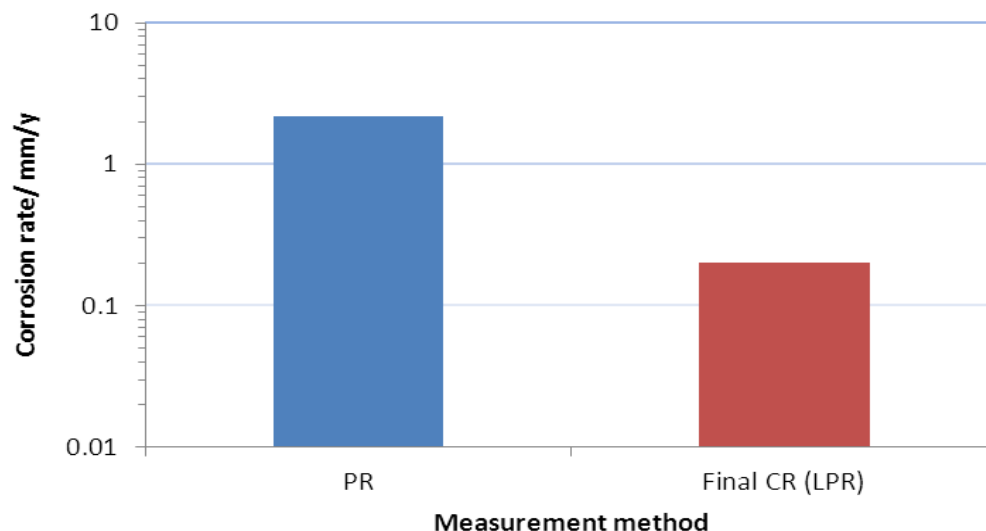


Figure 86: Comparison between corrosion rates measured by weight loss (WL), integrated LPR, and penetration rate of the deepest pit on each steel (PR) after 5 days of exposure at 80°C, A106GRB steel, 1.5 bar CO<sub>2</sub>, pH 6.6, B=26 mV/decade  $\tau = 35$  Pa for the first 2 days,  $\tau = 535$  Pa for another 3 days.

#### 6.3.4 Summary

As shown from the results above, all steels suffered from partial loss of the protective FeCO<sub>3</sub> layer when high wall shear stress, with a magnitude of 535 Pa, was applied. This magnitude of wall shear stress should be insufficient to cause breakdown of the FeCO<sub>3</sub> layer according to some previous studies [46], [47]. However, there are some authors that have reported the failure of FeCO<sub>3</sub> and induced localized corrosion initiated at low wall shear stresses below 0.2 Pa [45]. The observed breakdown of the FeCO<sub>3</sub> layer reported herein is thought to be caused by a fluctuation of forces (pressure and shear stress) relating to turbulent flow [45]. The effect of such fluctuating wall forces: local pressure and shear stresses on the formed corrosion product layer would be dependent on exposure time, the intergranular and/or intragranular strength of the FeCO<sub>3</sub> layer, and

adherence between  $\text{FeCO}_3$  and the steel surface. Fluctuating forces could cause mechanical fatigue of the  $\text{FeCO}_3$  crystals and lead to their detachment from each other and from the steel surface. The iron carbide content can play a role in improving the adherence of the  $\text{FeCO}_3$  to the steel surface and also its protectiveness, Figure 80. As shown in Figure 87, the  $\text{FeCO}_3$  formed on Q&T steels, which have relatively low carbon content (0.07 and 0.14 wt. % for X70 and X65I, respectively), can be clearly removed after applying high wall shear stress. This removal of  $\text{FeCO}_3$  results in exposure of steel to the corrosive environment. Besides, the high wall shear stress may contribute to the occurrence of localized corrosion in these areas due to the difficulty to reform the protective layer under high flow intensity [41]. On the other hand, the  $\text{FeCO}_3$  that formed on normalized steels, Figure 88, cannot be easily removed after applying high wall shear stress. However, breakdown of  $\text{FeCO}_3$  at small local areas occurred, which caused localized corrosion.

To clarify if steel suffered from localized or pitting corrosion, a comparison between the final general corrosion rates (measured by LPR) and pit penetration rates is shown in Figure 89. Although the pit penetration rates of normalized steels (X52, A106GRB) are lower than for Q&T steels (X65I, X70), the hot rolled normalized steel X65II has the largest pitting penetration rates, Figure 89, which could be related to the inhomogeneity of this microstructure caused by the segregation of carbon and other alloying elements during heat treatment [29], see Figure 14.

Regarding the effect of the chemistry of the testing solution, the  $\text{FeCO}_3$  layer formed on Q&T steel (X70) without addition of  $\text{Fe}^{2+}$  took a longer time to form.

However, it is more dense and protective than the one formed with a high initial concentration of  $\text{Fe}^{2+}$ . Thus, the initial concentration of  $\text{Fe}^{2+}$  could play an important role in promoting the protectiveness of the  $\text{FeCO}_3$  product layer. This issue will be further discussed in relation to proposed future work in the final chapter.

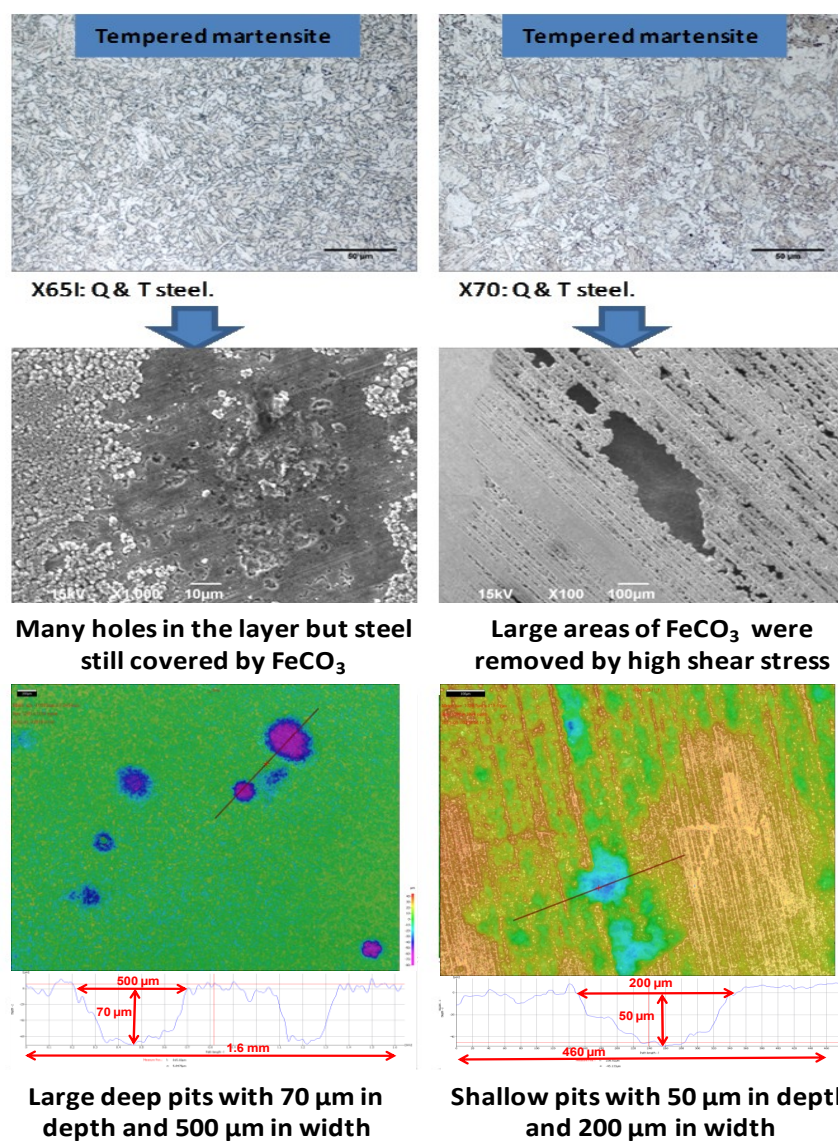


Figure 87: SEM & IFM (after Clarke solution) of Q&T steels (X65I, X70) after 5 days of exposure at 80°C, 1.5 bar  $\text{CO}_2$ , pH 6.6,  $B=26$  mV/decade,  $\tau=35$  Pa for the first 2 days,  $\tau=535$  Pa for another 3 days.

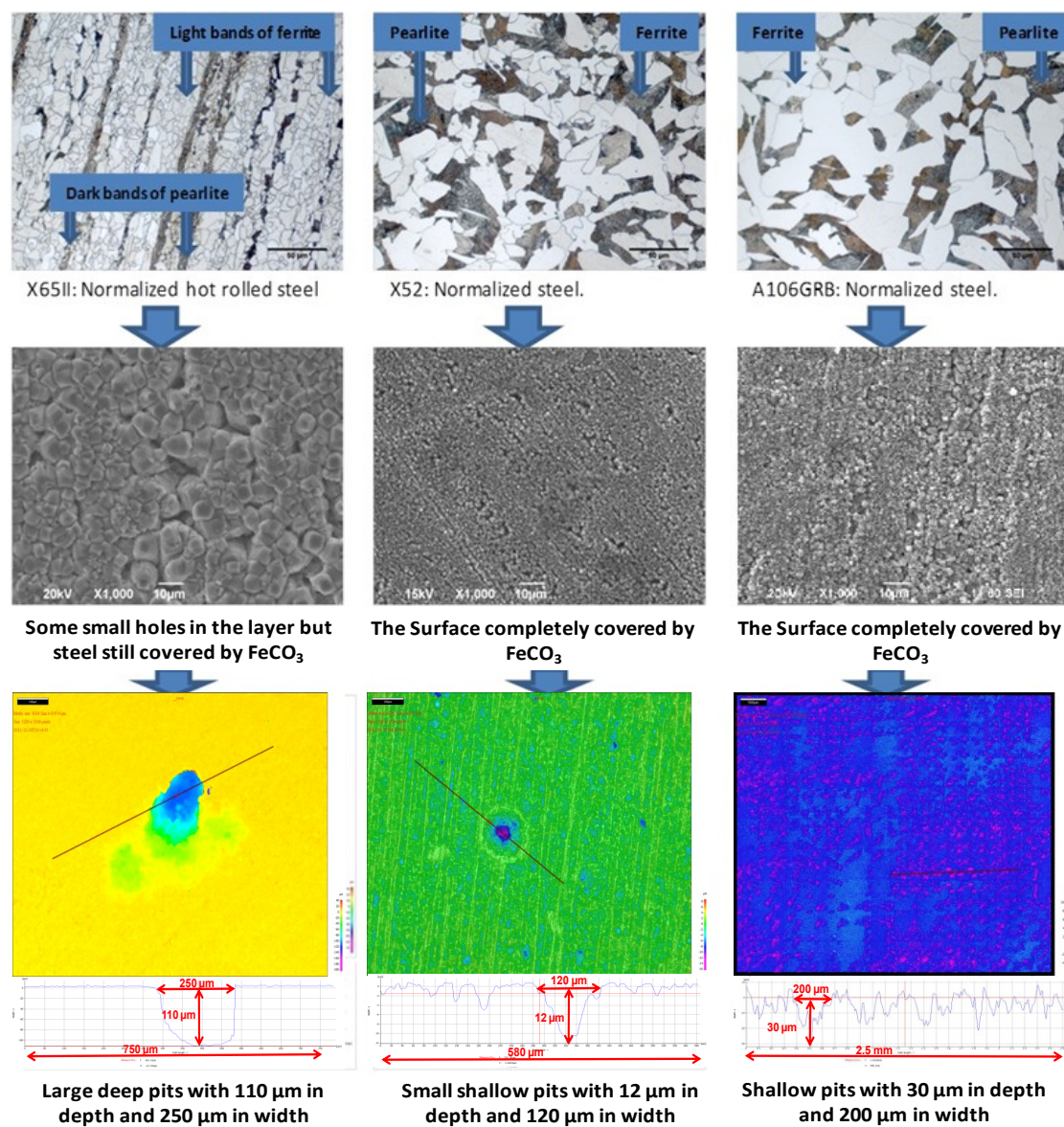


Figure 88: SEM & IFM (after Clarke solution) images of normalized steels (X65II, X52, A106GRB) after 5 days of exposure at 80°C, 1.5 bar  $\text{CO}_2$ , pH 6.6,  $B=26$  mV/decade,  $\tau=35$  Pa for the first 2 days,  $\tau=535$  Pa for another 3 days.

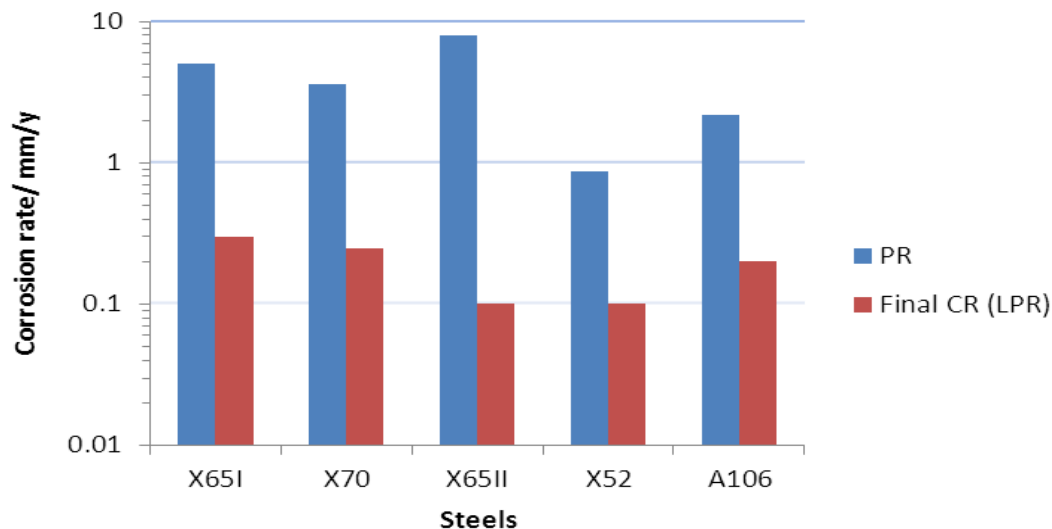


Figure 89: TCFC final corrosion rate measured by LPR & penetration rate (PR) of the deepest pit on each steel after 5 days of exposure at 80°C, 1.5 bar CO<sub>2</sub>, pH 6.6,  $\tau = 35$  Pa for the first 2 days,  $\tau = 535$  Pa for another 3 days.

### 6.3.5 Discussion

From the obtained results, the effect of chemical composition and microstructure may be separated according to two different mechanisms which are dependent on steel type:

I - FeCO<sub>3</sub> Layer Formed on Normalized Steel.

II - FeCO<sub>3</sub> Layer Formed on Q&T Steel.

- Mechanism I: FeCO<sub>3</sub> Layer Formed on Normalized Steel.

When the FeCO<sub>3</sub> layer is formed on normalized steels, which have ferrite-pearlite (F-P) microstructure, pearlite can play a major role on the protective properties and adherence of the FeCO<sub>3</sub> layer. Pearlite is a two-phased lamellar structure that is composed of alternating layers of  $\alpha$ -ferrite and cementite (iron carbide). Actually, the

individual lamellae within a colony are connected in three dimensions, so pearlite is in fact an interpenetrating bi-crystal of ferrite and cementite.

When steel is exposed to the CO<sub>2</sub> environment at supersaturation condition of CO<sub>2</sub>, the carbonate ion that is dissociated from bicarbonate ion will rapidly react with dissolved ferrous ion (Fe<sup>2+</sup>) in the bulk solution. The reaction product will be FeCO<sub>3</sub> as a corrosion product that will cover some areas of the surface. As the pearlite is composed of ferrite and iron carbide, the ferrite corrodes preferentially while the iron carbide that remains is still attached to the ferrite matrix and acts as preferential site for the cathodic reactions [22]. When the fluid is stagnant or the flow intensity is relatively low, the concentration of ferrous ions becomes high in the cavities between iron carbides which may favor the FeCO<sub>3</sub> crystal nucleation and growth within the iron carbide skeleton [30] enhancing the formation and the adhesion of the corrosion product layer on the steel surface. Also, the ferrite grains on the steel surface will rapidly corrode and the dissolved ferrous ion (Fe<sup>2+</sup>) will react with carbonate, from dissociated bicarbonate, to form an FeCO<sub>3</sub> layer that will cover the remaining surface area, as shown in Figure 90-a. This mechanism can lead to the formation of adherent and protective FeCO<sub>3</sub> layer, see Figure 90-b.

When a high flow rate, and thus a high wall shear stress, is applied on the FeCO<sub>3</sub> layers already formed on normalized steels (F-P microstructure), small areas of the FeCO<sub>3</sub> layer on ferrite grain locations may be removed since the attachment of the layer in these regions may be weaker than on pearlite grains, as shown in Figure 90-c. If local

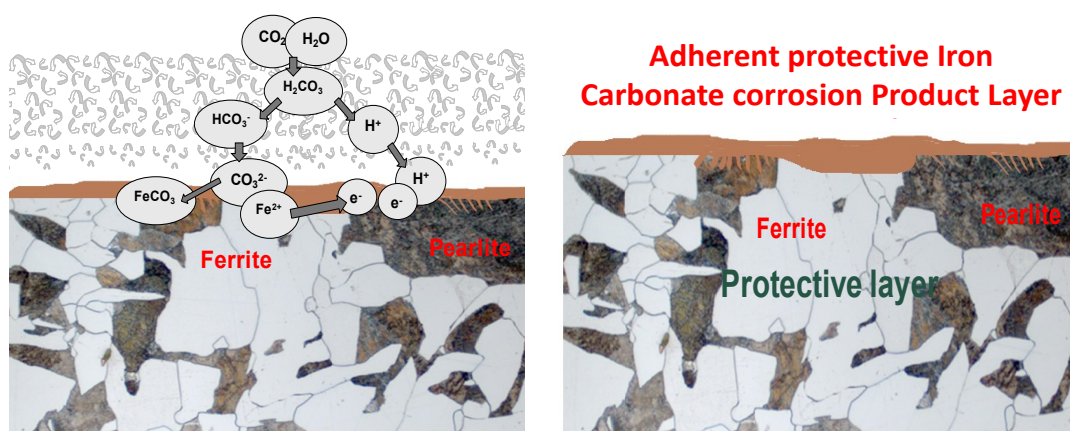
breakdown of the  $\text{FeCO}_3$  has occurred, this will contribute to the onset of localized corrosion, see Figure 90-d.

- Mechanism II:  $\text{FeCO}_3$  Layer Formed on Q&T Steel.

The  $\text{FeCO}_3$  layer formed on Q & T steels (tempered martensite microstructure) behave differently compared to the one formed on normalized steel when high wall shear stress is applied. In this case, the iron carbide phase in the steel exists as small carbide particles dispersed in the  $\alpha$ -ferrite matrix. During the period of  $\text{FeCO}_3$  layer formation (relatively high corrosion rate) the small carbide particles are not able to form a network or skeleton as in the case of the normalized steels. When this type of steel is exposed to the  $\text{CO}_2$  environment with supersaturation condition of  $\text{CO}_2$ , the carbonate that is dissociated from bicarbonate will rapidly react with dissolved ferrous ion ( $\text{Fe}^{2+}$ ) in the bulk solution. The reaction product will be  $\text{FeCO}_3$  as a corrosion product that will cover some areas of the surface. Uncovered regions of the steel surface will corrode and the dissolved ferrous ion at the steel surface ( $\text{Fe}^{2+}$ ) will react with carbonate that is dissociated from bicarbonate to form  $\text{FeCO}_3$  layer that will cover the remaining surface area, see Figure 91-a and Figure 91-b. Here the formed  $\text{FeCO}_3$  layer will not be in good contact with the steel surface, because no cavities within the iron carbide skeleton have developed, which assist in retention of the  $\text{FeCO}_3$ . However, at low flow rates, the  $\text{FeCO}_3$  will be protective and can't be easily removed.

When high wall shear stress is applied on a formed  $\text{FeCO}_3$  layer that grew on Q&T steels which have tempered martensite microstructure, large areas of  $\text{FeCO}_3$  will be removed at the areas where the  $\text{FeCO}_3$  is not in good contact with the steel surface. This

will be due to pressure and shear stress fluctuations in turbulent flow, see Figure 91-c. The large breakdown areas of  $\text{FeCO}_3$  will result in exposure of steel to the corrosive environment and the high flow rate will contribute to an increased localized corrosion, where the exposed areas selectively experience a higher corrosion rate than the rest of the surface, as shown in Figure 91-d.



a- Mechanism of  $\text{FeCO}_3$  formation on normalized steel at low wall shear stress

b- The result is adherent protective  $\text{FeCO}_3$  product that is stuck to surface

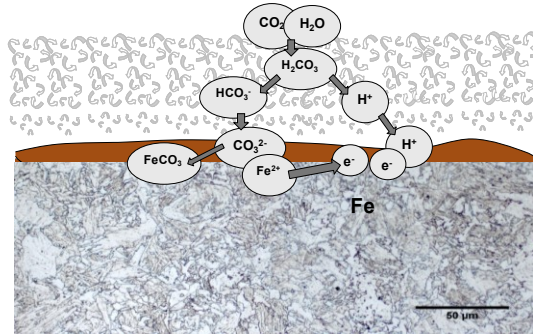


c- Local breakdown of  $\text{FeCO}_3$  caused by high wall shear stress



d- Localized corrosion where breakdown of  $\text{FeCO}_3$  areas (?? Not a complete idea or sentence)

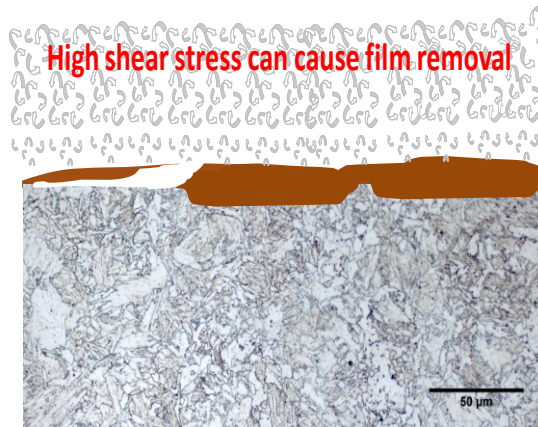
Figure 90: Mechanism of  $\text{FeCO}_3$  formations on normalized steel.



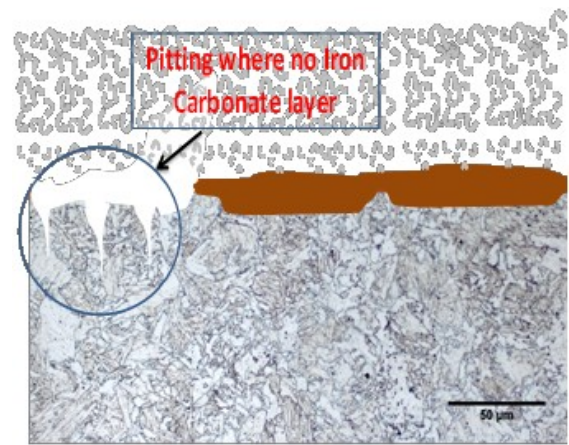
a- Mechanism of  $\text{FeCO}_3$  formation on Q & T steel at low wall shear stress



b- Protective iron carbonate product layer



c- Large areas of  $\text{FeCO}_3$  can be removed.



d- Pitting corrosion at the exposed area

Figure 91: Mechanism of  $\text{FeCO}_3$  formations on Q&T steel.

#### 6.4 Summary

- 1- Increasing the wall shear stress caused some locations of  $\text{FeCO}_3$  layer failure which has led to pitting.
- 2- The breakdown of  $\text{FeCO}_3$  layer is thought to be caused by fluctuating forces: pressure and shear stress in turbulence flow which led to fatigue type of failure.
- 3- The penetration rates of pitting in normalized steels (X52 & A106GRB) were much lower than Q & T steels (X65I & X70).

- 4- The low pit penetration rates in normalized steels can be related to the homogeneity of microstructure and the pearlite structures which help the layer “stick” to the steel surface.
- 5- The hot rolled steel X65II had the largest pitting penetration rates that could be due to inclusions.

## CHAPTER7: Determination of FeCO<sub>3</sub> Formation at High Wall Shear Stress

### 7.1 Introduction

In the previous chapter, results were presented where an FeCO<sub>3</sub> layer developed at a low wall shear stress was exposed to a much higher wall shear stress which caused local failures in the layer. In this chapter, experiments are described where the FeCO<sub>3</sub> layer was generated under a high wall shear stress from the very beginning of exposure to determine the influence high wall shear stress on FeCO<sub>3</sub> layer formation, adhesion and protection on various steel substrates.

FeCO<sub>3</sub> corrosion layer formation is dependent on temperature and the pH in bulk solution. In highly turbulent flow rapid species transport towards and away from the steel surface increases the rate at which hydrogen ions are replenished and ferrous ions are removed from the surface, respectively. This leads to an increase in the bare steel corrosion rate and will retard the precipitation of FeCO<sub>3</sub>.

### 7.2 Experimental Method

In each experiment, two weight loss samples and one electrochemical probe made from the same steels were tested in the TCFC, as shown in Figure 18 and described in details in APPENDIX C. In order to accelerate the formation of the FeCO<sub>3</sub> corrosion layer during experiments, the initial concentration of Fe<sup>2+</sup> ion was increased by addition of ferrous chloride tetrahydrate (FeCl<sub>2</sub>.4H<sub>2</sub>O), using the same procedure as was described in Chapter 6. After adjusting the concentration of Fe<sup>2+</sup> ions, temperature, and pH to the desired levels, as shown in Table 9, high wall shear stress (535 Pa) was generated upon

introduction of the samples to the TCFC system. The results of LPR, weight loss experiments, as well as SEM, and IFM analyses are shown below grouped by steel type.

At the end of the experiment, all samples were rinsed in isopropyl alcohol immediately upon removal from the system, and then dried and stored in a desiccator, which had an appropriate flow of nitrogen to facilitate desiccation and maintain deoxygenation, until analyses by infinite focus microscopy (IFM), scanning electron microscopy (SEM) and energy dispersive spectroscopy (EDS) were conducted. Corrosion rates were then calculated from the weight loss of each sample. Microscopy was then conducted to characterize corrosion behavior.

Table 9: Test Matrix: Determination of  $\text{FeCO}_3$  at High Wall Shear Stress ( $\tau = 535 \text{ Pa}$ ).

Parameters	Condition
Test time	3 days
Velocity	16 m/s
Wall shear stress	535 Pa
Temperature	80° C
Total Pressure	2.0 bar
CO <sub>2</sub> Partial pressure	1.5 bar
pH	6.6
Solution	1.0 wt.% NaCl
Material	X52, X65I, X65II, X70, A106 GRB
Measurement methods	LPR, WL
surface morphology	IFM, SEM and EDS
Initial $[\text{Fe}^{2+}]$ concentration	18-22 ppm

### 7.3 Results

For all steels tested, the LPR corrosion rates were in the range of 4-9 mm/y during the three days of exposure and no  $\text{FeCO}_3$  layers formed, see Figure 92.

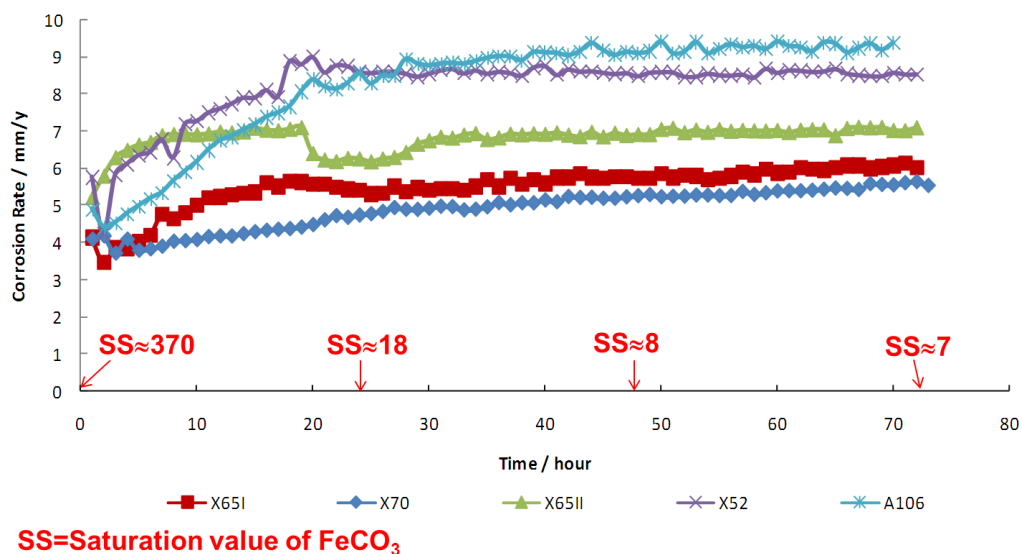


Figure 92: LPR measurement corrosion rates (CR) mm/y, five different steels, 3 days of exposure at  $80^\circ\text{C}$ , 1.5 bar  $\text{CO}_2$ , pH 6.6,  $B=26$  mV/decade,  $\tau = 535$  Pa.

- Q&T Steels, X65I & X70:

Variation of the LPR corrosion rate of Q&T steels with exposure time is shown in Figure 93. At the beginning of the test, the corrosion rate was 3.5-4.0 mm/y, the corrosion rates increased gradually to about 6.0 mm/y after about 40 hours and remained at that value during the three days of exposure. The increasing corrosion rate is thought to be due to the initial increase in surface roughness until reaching a steady state. The surface roughness can contribute to intensify corrosion processes due to the high local wall shear stress [82]. The LPR measurements indicate that there are no  $\text{FeCO}_3$  layers formed on the

steel surface, where is no decrease in corrosion after three days of exposure. After three days of exposure, the samples were removed and the weight loss corrosion rate was found to be 15 mm/y for X65I and 11 mm/y for X70, which were much higher than the value obtained from integration in time of the corrosion rate values from LPR data. This suggests that probably the B value used here was underestimated as shown, see Figure 98. Here again, the corrosion rate assumed was not purely under charge-transfer control, so the effect of mass transfer from cathodic limiting current could be the reason for the difference between weight loss and integrated LPR corrosion rates.

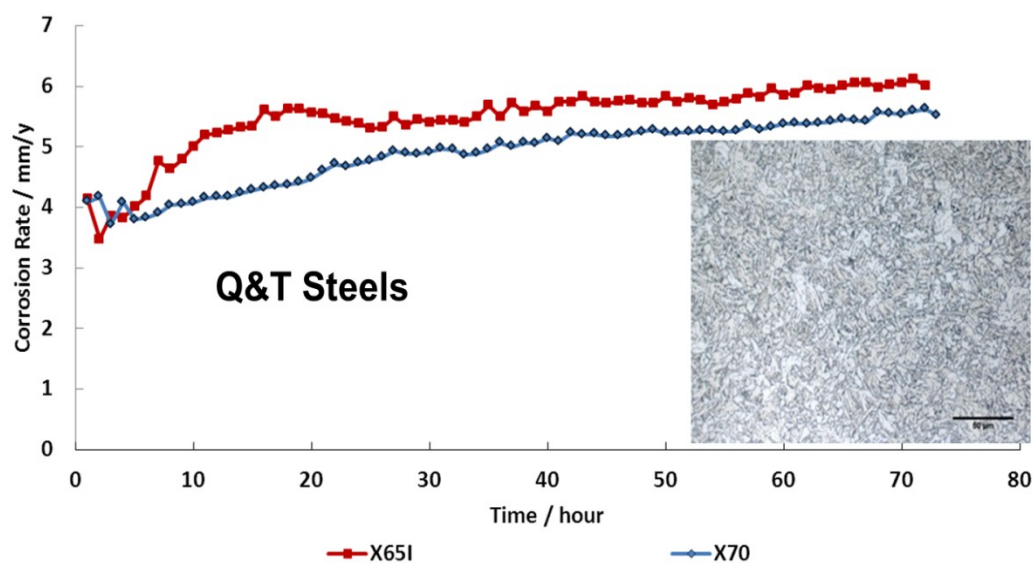
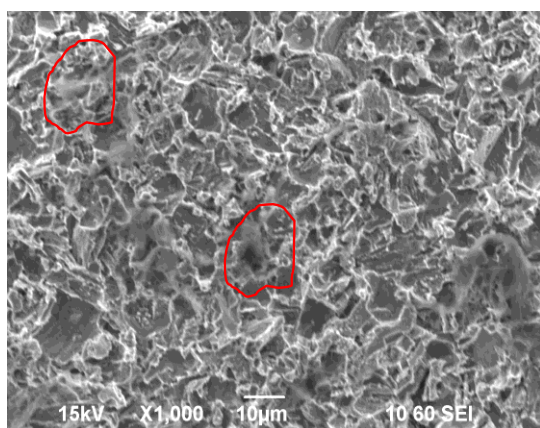


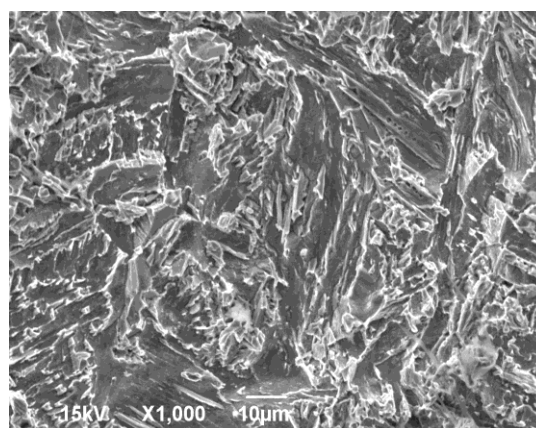
Figure 93: LPR measurements with time for Q&T steels. 3 days of exposure at 80°C, 1.5 bar CO<sub>2</sub>, pH 6.6, B=26 mV/decade,  $\tau = 535$  Pa.

However, the concentration of Fe<sup>2+</sup> was decreased over time as shown in Figure 92, the images that were taken by SEM upon removal of the samples from the system after three days of exposure show that there is no FeCO<sub>3</sub> layer, see Figure 94. The

decreasing in  $\text{Fe}^{2+}$  concentration could be due to the precipitation of  $\text{FeCO}_3$  elsewhere in the system (tank or piping). Because the carbon content of X65I steel is 0.15wt. %, there was some iron carbide remaining on the steel surface that were indicated by red circles as shown in Figure 94. On the other hand, there is no iron carbide found on X70 steel, which has very low carbon content (0.07 wt.% C), see Figure 94. The top surface analysis of steel by SEM and EDS also shows the main element is the iron substrate material indicating the surface is not covered by an  $\text{FeCO}_3$  layer, see Figure 95.

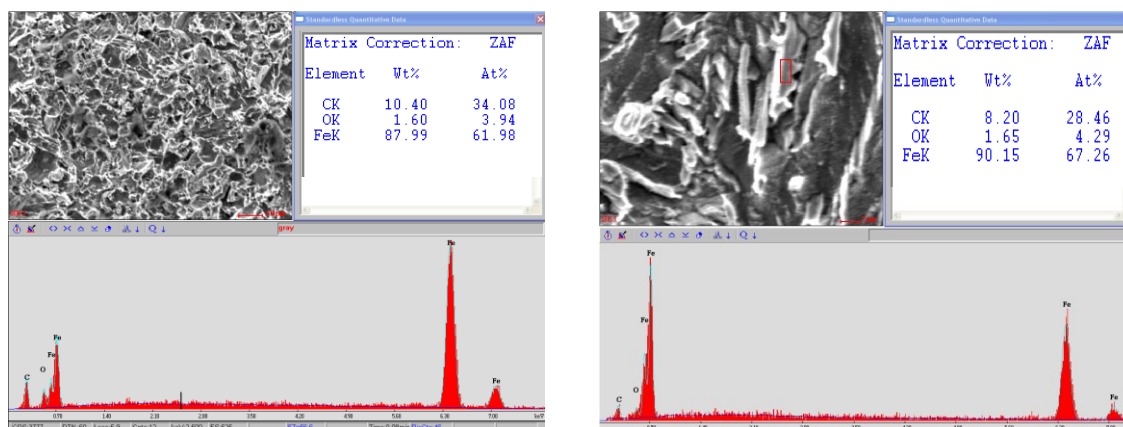


X65I, Iron carbides remained on the steel surface



X70, No iron carbides

Figure 94: SEM top surface analysis of Q&T steel samples (X65I, X70) after 3 days of exposure at 80°C, 1.5 bar  $\text{CO}_2$ , pH 6.6,  $\tau = 535$  Pa.



X65I.

X70.

Figure 95: SEM & EDS top surface analysis show that there is no  $\text{FeCO}_3$  layer formed on the steel surface after 3 days of exposure at  $80^\circ\text{C}$ , Q&T steels, 1.5 bar  $\text{CO}_2$ , pH 6.6,  $\tau = 535$  Pa.

The visual inspection of a sample after three days of exposure also indicates that  $\text{FeCO}_3$  layer has not formed on the steel. The IFM images and analysis show very small localized corrosion features on both steels, see Figure 96 and Figure 97. However, when making comparison between the general and pit penetration rates of both steels, the general corrosion rate is about five times higher than pit penetration rate, see Figure 98.

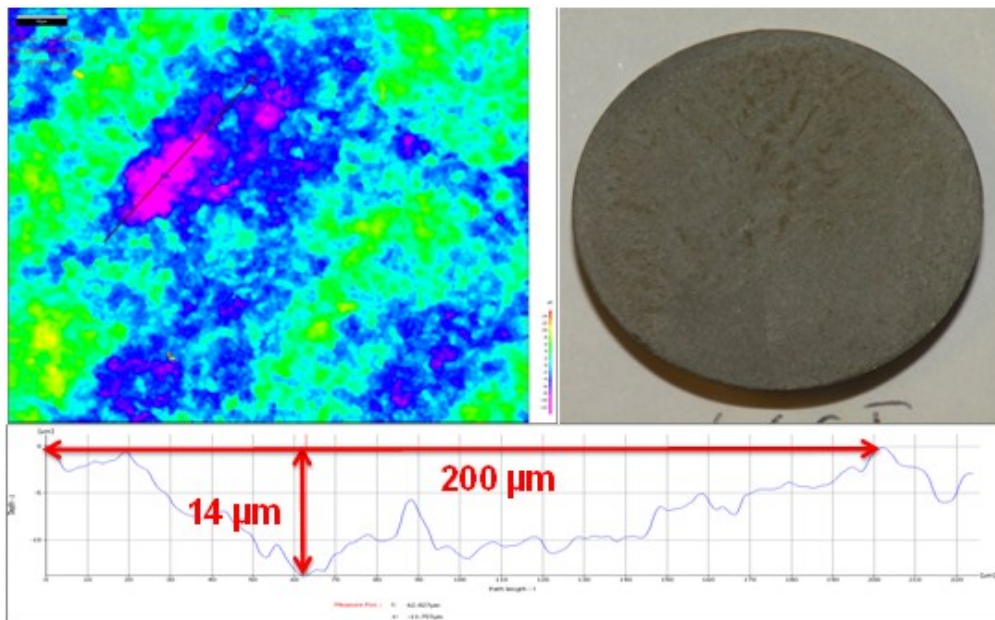


Figure 96: IFM top surface analysis shows wide shallow pits with 200  $\mu\text{m}$  in width & 14  $\mu\text{m}$  in depth. There is no  $\text{FeCO}_3$  layer formed on the steel surface after 3 days of exposure at 80°C, Q&T steel X65I, 1.5 bar  $\text{CO}_2$ , pH 6.6,  $\tau = 535$  Pa.

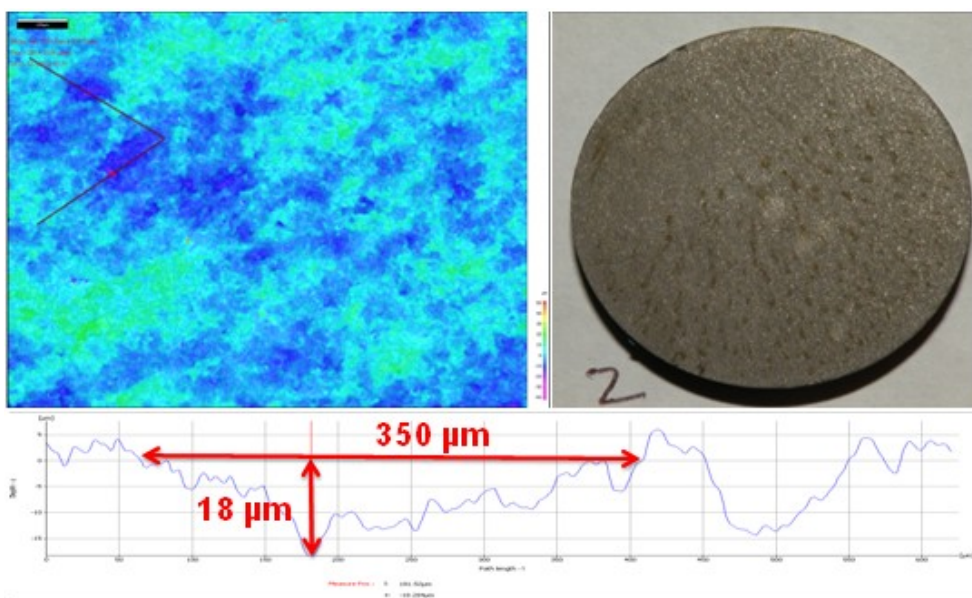


Figure 97: IFM top surface analysis shows wide shallow pits with 350  $\mu\text{m}$  in width & 18  $\mu\text{m}$  in depth. There is no  $\text{FeCO}_3$  layer formed on the steel surface after 3 days of exposure at 80°C, Q&T steel X70, 1.5 bar  $\text{CO}_2$ , pH 6.6,  $\tau = 535$  Pa.

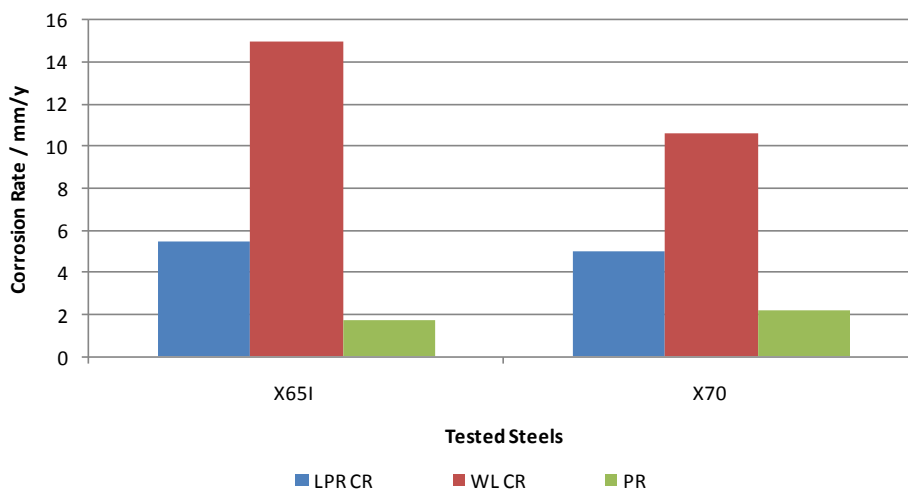


Figure 98: Comparison between corrosion rates measured by integrated LPR, weight loss (WL), and pit penetration rate (PR). After 3 days of exposure at 80°C, Q&T steels, 1.5 bar CO<sub>2</sub>, pH 6.6,  $\tau = 535$  Pa.

- X65II steel:

Variation of the LPR corrosion rate of X65II with exposure time is shown in Figure 99. At the beginning of the test, the corrosion rate was 5 mm/y, the corrosion rates increased gradually to about 7 mm/y after about 10 hours and remained at this value during the three days of exposure. Here again as mentioned before, the increase in corrosion rates is thought to be due to the initial increase in surface roughness until reaching a steady state. The LPR measurements indicate that there is no FeCO<sub>3</sub> that formed on the steel surface, and that there is no increase in corrosion rate after three days of exposure. After three days of exposure, the samples were removed and the weight loss corrosion rate was found to be 10 mm/y, as shown in Figure 103.

The images that were taken by SEM upon removal of the samples from the system after three days of exposure show that the sample surface was bare steel with no FeCO<sub>3</sub> layer, see Figure 100. The top surface analysis of steel by SEM and EDS also

shows composition consistent with the steel substrate material, indicating the surface is not covered by an  $\text{FeCO}_3$  layer; see Figure 101.

Although X65II steel suffered high localized or pitting corrosion when it was covered by a partially protective  $\text{FeCO}_3$  layer (described in Chapter 6), the high wall shear stress did not cause any localized corrosion in the present experiments. The IFM analysis of the sample after three days of exposure shows large areas with shallow pits, see Figure 102.

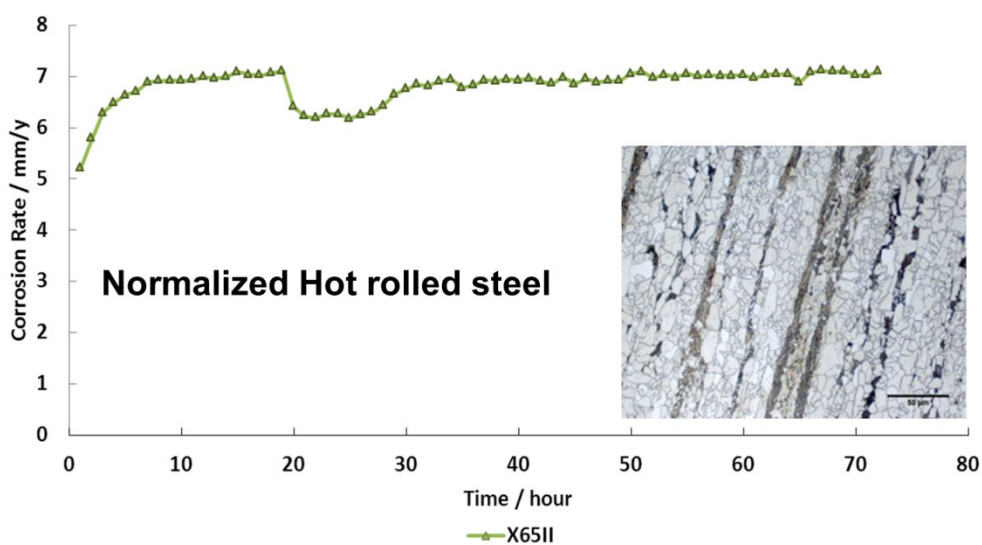


Figure 99: LPR measurements with time for Normalized hot rolled steel X65II, 3 days of exposure at  $80^\circ\text{C}$ , 1.5 bar  $\text{CO}_2$ , pH 6.6,  $B=26$  mV/decade,  $\tau = 535$  Pa.

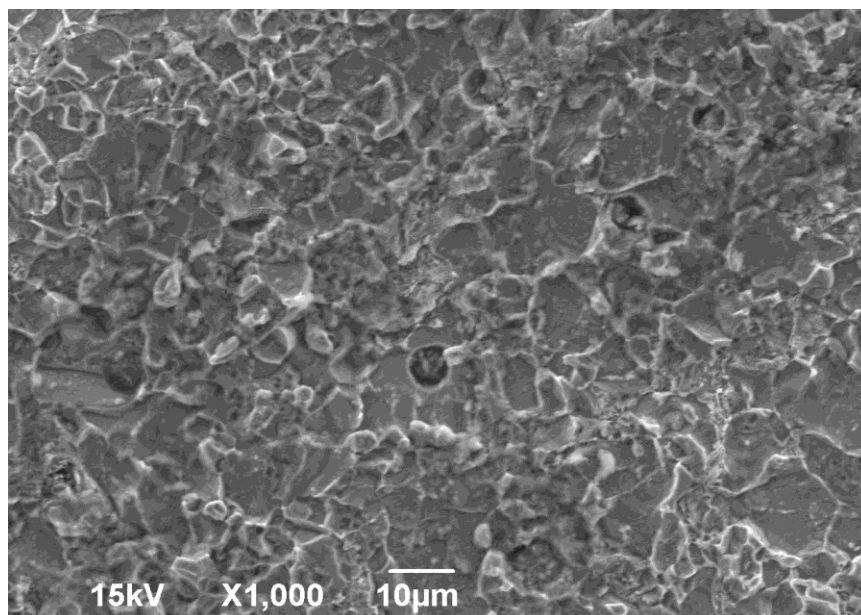


Figure 100: SEM top surface analysis of samples after 3 days of exposure at 80°C, NHR steel X65II, 1.5 bar CO<sub>2</sub>, pH 6.6,  $\tau = 535$  Pa, No iron carbides remained on the steel surface.

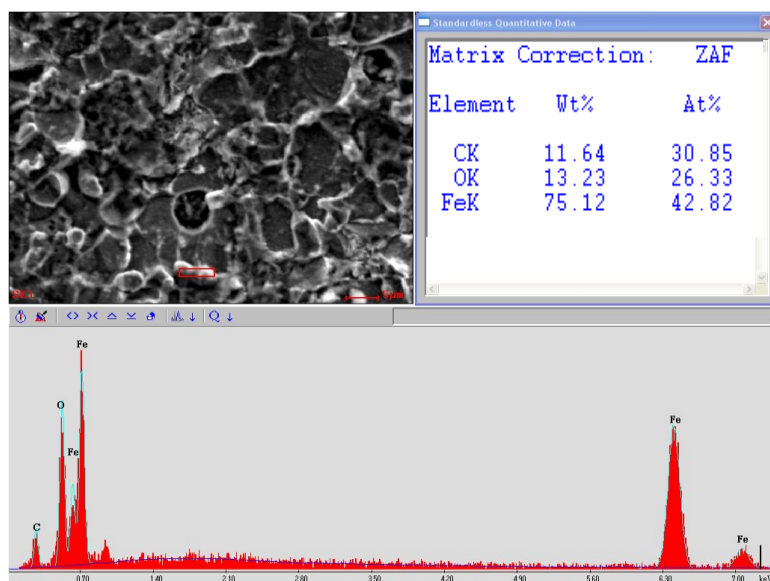


Figure 101: SEM & EDS top surface analysis show that there is no FeCO<sub>3</sub> layer formed on the steel surface after 3 days of exposure at 80°C, NHR steel X65II, 1.5 bar CO<sub>2</sub>, pH 6.6,  $\tau = 535$  Pa.

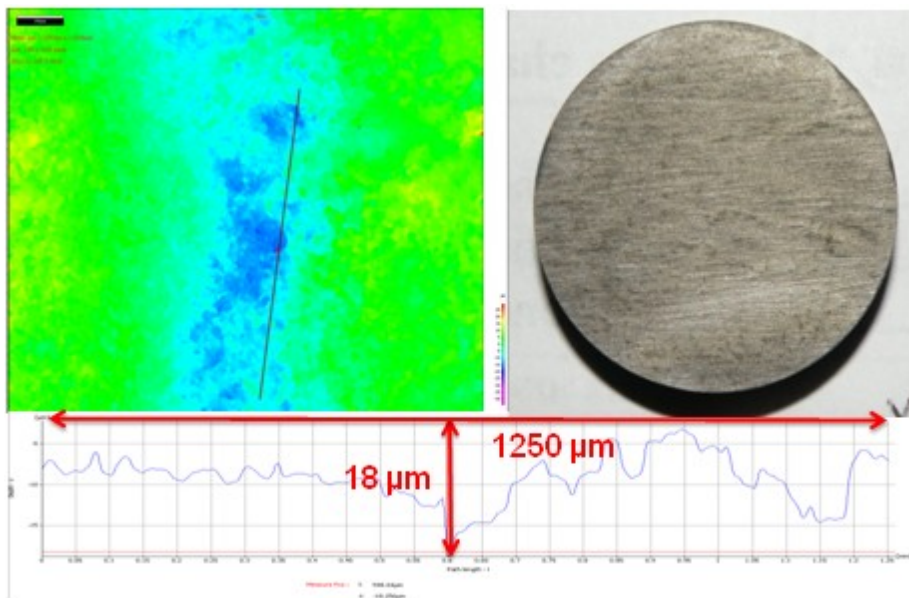


Figure 102: IFM top surface analysis shows large areas of shallow localized corrosion with 1250  $\mu\text{m}$  in width & 18  $\mu\text{m}$  in depth. No  $\text{FeCO}_3$  layer formed on the surface after 3 days of exposure at 80°C, NHR steel X65II, 1.5 bar  $\text{CO}_2$ , pH 6.6,  $\tau = 535$  Pa.

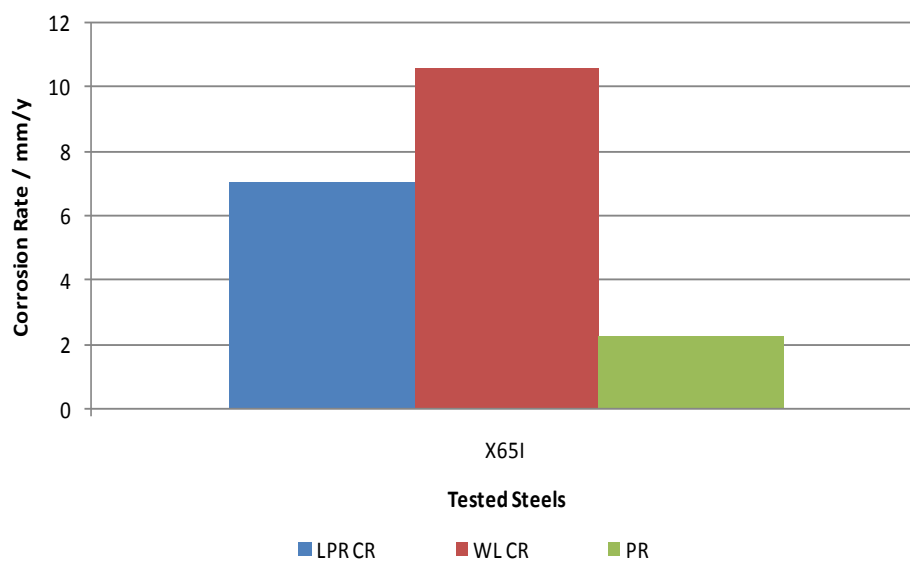


Figure 103: Comparison between corrosion rates measured by integrated LPR, weight loss (W/L), and pit penetration rate (PR). After 3 days of exposure at 80°C, NHR steel X65II, 1.5 bar  $\text{CO}_2$ , pH 6.6,  $\tau = 535$  Pa.

- X52 & A106GRB, Normalized steels:

Variation of the LPR corrosion rate of normalized steels with exposure time is shown in Figure 104. At the beginning of the test, the corrosion rate was 4-6 mm/y, the corrosion rates increased gradually to about 8.5 mm/y after about 30 hours and remained almost the same during the three days of exposure. Here again, the increase in corrosion rate is thought to be due to the initial increase in surface roughness until reaching a steady state. The increasing in corrosion rate after 30 hours where higher than what was observed in the other steels (X65, X70, and X65II) this can be related to the higher surface roughness due to the large grains of ferrite and pearlite. The LPR measurements indicate that there is no  $\text{FeCO}_3$  layers formed on steel surfaces. After three days of exposure, the samples were removed and the weight loss corrosion rate was found to be about 20 mm/y for both steels, which were much higher than the value obtained from integration in time of the corrosion rate values from LPR data, see Figure 109. This suggests that probably the B value used here was underestimated. Here again, as shown before, in the case of X65I and X70 steels, the corrosion rate assumed was not purely under charge-transfer control. In this case also, there is no indication that  $\text{FeCO}_3$  layer was precipitated on steel surfaces. The SEM and EDS analysis of the samples upon removal from the system after three days of exposure indicate that there is no  $\text{FeCO}_3$  layer formed on the samples, see Figure 105 and Figure 106. Because the carbon content of X52 and A106GRB is high (about 0.26 wt.% C), iron carbides remained on the steel surface that were indicted by red circles as shown in Figure 105.

As shown in Figure 107 and Figure 108, the visual inspection of a sample after three days of exposure also indicates that no  $\text{FeCO}_3$  layer was formed on the steel. The IFM images and analysis show large areas of local areas of material loss occurred and the dimensions of these local areas of material loss match the grain size of pearlite. As shown in Figure 108, A106GRB steel suffered from very large areas of shallow localized corrosion with about  $53 \mu\text{m}$  in depth, this again matches the grain size of pearlite ( $\sim 50 \mu\text{m}$  in diameter), see Figure 18 in chapter 4. However, when making comparison between the general and localized corrosion rates of both steel, the general corrosion rate is three times higher than localized corrosion, which indicates that the steel did not suffer from localized corrosion, see Figure 109.

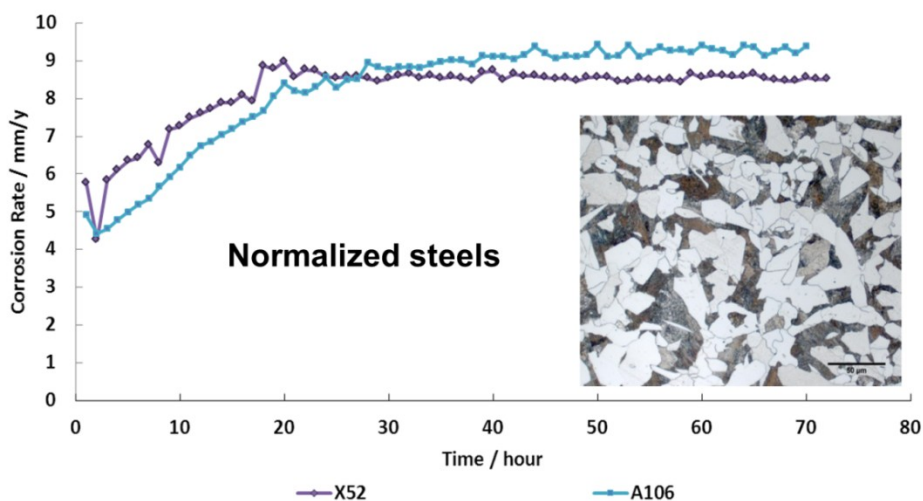
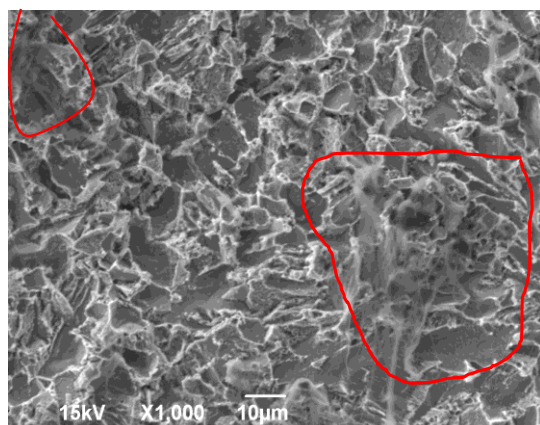
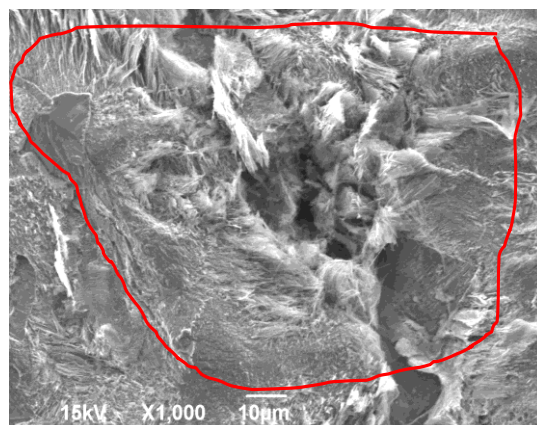


Figure 104: LPR measurements with time for Normalized steels.  
3 days of exposure at  $80^\circ\text{C}$ , 1.5 bar  $\text{CO}_2$ , pH 6.6,  $B=26 \text{ mV/decade}$ ,  $\tau = 535 \text{ Pa}$ .

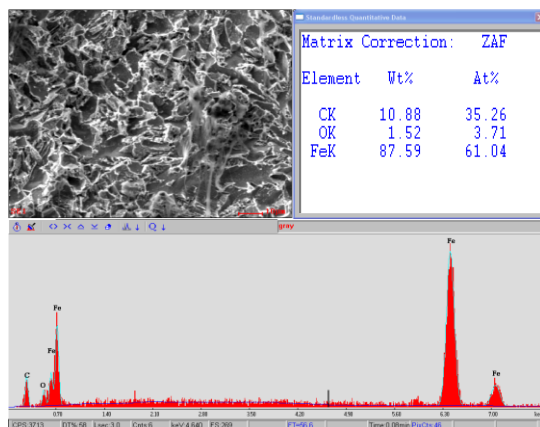


X52, iron carbides remained on the surface

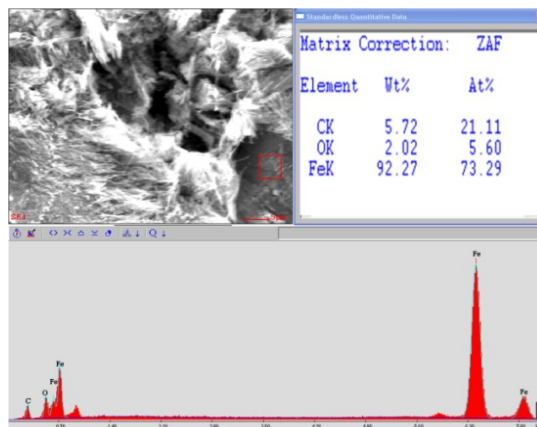


A106GRB, iron carbides remained on the surface

Figure 105: SEM top surface analysis of samples after 3 days of exposure at 80°C, Normalized steels, 1.5 bar CO<sub>2</sub>, pH 6.6,  $\tau = 535$  Pa.



X52.



A106GRB.

Figure 106: SEM & EDS top surface analysis show that there is no FeCO<sub>3</sub> layer formed on the steel surface after 3 days of exposure at 80°C, Normalized steels, 1.5 bar CO<sub>2</sub>, pH 6.6,  $\tau = 535$  Pa.

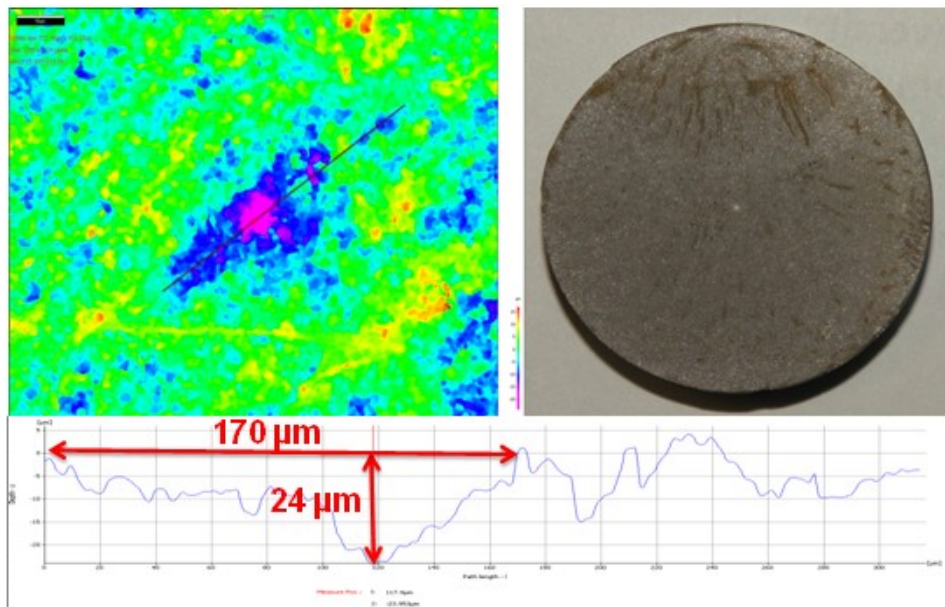


Figure 107: IFM top surface analysis show that there is no  $\text{FeCO}_3$  layer formed on the steel surface after 3 days of exposure at  $80^\circ\text{C}$ , Normalized steel X52, 1.5 bar  $\text{CO}_2$ , pH 6.6,  $\tau = 535$  Pa.

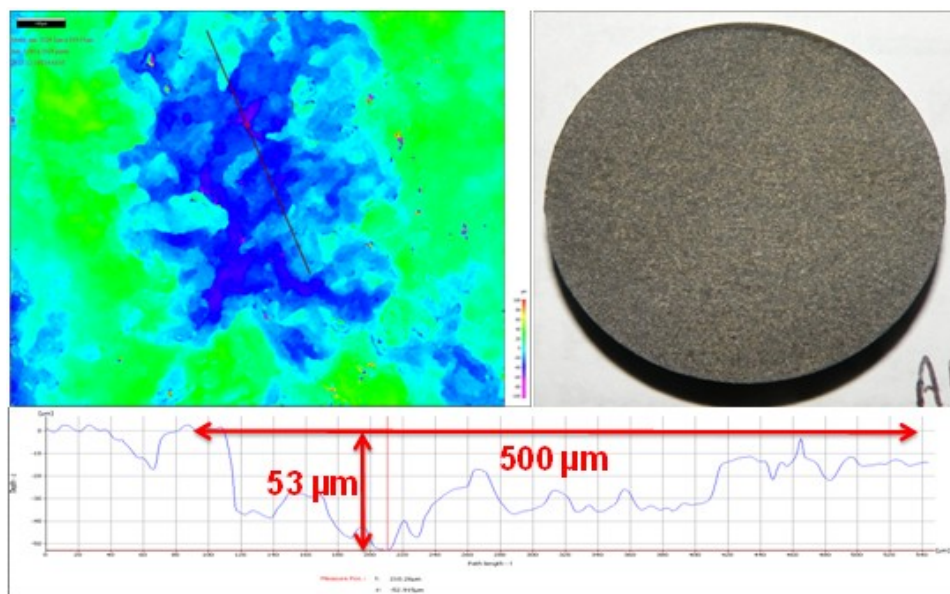


Figure 108: IFM top surface analysis show that there is no  $\text{FeCO}_3$  layer formed on the steel surface after 3 days of exposure at  $80^\circ\text{C}$ , Normalized steel A106, 1.5 bar  $\text{CO}_2$ , pH 6.6,  $\tau = 535$  Pa.

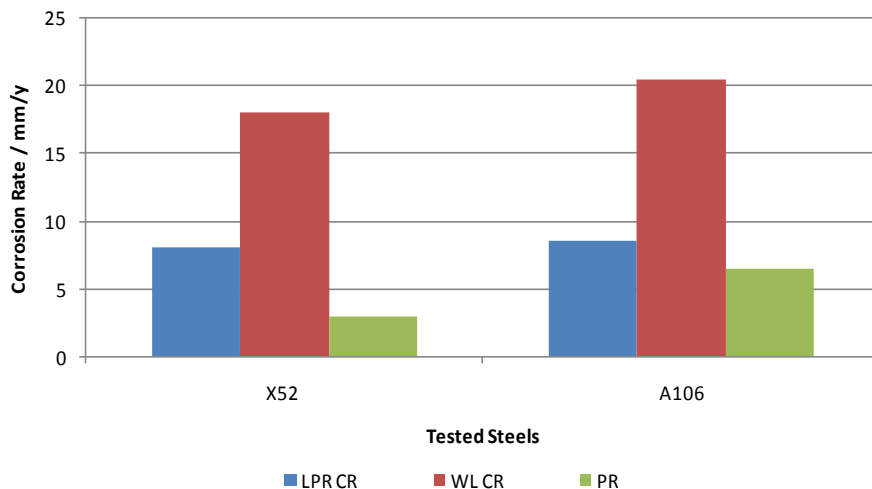


Figure 109: Comparison between corrosion rates measured by integrated LPR, weight loss (W/L), and pit penetration rate (PR). After 3 days of exposure at 80°C, Normalized steels, 1.5 bar CO<sub>2</sub>, pH 6.6, B=26 mV/decade,  $\tau = 535$  Pa.

#### 7.4 Summary

For all steels tested here, no protective FeCO<sub>3</sub> layers formed at high wall shear stress even at high bulk supersaturation condition of CO<sub>2</sub>. Due to intense turbulence, the rapid diffusion of species from and toward the steel surface made it more difficult to form an FeCO<sub>3</sub> layer. The ferrous ions generated by corrosion were effectively removed and a more rapid diffusion of hydrogen ions to the surface lead to a lower surface pH what made it difficult to precipitate FeCO<sub>3</sub>. Additionally, the high wall shear stress led to removal of any Fe<sub>3</sub>C which would normally left behind on carbon steel and provide a matrix where FeCO<sub>3</sub> would more readily precipitate.

For all cases the bare steel corrosion rates were high. However, the general corrosion rates of Q&T steels was lower than for normalized steels; see Figure 110 and Figure 111. The higher general corrosion rates of normalized steels (X52, A106GRB) can be related to the amount of iron carbides and grain size of pearlite. When normalized

steel with large carbide particles is exposed to a corrosive environment with high flow rates, the ferrite that surrounds the carbide particles would rapidly corrode due to a galvanic effect between ferrite (anode) and iron carbide (cathode). Remaining iron carbides are removed by the local high wall shear stress. On the other hand, when Q&T steel, which has single face structure (tempered martensite) is exposed to corrosive environment with high flow rates, the effect of galvanic corrosion will be insignificant. Normalized steel as well, which has small amounts of carbide particles, such as X65II, when is exposed to corrosive environment with high flow rates, the effect of galvanic corrosion will be insignificant. Figure 110 and Figure 111, show that there is relationship between the carbon content, grain size, and the corrosion rate.

Although some steels suffered localized or pitting corrosion when they were covered by  $\text{FeCO}_3$  layer (described in Part I), the high wall shear stress did not cause any localized corrosion when no  $\text{FeCO}_3$  layer could be formed, see Figure 111.

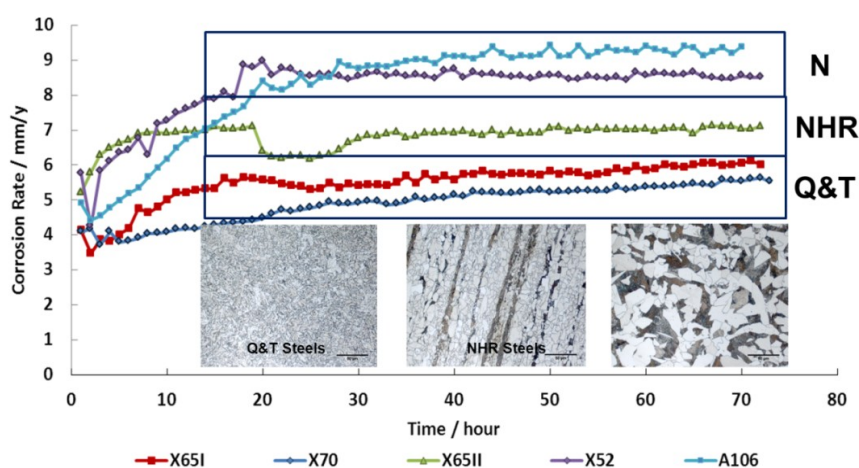


Figure 110: LPR measurements of corrosion rate (CR) in mm/y. 3 days of exposure at  $80^{\circ}\text{C}$ , 1.5 bar  $\text{CO}_2$ , pH 6.6,  $B=26$  mV/decade,  $\tau = 535$  Pa, Quenched and Tempered (Q&T), Normalized steels (N), Normalized hot rolled steels (NHR).

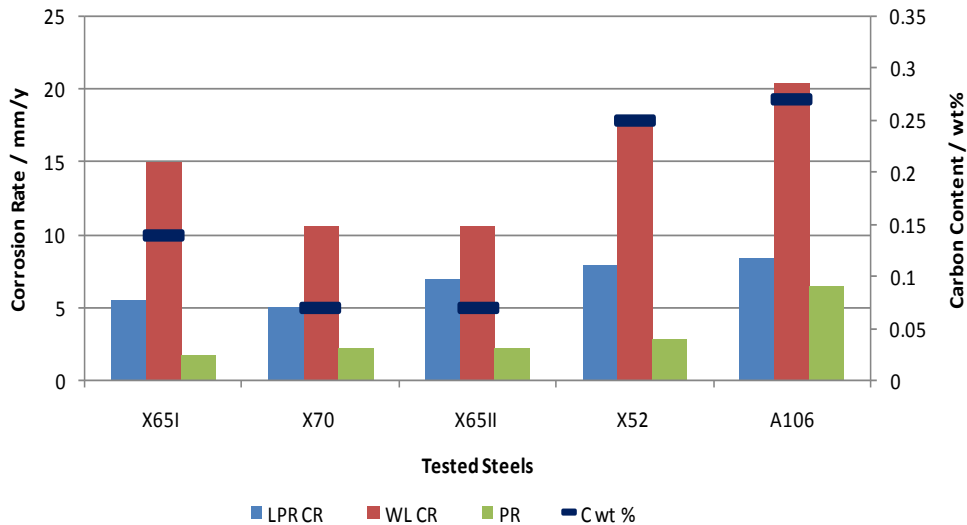


Figure 111: Comparison between corrosion rates measured by weight loss (W/L), integrated LPR, pit penetration rate (PR) and carbon content (wt. %). 3 days of exposure at 80°C, 1.5 bar CO<sub>2</sub>, pH 6.6,  $\tau = 535$  Pa.

## 7.5 Discussion

From the obtained results, the effect of high wall shear stress, chemical composition and microstructure on the formation, adhesion and protectiveness of FeCO<sub>3</sub> layer, can be classified into two mechanisms according to steel type:

- 1- Effect of wall high shear stress on normalized steel.
- 2- Effect of high wall shear stress on Q&T steel.

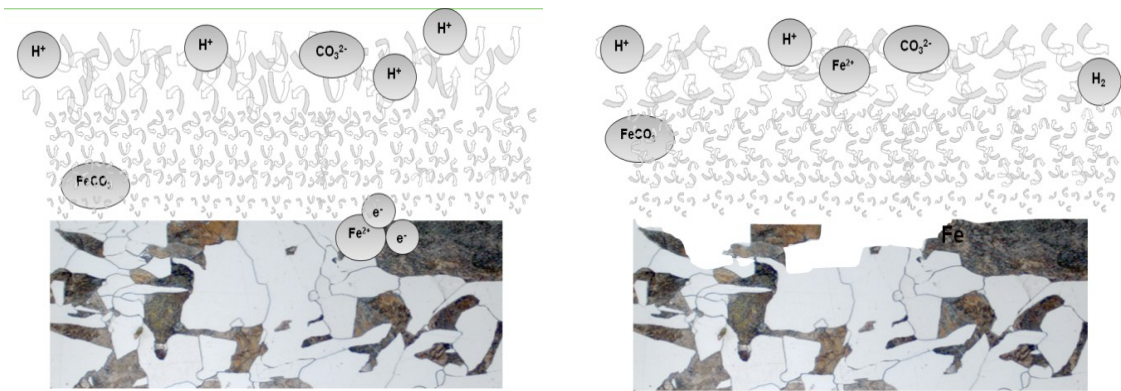
For both mechanisms, when steels are exposed to high flow rates in a solution with a high FeCO<sub>3</sub> supersaturation the fast movement of species transport from and towards the steel surface will increase the rate at which hydrogen ions are replenished and generated ferrous ions are removed from the surface, which in turn prevents the precipitation of FeCO<sub>3</sub> at the steel surface and increases the corrosion rate, Figure 112-a, Figure 113-a.

- Mechanism I: Effect of wall high shear stress on normalized steel.

In this case, the ferrite that surrounds the carbide particles will rapidly corrode due to a galvanic effect between ferrite (anode) and iron carbide (cathode); see Figure 112-b. Residual iron carbides are then removed mechanically by the local high wall shear stress from the steel surface, with additional particle detachment from the surface, Figure 112-c, Figure 112-d. As shown in one study [30] the iron carbides that remained on steel surface can enhance the formation of an  $\text{FeCO}_3$  layer by creating favorable environmental conditions for  $\text{FeCO}_3$  precipitation. High wall shear stress removes the exposed iron carbides and therefore does not provide a location for changes in the environmental conditions needed to precipitate iron carbonate. Preventing the formation of iron carbonate lead to increase the mass transfer and increase the corrosion rate.

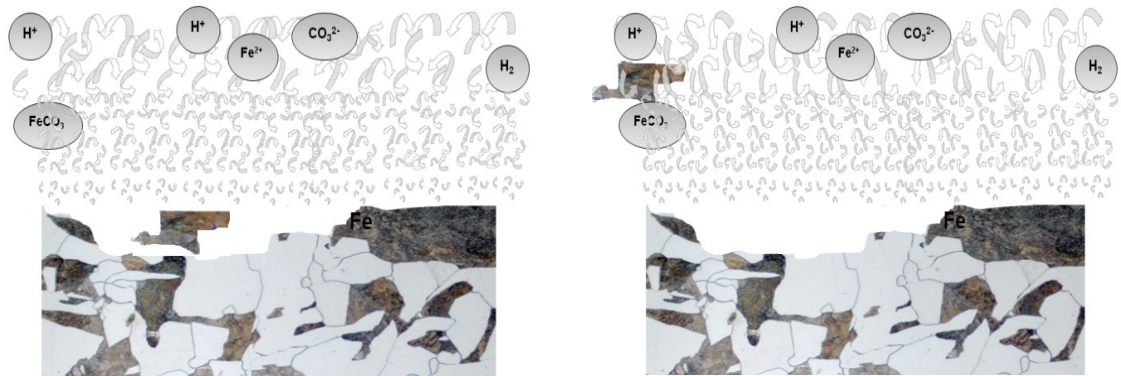
- Mechanism II: Effect of high wall shear stress on Q&T steel.

In this case, because the microstructure of steel consists of tempered martensite which is considered as single face structure, there is not a significant galvanic effect. That is why the corrosion rate of Q&T steel is lower than normalized steel, Figure 113-b.



a- Fast movement of flow transports species from and towards the steel surface.

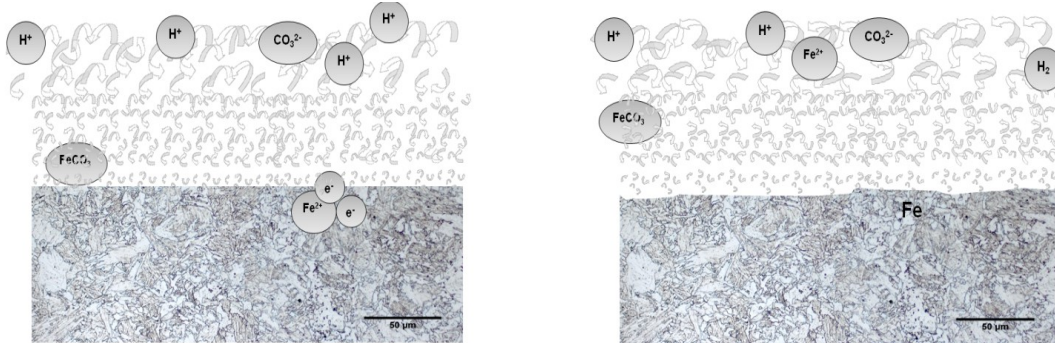
b- Ferrite will corrode very fast.



c- Ferrite that surrounds the iron carbide particles will corrode very fast, weak iron carbide is left behind.

d- Force of fluid flow removes weak iron carbide structure by the local high wall shear stress from the steel surface.

Figure 112. Effect of high wall shear stress on normalized steel.



a- Fast movement of flow transports species from and towards the steel surface.

b- Single face structure, there is not a significant galvanic effect. Surface will corrode with the same rate

Figure 113: Effect of high wall shear stress on Q&T and low carbon steels.

## CHAPTER 8: CONCLUSIONS AND FUTURE WORK

### 8.1 Conclusions

1. There was no systematic and significant difference between results obtained from experiments conducted in the glass cell and TCFC at similar low mass transfer rates.

This validated that the TCFC can be used instead of the glass cell to study localized corrosion at high flow rates.

2. Although the microstructures of steels were different, no significant differences in general corrosion of all steels at pH 4.0, with changing temperature and velocity, were observed. Because no corrosion product layer was formed at pH 4.0, there was no significant effect of alloying elements and microstructure on the corrosion rate in a non-film forming environment.

3. At supersaturated conditions,  $\text{FeCO}_3$  corrosion product layer formed on all steels. However, increasing the wall shear stress caused some locations in the  $\text{FeCO}_3$  layer to fail which led to pitting.

- The breakdown of an  $\text{FeCO}_3$  layer is thought to be caused by fluctuation of forces due to pressure changes and high local shear stress related to the turbulent flow.
- The penetration rates of pitting in normalized steels (X52 & A106GRB) were much lower than for Q & T steels (X65I & X70). The low pit penetration rates in normalized steels can be related to the homogeneity of microstructure and the pearlite structures which help the  $\text{FeCO}_3$  layer “stick” to the steel surface.

- The hot rolled steel X65II had the largest pitting penetration rates. However, the pitting initiated even before increasing wall shear stress, which was related to inclusions and phase distribution of the ferrite/pearlite structure.
4.  $\text{FeCO}_3$  layers cannot be formed at high wall shear stress ( $\tau=535\text{Pa}$ ), even with supersaturated conditions. This can be related to the fast movement of species from and toward the steel surface and the high local shear stress that contribute to removal of generated ferrous ions, preventing the formation of  $\text{FeCO}_3$  as a corrosion product layer.
- At high wall shear stress, the general corrosion rates of normalized steels (X52, A106GRB) are higher than for Q&T steels. This can be related to the amount of iron carbides, or carbon content, in the steel.
  - Because all steels suffered from high general corrosion, no localized corrosion behavior was observed since the penetration rates of observed pitting are much lower than general corrosion ( $\text{PR}=2$  to  $7$  mm/y).

## 8.2 Future Work

1. Since the effect of highly turbulent flow on formed  $\text{FeCO}_3$  layers is considered to be time dependent, this effect should be studied at longer exposure times. This would facilitate determination of how the exposure time for high shear stress conditions can affect the formed  $\text{FeCO}_3$  layer.
2. Since the  $\text{FeCO}_3$  that formed without initial addition of  $\text{Fe}^{2+}$  is denser than the corrosion product formed with initial addition of  $\text{Fe}^{2+}$ , it should be further studied how experimental methods can affect the protectiveness of formed  $\text{FeCO}_3$ .

3. Conduct normalizing heat treatment on low carbon Q&T steels (X65I & X70) to study how their recrystallization and grain growth affects their corrosion behavior for high flow rates; such steels would have altered microstructure for the same chemical composition. Corrosion data could then be compared with that obtained for higher carbon normalized steels (X52, A106GRB). The goal would be to further relate how microstructure and carbide content, or only carbide content or microstructure, affects corrosion behavior.

4. Study the formation of  $\text{FeCO}_3$  corrosion layers at wall shear stresses between 35 and 535 Pa to determine the maximum wall shear stress that permits the development of a protective  $\text{FeCO}_3$  layer for different steel microstructures.

## REFERENCES

- [1] M. Thomas and P. Hebert, "CO<sub>2</sub> corrosion in gas production wells correlation of predictions and field experience," Corrosion/1995, Houston, TX: NACE International, Paper. 121.
- [2] J. Crolet and M. Bonis, "Prediction of the risks of CO<sub>2</sub> corrosion in oil and gas wells," SPE Prod Eng, Vol. 6, no 4, pp. 449-453, 1991.
- [3] M. Kermani and L. Smith, "CO<sub>2</sub> corrosion control in the oil and gas production design considerations," European Federation of Corrosion, Vol. 23, 1997.
- [4] L. Newton, "Sacroc CO<sub>2</sub> project-corrosion problems and solutions, advances in CO<sub>2</sub> corrosion," Corrosion/1984, Houston, TX: NACE International, Paper. 67.
- [5] D. Lopez, T. Perez, and S. Simison, "The Influence of Microstructure and Chemical Composition of Carbon and Low Alloy Steels in CO<sub>2</sub> Corrosion. A State-of-the-art Appraisal," Elsevier Ltd, Material and Design, Vol. 24, pp. 561-575, 2003.
- [6] S. Nestic and L. Lunde, "Carbon dioxide corrosion of carbon steel in two-phase flow," Corrosion, Vol.50, no 9, pp 717-727, 1994.
- [7] S. Nestic and W. Sun, Shreir's Corrosion: Corrosion in acid gas solutions, Fourth Edition, Vol. 2. Amsterdam: Elsevier, 2010, pp. 1270-1298.
- [8] M. Nordsveen, S. Nestic, R. Nyborg, and A. Stangeland, "A mechanistic model for carbon dioxide corrosion of mild steel in the presence of protective iron carbonate films – part 1: Theory and verification," Corrosion, Vol. 59, no 5, pp. 443 – 456, 2003.
- [9] E. Dayalan, "CO<sub>2</sub> corrosion prediction in pipe flow under FeCO<sub>3</sub> scale-forming conditions," Corrosion/1998, Houston, TX: NACE, Paper. 51.

- [10] J. Crolet, N. Thevenot, and S. Netic, "The role of conductive corrosion products in the protectiveness of corrosion layers," *Corrosion*, Vol. 54, no 3, pp.194 –203, 1998.
- [11] R. John, "Sweet Corrosion: an information system for the analysis of corrosion of steels by water and carbon dioxide," *Corrosion/1998*, Houston, TX, NACE, Paper. 20.
- [12] Y. Gunaltum, "Combining research and field data for corrosion rate prediction," *Corrosion/1996*, Houston, TX, NACE, Paper. 27.
- [13] C. de Waard and U. Lotz, "Prediction of CO<sub>2</sub> corrosion of carbon steel," *Corrosion/1993*, Houston, TX, NACE, Paper. 69.
- [14] C. de Waard and D. Milliams, "Carbonic acid corrosion of steel," *Corrosion*, Vol.31, no 5, pp 177-181, 1975.
- [15] V. Ruzic, M. Veidt, and S. Netic, "Protective FeCO<sub>3</sub> layers - Part 1: Mechanical removal in single-phase aqueous flow," *Corrosion*, Vol.62, no 5, pp 419-432, 2006.
- [16] S. Netic, M. Nordsveen, R. Nyborg, and A. Stangeland, "A mechanistic model for carbon dioxide corrosion of mild steel in the presence of protective iron carbonate films – part 2:Numerical experiment," *Corrosion*, vol. 59, no 6, pp. 489 –497, 2003.
- [17] S. Netic, N. Thevenot, J. Crolet, and D. Drazic, "Electrochemical properties of iron dissolution in the presence of CO<sub>2</sub> – basics revisited" *Corrosion/1996*, Houston, TX, NACE, Paper. 3.
- [18] B. Pots, "Mechanistic models for the prediction of CO<sub>2</sub> corrosion rates under multi-phase flow conditions," *Corrosion/1995*, Houston, TX, NACE, Paper. 137.

- [19] P. Gartland and J. Salomonsen, "Pipeline integrity management strategy based on multiphase fluid flow and corrosion modeling," Corrosion/1999, Houston, TX, NACE Paper. 622.
- [20] A. Dugstad, "Mechanism of Protective film formation during CO<sub>2</sub> Corrosion of Carbon Steel," Corrosion/1998, Houston, TX, NACE, Paper. 31.
- [21] J. Crolet, N. Thevenot, and S. Netic, "The role of conductive corrosion products in the protectiveness of corrosion layers," Corrosion, Vol. 54, no 3, pp.194 –203, 1998.
- [22] A. Dugstad, H. Hemmer, and M. Seiersten, "Effect of Steel Microstructure upon Corrosion Rate and Protective Iron Carbonates Film Formation," Corrosion/2000, Houston, TX, NACE, Paper. 24.
- [23] M. Ueda and H. Takabe, "Effect of environmental factor and microstructure on morphology of corrosion products in CO<sub>2</sub> environments," Corrosion/1999, Houston, TX, NACE Paper. 13.
- [24] D. Clover, B. Kinsella, B. Pejic, and R. De Marco, "The influence of microstructure on the corrosion rate of various carbon steels ," Applied Electrochemistry, Vol. 35, no 2, pp. 139-149, 2005.
- [25] K. Videm, "The influence of composition of carbon steels on anodic and cathodic reaction rate in CO<sub>2</sub> corrosion," Corrosion/1998, Houston, TX, NACE, Paper. 30.
- [26] D. Lopez, W. Schreiner, S. de Sanchez, and S. Simison, "The influence of carbon steel microstructure on corrosion layers. An XPS and SEM characterization," Appl Surf Sci, Vol. 207, pp, 69-85, 2003.
- [27] S. Al-Hassan, B. Mishra, D. Olson, and M. Salama, "Effect of microstructure on corrosion of steels in aqueous solution containing carbon dioxide," Corrosion, Vol 54, no. 6, pp. 480-491, 1998.

- [28] S. Wang, C. Shen, K. Long, T. Zhang, F. Wang, and Z. Zhang, "The Electrochemical Corrosion Behavior of Bulk Nanocrystalline Ingot Iron in HCl Acid Solution," *J. Phys. Chem. B*, Vol.109, American Chemical Society. 2005.
- [29] M. Salcu, "Increasing the Lifetime of J55 Tubing by Improving Steel Metallurgy Laboratory and Field Tests Achievements," *Corrosion/2013*, Houston, TX, NACE, Paper. 2141.
- [30] F. Farelas, B. Brown, and S. Nestic, "Iron Carbide & Its Influence on Formation of Protective Iron Carbonate in CO<sub>2</sub> Corrosion of Mild Steel," *Corrosion/2013*, Houston, TX, NACE, Paper. 2291.
- [31] E. Gulbrandsen, R. Nyborg, T. Loland, and K. Nisancioglu, "Effect of steel microstructure and composition on inhibition of CO<sub>2</sub> corrosion," *Corrosion/2000*, Houston, TX, NACE, Paper. 23.
- [32] D. Lopez, S. Simison, and S. de Sanchez, "The influence of steel microstructure on CO<sub>2</sub> corrosion. EIS studies on the inhibition efficiency of benzimidazole," *Electrochim Acta*, Vol 48, no. 7, pp. 845-854, 2003.
- [33] R. Nybborg and A. Dugstad, "Mesa corrosion attack in carbon steel and 0.5% chromium steel," *Corrosion/1998*, Houston, TX, NACE, Paper. 29.
- [34] A. Halvorsnand and T. Sontvedt, "CO<sub>2</sub> corrosion model for carbon steel including a wall shear stress model for multiphase flow and limits for production rate to avoid mesa attack," *Corrosion/1999*, Houston, TX: NACE International, Paper. 42.
- [35] J. Han, Y. Yang, B. Brown, and S. Nestic, "Roles of passivation and galvanic effects in localized CO<sub>2</sub> corrosion of mild steel", *Corrosion/08*, Houston, TX, NACE, paper no. 08332.
- [36] G. Schmitt and S. Feinen, "Media effects in CO<sub>2</sub> pitting corrosion of steel", *Ukrainian Corrosion Congress/1998*, Lviv, Ukraine, paper.13.

- [37] G. Schmitt, M. Mueller, M. Papenfuss, and E. Strobel-Effertz, "Understanding localized CO<sub>2</sub> corrosion of carbon steel from physical properties of iron carbonate scales", Corrosion/1999, Houston, TX, NACE, Paper. 38.
- [38] C. de Waard, U. Lotz, and A. Dugstad, "Influence of liquid flow velocity on CO<sub>2</sub> corrosion. A semi-empirical model," Corrosion/1995, Houston, TX: NACE International, Paper. 128.
- [39] G. Schmitt and T. Gudde, "Local mass transport coefficients and local wall shear stresses at flow disturbances," Corrosion/1995, Houston, TX, NACE, Paper. 102.
- [40] G. Schmitt, T. Simon, and R. Hausler, "CO<sub>2</sub> Erosion corrosion and its inhibition under extreme shear stresses. II. Performance of inhibitors," Corrosion/1993, Houston, TX, NACE, Paper. 86.
- [41] G. Schmitt, "Fracture mechanical properties of CO<sub>2</sub> corrosion product scales and their relation to localized corrosion," Corrosion/1996, Houston, TX, NACE, Paper. 9.
- [42] F. Farelas, "Observation of high flow effects in CO<sub>2</sub> Corrosion," Corrosion Center JIP, Advisory Board Meeting, Apr 2008, OHIO University, Athens, Ohio.
- [43] J. Mora-Mendoza and S. Turgoose, "Fe<sub>3</sub>C influence on the corrosion rate of mild steel in aqueous CO<sub>2</sub> systems under turbulent flow conditions," Corrosion Sci, Vol. 44, pp. 1223–1246, 2002.
- [44] F. Al-Mutahar, G. Al-Aithan, K. Roberts, S. Shirazi, E. Rybicki<sup>1</sup>, and J. Shadley, "Characterization of Erosion Resistance of Iron Carbonate (FeCO<sub>3</sub>) Scale," Corrosion/2013, Houston, TX, NACE, Paper. 2713.
- [45] G. Schmitt and M. Mueller, "Critical wall shear stresses in CO<sub>2</sub> corrosion of carbon steel," Corrosion/1999, Houston, TX, NACE, Paper. 44.

- [46] Y. Yang, B. Brown, and S. Netic, "Mechanical strength and removal of a protective iron carbonate layer formed on mild steel in CO<sub>2</sub> corrosion," Corrosion/2010, Houston, TX, NACE, Paper. 383.
- [47] K. Gao, F. Yu, X. Pang, and G. Zhang, "Mechanical properties of CO<sub>2</sub> corrosion product scales and their relationship to corrosion rates," Corrosion Science, Vol. 50, no 10, pp 2796-2803, 2008.
- [48] J. Wang and A. Atrens, "Microstructure and grain boundary microanalysis of X70 pipeline steel," Journal of Material Science, Vol. 38, pp. 323 – 1330, 2003.
- [49] J. Wang, A. Atrens, D. Cousens, and N. Kinaev, "Microstructure of X52 and X65 pipeline steels," Journal of Material Science, Vol. 34, pp. 1721 – 1728, 1999.
- [50] J. Wang, A. Atrens, D. Cousens, C. Nockolds, and S. Bulcock, "Boundary characterization of X65 pipeline steel," Journal of Material Science, Vol. 34, pp. 1711 – 1719, 1999.
- [51] F. Xiao, B. Liao, D. Ren, Y. Shan, and K. Yang, "Acicular ferritic microstructure of a low-carbon Mn–Mo–Nb microalloyed pipeline steel," Materials Characterization, Vol. 54, no.4, pp. 305–314, 2005.
- [52] M. Zhao, F. Xiao, Y. Shan, "Microstructural characteristic and toughness of an ultra-low carbon acicular ferrite pipeline steel," Acta Metall. Sin., Vol. 38, pp. 283, 2002.
- [53] C. Shang, L. Hu, and S. Yang, "Forming and controlling of the acicular ferrite in low carbon micro-alloyed steel," Acta Metall. Sin., Vol. 14, no. 5, pp. 471, 2005.
- [54] S. Thompos, D. Colvin, and G. Krauss, "Continuous cooling transformations and microstructures in a low carbon, high-strength low-alloy plate steel," Metall. Trans. A, Vol. 21, p.1493, 1990.

- [55] P. Nice and M. Ueda, "Effect of microstructure and chromium alloying content to the corrosion resistance of low-alloy steel well tubing in seawater injection service," Corrosion/1998, Houston, TX, NACE, Paper. 3.
- [56] U. Lotz and T. Sydberger, "CO<sub>2</sub> corrosion of carbon steel and 13 Cr steel in particle-laden fluid," Corrosion, Vol. 44, no. 11, pp. 800–809, 1998.
- [57] M. Ueda and A. Ikeda, "The effect of microstructure and Cr content in steel on CO<sub>2</sub> corrosion," Corrosion/1996, Houston, TX: NACE International, Paper. 13.
- [58] T. Berntsen, M. Seiersten, and T. Hemmingsen, "Effect of FeCO<sub>3</sub> supersaturation and iron carbide exposure on the CO<sub>2</sub> corrosion rate of carbon steel," Corrosion/2011, Houston, TX, NACE, Paper. 11072.
- [59] D. Askeland, P. Fulay, and W. Wright, The Science and Engineering of Materials, Sixth Edition, Cengage Learning. Stamford, CT. 2006, pp. 493-531.
- [60] Micrograph Library, University of Cambridge. Available: <http://www.doitpoms.ac.uk/miclib/pds.swf?targetFrame=Fe-C-X>, [May. 30, 2013]
- [61] 2000 MATTER, The University of Liverpool, [http://www.matter.org.uk/steelmatter/metallurgy/7\\_1\\_2.html](http://www.matter.org.uk/steelmatter/metallurgy/7_1_2.html), [May. 30, 2013]
- [62] Laboratory Testing Inc. 2331 Topaz Drive, Hatfield, PA 19440, [May. 30, 2013]
- [63] "UNS NUMBER INDEX", [http://www.astm.org/digital\\_library/mnl/source\\_pagees/mnl12062d\\_index.pdf](http://www.astm.org/digital_library/mnl/source_pagees/mnl12062d_index.pdf), [May. 30, 2013]
- [64] "Cost Effective and Efficient Method for Grinding and Polishing". LECO Corporation; Saint Joseph, Michigan USA, [http://www.leco.com/resources/application\\_notes/pdf/GPX\\_FESTAR\\_POLISHING\\_FILM\\_CARBOON\\_STEEL\\_203-821-382.PDF](http://www.leco.com/resources/application_notes/pdf/GPX_FESTAR_POLISHING_FILM_CARBOON_STEEL_203-821-382.PDF), [Jan. 20, 2010]

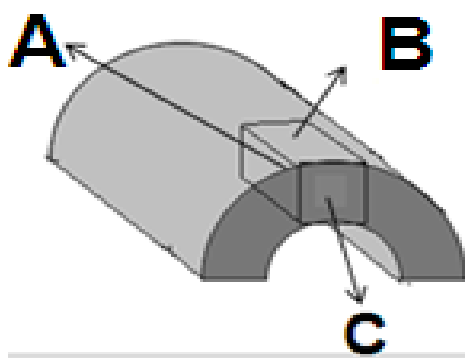
- [65] Chevron Corporation, Energy Technology Company, FE - MEE - Corrosion Lab, 3901 Briarpark Dr., WP117, Houston, TX 77042 U.S.A.
- [66] Micrograph Library, 2004, University of Cambridge. Available: [www.doitpoms.ac.uk/miclib/index.php](http://www.doitpoms.ac.uk/miclib/index.php), [Mar. 30, 2013]
- [67] S. Smith, Corrosion and Materials Consultant retired from ExxonMobil. Now he is Corrosion and Materials Consultant and Adjunct Professor for Ohio University, ICMT, personal communication, 2011, Feb 15.
- [68] Y. Li, F. Wang, and G. Liu, "Grain Size Effect on the Electrochemical Corrosion Behavior of Surface Nanocrystallized Low-Carbon Steel," *Corrosion*, Vol. 60, pp. 891-896, 2004.
- [69] R. Napolitano. "Measurement of ASTM grain size number," *Materials Science & Engineering*, Iowa State University.
- [70] W. Rasband. "ImageJ, Image Processing and Analysis in Java," <http://rsbweb.nih.gov/ij/>, [May. 30, 2013]
- [71] <http://www.argentumsolutions.com/publications/CorrVol60p10032004.pdf>, [Apr. 25, 2013]
- [72] G. Schmitt and B. Rothmann, "Corrosion mechanism of unalloyed steel in oxygen free carbon dioxide solutions - Part 1: Kinetics of the liberation of hydrogen," *Werkst. Korros.*, Vol. 28, No. 12, pp. 816-822, 1977.
- [73] A, Nor. *The Effect of Turbulent Flow on Corrosion of Mild Steel in High Partial CO<sub>2</sub> Environments*. PhD dissertation. The Russ College of Engineering and Technology of Ohio University. May 2013.
- [74] Corrosion Control in Petroleum Production - TPC Publication 5. NACE International, 1979.

- [75] P. Roberge, *Corrosion Testing Made Easy: Erosion-Corrosion*. NACE Press, 2004.
- [76] H. Wang, T. Hong, J. Yong, W. Jepson, and C. Bosch, "Enhanced Mass Transfer and Wall Shear Stress in Multiphase Slug Flow," *Corrosion/2002*, Houston, TX, NACE, Paper. 02501.
- [77] "Shear Stress Sensors/Inline Viscometers," 105 Lock St. Suite 301 – Newark, NJ 07103, <http://www.lenterra.com/products/shear-stress-sensors>, [May, 2012]
- [78] R. B. Dean. "Reynolds Number Dependence of Skin friction and other Bulk Flow Variables in Two-dimensional Rectangular Duct Flow," *J. Fluids Eng.* vol. 100, no 2, pp. 219-242, 1978.
- [79] ASTM Standard G1, 2003, "Standard Practice for Preparing, Cleaning, and Evaluating Corrosion Test Specimens," ASTM International, West Conshohocken, PA, 2003, DOI: 10.1520/G0001-03, [www.astm.org](http://www.astm.org)
- [80] V. Fajardo. *Localized CO<sub>2</sub> Corrosion in the Presence of Organic Acids*. MS thesis. The Russ College of Engineering and Technology of Ohio University. March 2011.
- [81] V. Fajardo, B. Brown, D. Young, and S. Netic, "Study of the Solubility of Iron Carbonate in the Presence of Acetic Acid using an EQCM," *Corrosion/2013*, Houston, TX, NACE, Paper. 2452.
- [82] Y. Wu and K. T., "Reynolds-Stress Enhancement Associated with a Short Fetch of Roughness in Wall Turbulence," *Corrosion/2013*, Christensen University of Illinois at Urbana, Champaign, Urbana, Illinois 61801, DOI: 10.2514/1.22357.

## APPENDIX A: GRINDING, POLISHING, AND ETCHING PROCEDURES

Samples Mounting:

Three sections from different planes were cut from each material and mounted in Bakelite\* using Metallurgical Mounting Press machine.



a-Samples cut from 3 orientations



b- Mounted in Bakelite

Figure A1: Schematic diagram show how the three different planes were cut and the samples after being mounted in Bakelite.

Grinding & Polishing:

The grinding and polishing processes were conducted using a BUEHLER AutoMet-2000 polishing machine that allows grinding and polishing of samples in one step.

---

\*Trade name for plastic mounting material. Bakelite is a synthetic resin chemically formulated. The Bakelite powder is used with specimens mounting press machine for mounting of samples.



Figure A2: BUEHLER AutoMet-2000 polishing machine that was used to conduct grinding and polishing work.

#### Coarse Grinding:

Start grinding with the 150 grit abrasive papers, with 150 rpm for head speed and 200 – 250 rpm for base speed; and 20 lb pressure force. The grinding time from 2–4 minutes depends on the surface of the sample. The purpose of this step is to remove the deformation produced during sectioning, and to produce an initially flat surface.

#### Fine Grinding:

Samples were cleaned to remove any grits then grinding started with 400 grit abrasive papers, with 150 rpm for head speed and 200–250 rpm for base speed; and 20 lb pressure force. The grinding time is 4 minutes.

Samples were cleaned to remove any grits then grinding started with 600 grit abrasive papers, with 150 rpm for head speed and 300 rpm for base speed; and 20 lb pressure force. The grinding time depends on the surface (4–6 minutes).

### Rough Polish:

Samples were washed with soap and a cotton ball then rinsed immediately in isopropyl alcohol. Specimens are then placed in a beaker of isopropyl alcohol which is then placed in an ultrasonic bath for a minute, and then rewashed with running water and rinsed with isopropyl alcohol.

Polishing was started using 9  $\mu\text{m}$  monocrystalline diamonds and synthetic napped cloth with 150 rpm for head speed and 150 rpm for base speed; and 20 lb pressure force. The polishing time is from 4 – 8 minutes. Samples were rewashed with running water and rinsed with isopropyl alcohol.

The previous step was repeated for 3 $\mu\text{m}$  and then for 1 $\mu\text{m}$  monocrystalline diamonds. After washing the samples with running water and rinsing with isopropyl alcohol to remove any diamond particles, fine polishing could then be started.

### Fine Polishing:

Polishing was started using 0.05  $\mu\text{m}$  alumina slurry in water and fine woven silk, with 150 rpm for head speed, 150 rpm for base speed and 15 lb pressure force. The polishing time is 2 minutes.

Samples are well washed with running water and rinsed with isopropyl alcohol. The samples were placed in a beaker of isopropyl alcohol and put in the ultrasonic bath for a minute, and then samples rewashed with running water and rinsed with isopropyl alcohol. Samples were then dried with cold dry air.

If the sample is porous, drying the sample with the blow-dryer helps prevent bleed out of water in the pores.

Steel Etching Procedure:

The etching was conducted using 2% Nital, prepared in-house.

Material and Equipment used:

- 2% Nital (2% nitric acid& ethanol) that was prepared previously.
- Cotton swabs.
- Samples to be etched.

Procedure:

Drop a couple drops of etchant on the cotton swab (use the bottle tip).

Samples were swabbed with cotton in a circular motion, until haze began to appear (gray color) on the polished surface.

Rinsing was then conducted immediately under warm running water, samples rinsed with isopropyl alcohol, and then dried with cold air.

## APPENDIX B: INTERCEPT METHOD AND IMAGEJ SOFTWARE

Intercept Method, ASTM E112 Standard:

The basic steps to determine grain size are described below:

1. Apply number of lines of known total length  $L$ , see Figure B1.
2. Count total intercepts between test lines and grain boundaries  $P$ .
3. Define grain size number from chart shown in Figure B2.
4. Obtain grain size diameter and area from table shown in Figure B3.

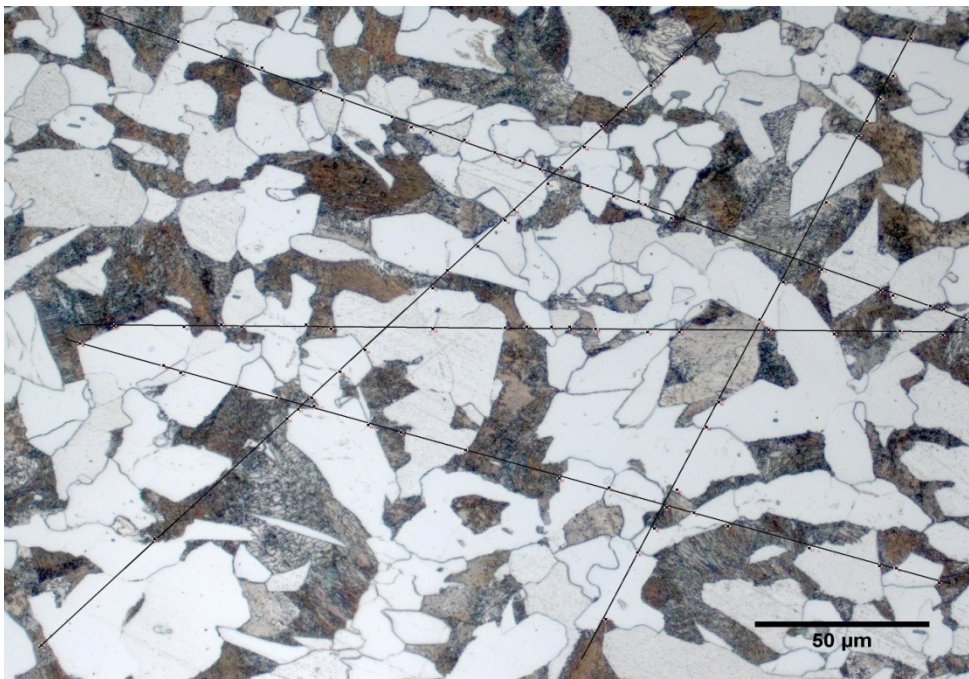


Figure B1: Image show number of lines of known combined total length  $L$  and the intercepts between these lines and grain boundaries.

E 112

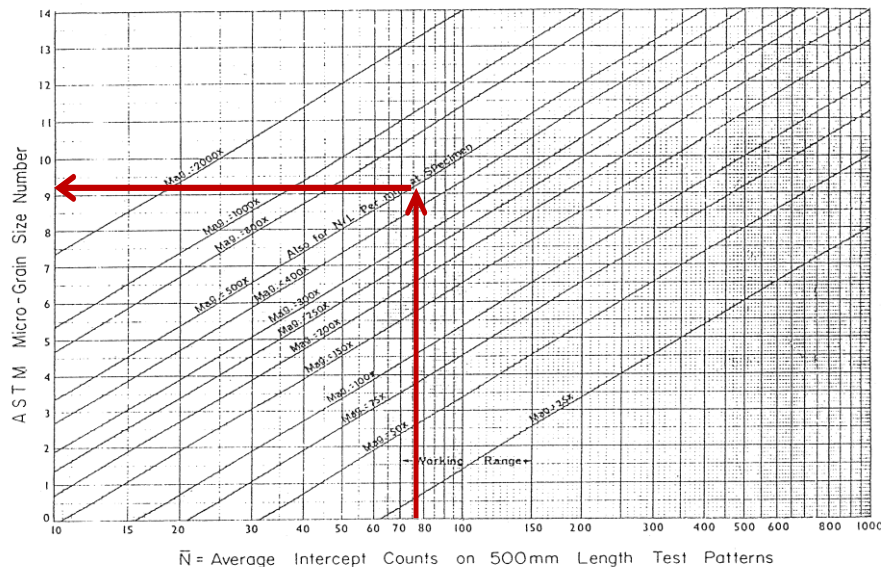


FIG. 6 Chart for Direct Determination of ASTM Micro-Grain Size Number from Intercept Count on 500-mm Test Pattern

Figure B2: Chart used to determine grain size number from the average intercepts [25].

E 112

TABLE 2 Micro-Grain Size Relationships Computed for Uniform Randomly Oriented Equiaxed Grains

nt—For diameters in inches, see Table 4 (divide by 100).

ASTM Micro-Grain Size Number G	"Diameter" of Average Grain Section <sup>a</sup>		Average Intercept Distance <sup>b</sup> $\bar{l}$ , mm	Intercept Count, $n/l$ per mm	Area of Average Grain Section, $\bar{a}$ , mm <sup>2</sup>	Calculated Number of Grains per mm <sup>2</sup> , $n/\bar{a}$ <sup>c</sup>	Average	
	Nominal $d_n$ , mm	Feret's $d_f$ , mm					Grains per mm <sup>2</sup> at $1\times, \bar{a}$	Grains per in. <sup>2</sup> at $100\times, n/\bar{a}$
5.0	65	71	56.6	17.7	4.03	3126	248	16.00
(5.2) <sup>d</sup>	60	68	53.2	18.8	3.60	3708	278	17.92
5.5	55	60	47.6	21.0	2.85	5258	351	22.63
(5.7) <sup>d</sup>	50	56	44.3	22.6	2.50	6400	400	25.81
6.0	45	50	40.0	25.0	2.02	8842	496	32.00
(6.4) <sup>d</sup>	40	45	35.4	28.2	1.60	12 500	625	40.32
6.5	38	42	33.6	29.7	1.43	14 871	701	45.25
(6.7) <sup>d</sup>	35	39	31.0	32.2	1.23	18 659	816	52.67
7.0	32	36	28.3	35.4	1.008	25 010	992	64.00
(7.2) <sup>d</sup>	30	34	26.6	37.6	0.900	29 630	1111	71.68
7.5	27	30	23.8	42.0	0.713	41 061	1403	90.51
(7.7) <sup>d</sup>	25	28	22.2	45.1	0.625	51 200	1600	103.23
	$\mu\text{m}$	$\mu\text{m}$	$\mu\text{m}$		mm <sup>2</sup> $\times 10^{-3}$	$\times 10^6$	$\times 10^3$	
8.0	22	25	20.0	50.0	504	0.0707	1.98	128.0
(8.4) <sup>d</sup>	20	23	17.7	56.4	400	0.1000	2.50	161.3
8.5	19	21	16.8	59.5	356	0.1190	2.81	181.0
9.0	16	18	14.1	70.7	252	0.2000	3.97	256.0
(9.2) <sup>d</sup>	15	17	13.3	75.2	225	0.237	4.44	286.7
9.5	13	15	11.9	84.1	178	0.336	5.61	362.0
10.0	11	13	10.0	100	126	0.566	7.94	512.0

Figure B3: Table used to define grain diameter and area from the grain size number that obtained from the previous chart [25].

### ImageJ Software:

An example screenshot which contains several windows and applications of ImageJ software is shown in Figure B4.

The basic steps to determine grain size are described below:

- 1- Set the scale by selecting *Analyze* and *SetScale*.
- 2- Convert the image to gray scale by selecting *Image* then *Type 8-bit*.
- 3- Convert the image to black and white, by selecting *Make Binary*, to define grain edges Figure B5.
- 4- Defined the grain size and area fraction by selecting *Analyze Particles*.

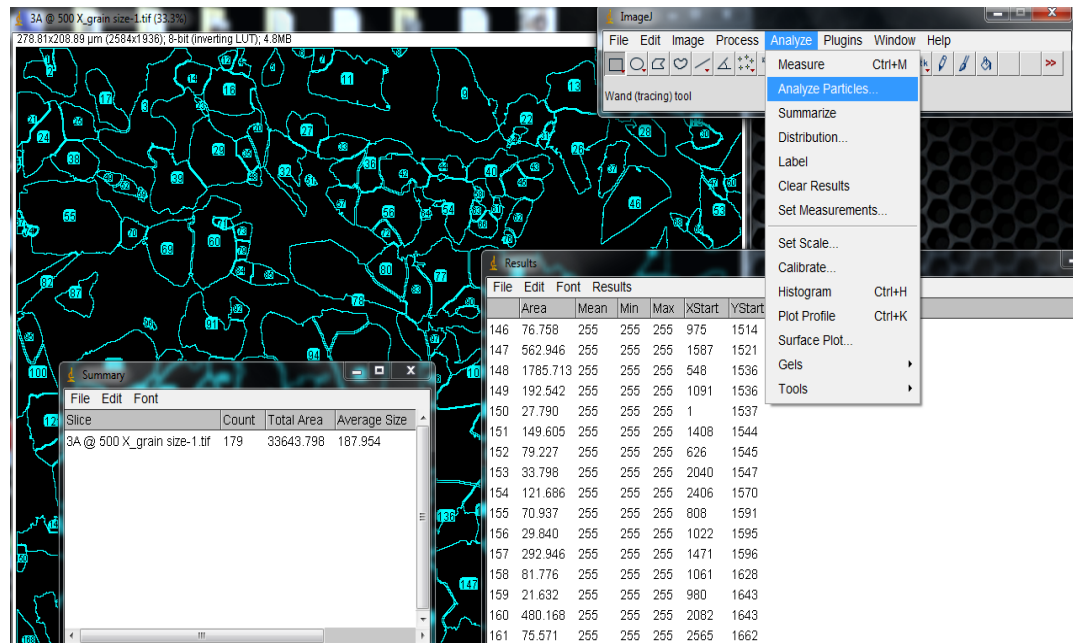
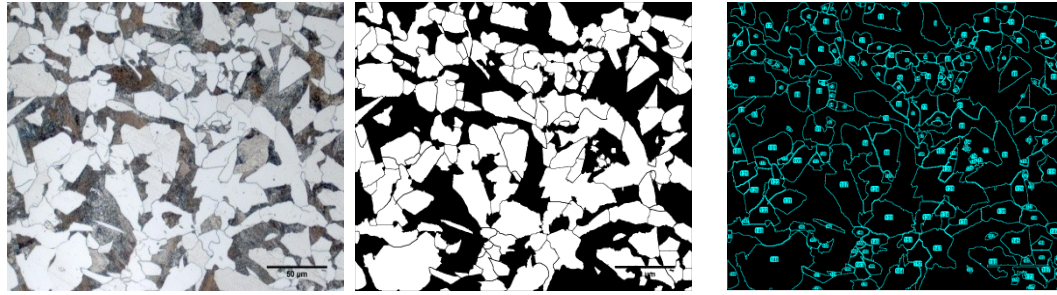


Figure B4: Screenshot of several windows and applications of ImageJ software [26].



Original Image

Black &amp; white and edges

Calculation of grain sizes

Figure B5: Defined edges of grains and calculate grain size.

## APPENDIX C: THIN CHANNEL FLOW CELL (TCFC) SYSTEM DESIGN

The TCFC system was designed and developed in Institute for Corrosion and Multiphase-Technology - Ohio University.

The TCFC is composed of two parts, see Figure C1:

### Part I: Tank, Heat Exchanger, Pump, and Piping System.

The volume of the tank is about 48 gallons. A heat exchanger is used to control and stabilize temperature to a desired level, this cannot be adequately controlled at high flow rates. The piping system includes a pH meter, which is used to monitor the pH of the solution, and an ion exchanger, which is used to control the water chemistry of the system.

### Part II: The TCFC Cell.

The dimensions of the flow cell are designed for fully developed turbulent flow. The height of the TCFC is 3.0mm, to facilitate high wall shear stresses, and the width of the TCFC is 90mm to obtain fully developed turbulent flow and eliminate edge effects. Four ports permit introduction of 1.25 inch (31 mm) diameter samples for each experiment, see Figure C3.

### System Control:

The whole TCFC system has two temperature controllers, one for the flow cell and one for the tank. This ensures temperature stabilization for the whole system. A flow meter is used to accurately control the volumetric flow rate. A pressure gauge is used to control the pressure of the system.

### Probes:

Two kinds of probes were used in the TCFC for corrosion study, a Linear Polarization Resistance (LPR) probe and Weight Loss (WL) probe, see Figure C2. This allows a variety of methods to be employed for measurements relating to corrosion processes. Sample holders were designed to hold a flush mounted, 1.25 inch (31 mm) diameter weight loss coupon, which makes the probes directly exchangeable with other flow loops.



TCFC: has four places with valves to install samples using sample holders



Piping system contain points for pH measurements and ion exchanger to control water chemistry

Figure C1: Images of the real thin channel flow cell (TCFC) system that used to conduct corrosion experiment.

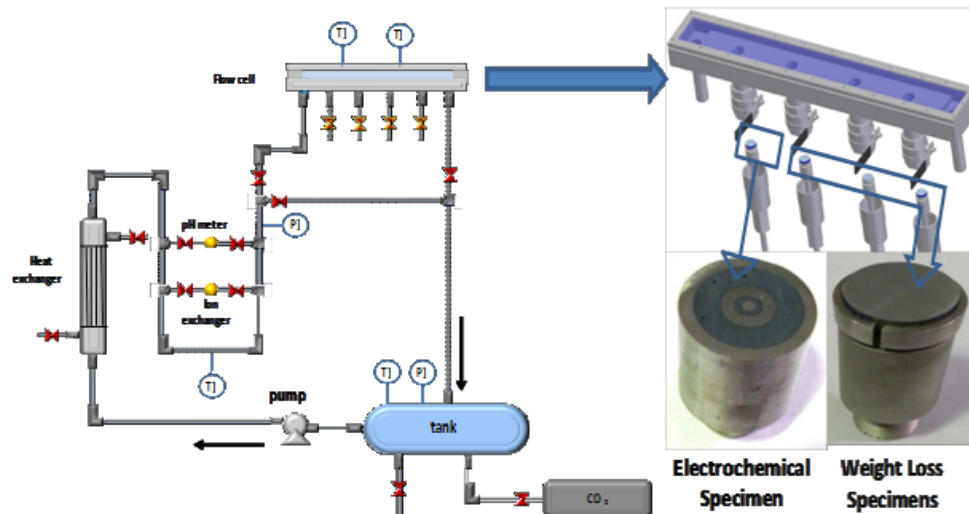


Figure C2: Schematic diagram of the thin channel flow cell (TCFC) system and samples used to conduct corrosion experiments [20].

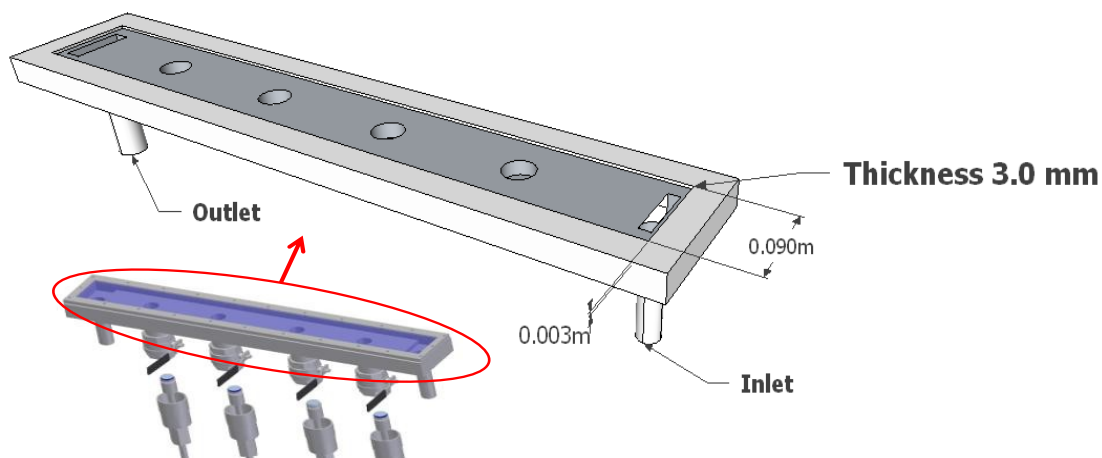


Figure C3: Schematic diagram show the dimensions of the thin channel that allow to obtain good control in flow conditions and to generate high wall shear stresses.

## APPENDIX D: REPEATED EXPERIMENTS

As mentioned in Chapter 6, a few of the key experiments were repeated to make sure that the results can be replicated (with the X65I – Q&T steel and A106GRB-normalize steel). One additional repeated experiment (with X65II steel), was conducted to find out whether pitting was caused as a result of the high wall shear stress or if it was due to metallurgical factors such as the presence of inclusions. The repeated experiments were conducted under the same conditions and using the same procedure used for the original experiments as described in Chapter 6.

The results of LPR, weight loss, SEM, and IFM of the repeated tested steels are analyzed separately for each steel type by making a comparison with the previous results.

### X65I steel:

Variation of the LPR corrosion rate of X65I, the repeated experiment (Experiment II), with exposure time is shown in Figure D1. At the beginning, the corrosion rate was high (9-10 mm/y); during the  $\text{FeCO}_3$  layer formation, the corrosion rate gradually reduced until reaching less than 1.0 mm/y after about 20 hours and remained the same during the remaining exposure time. After removal the first sample, the wall shear stress was increased to 535 Pa for the remainder of the experiment. The images taken by SEM upon removal of the samples from the system after 2 days of exposure show that the surface was fully covered with an  $\text{FeCO}_3$  layer, Figure D2 (Experiment II).

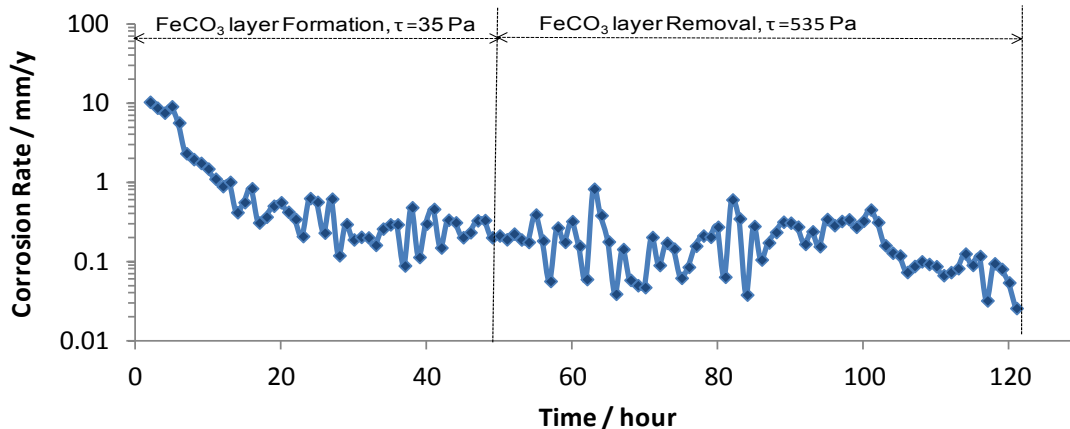
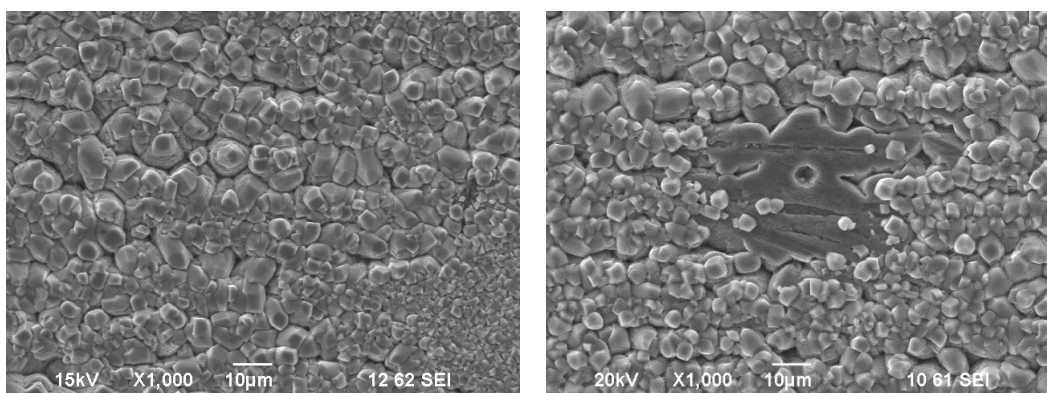


Figure D1: LPR Corrosion rate of X65I steel (Experiment II) during 5 days of exposure at 80°C, 1.5 bar CO<sub>2</sub>, pH 6.6, B=26 mV/decade,  $\tau=35$  Pa for the FeCO<sub>3</sub> layer formation,  $\tau=35$  Pa for the first 2 days,  $\tau=535$  Pa for another 3 days.

The comparison of SEM images of the previous experiment (Experiment I), shown in chapter 6, and this experiment (Experiment II) show that both samples were fully covered with an FeCO<sub>3</sub> layer, see Figure D2.



Experiment I

Experiment II

Figure D2: Comparison of SEM top surface analysis of FeCO<sub>3</sub> layer after 2 days of exposure (Experiments I & II) at 80°C, X65I steel, 1.5 bar CO<sub>2</sub>, pH 6.6,  $\tau=35$  Pa for the first 2 days.

After 5 days of exposure, the two remaining samples were removed and the weight loss corrosion rate was found to be 1.4 mm/y, as shown in Figure D3 (Experiment II). There is no significant differences between the corrosion rate between the two experiments, see Figure D3. Images that were taken by SEM upon removal of the samples from the system at the end of exposure to the high wall shear stress showed that the steel sample remained mostly covered by a dense  $\text{FeCO}_3$  layer, as shown in Figure D4 (Experiment II). However, comparison of SEM images before and after the increase in wall shear stress show that the  $\text{FeCO}_3$  crystals were removed from some small areas after the wall shear stress increased, see Figure D2 and Figure D4 (Experiment II). Here again the comparison of SEM images of the previous experiment (Experiment I) and this experiment (Experiment II) that were taken upon removal of the sample from the system after five days of exposure show that the  $\text{FeCO}_3$  crystals that were removed from the sample in experiment I were larger compared with the sample in experiment II. The images of the SEM cross-section analyses show that the sample surface in both experiments were fully covered by an  $\text{FeCO}_3$  layer, see Figure D5. Additionally, the IFM analysis shows the deepest pit with 50  $\mu\text{m}$  in depth and about 70  $\mu\text{m}$  in width, see Figure D6 (Experiment II). However, in experiment I, the deepest pit was 70  $\mu\text{m}$  in depth and about 300  $\mu\text{m}$  in width, see Figure D6 (Experiment I). As shown in Figure D7 (experiment II), the penetration rate of the deepest pit is compared with final corrosion rate measured by LPR, where the final corrosion rate represents the actual corrosion rate at the end of the experiment. Here the deepest pit penetration rate is calculated to be 3.7 mm/y. The deepest pit penetration rate is very large compared with final corrosion rate

that measured by LPR, which is 0.1 mm/y. The final corrosion rate is assumed to be the true corrosion rate corresponding to long periods of exposure.

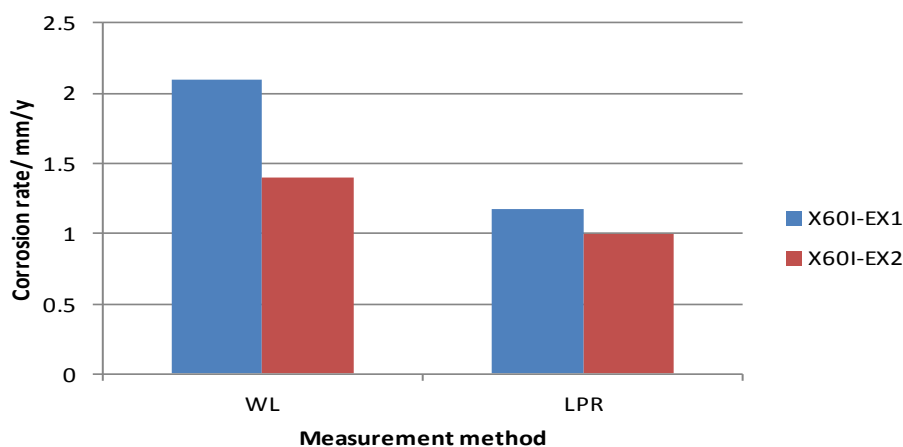
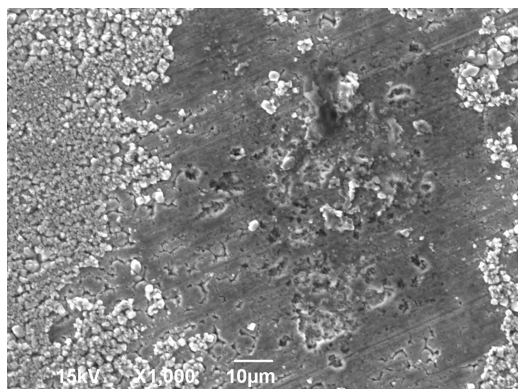
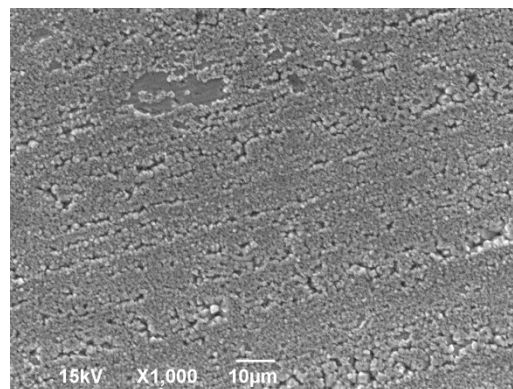


Figure D3: Comparison between corrosion rates measured by weight loss (WL) and integrated LPR after 5 days of exposure (Experiments I & II), at 80°C, X65I steel, 1.5 bar CO<sub>2</sub>, pH 6.6, B=26 mV/decade,  $\tau=35$  Pa for the FeCO<sub>3</sub> layer formation,  $\tau=35$  Pa for the first 2 days,  $\tau=535$  Pa for another 3 days.

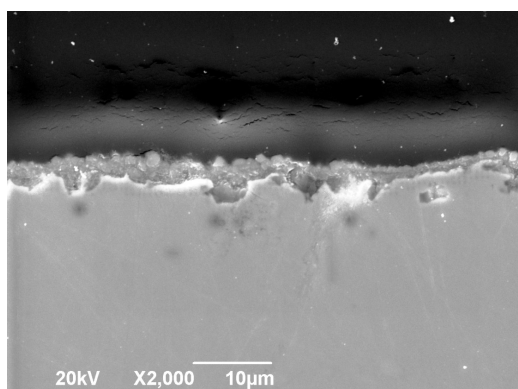


Experiment I

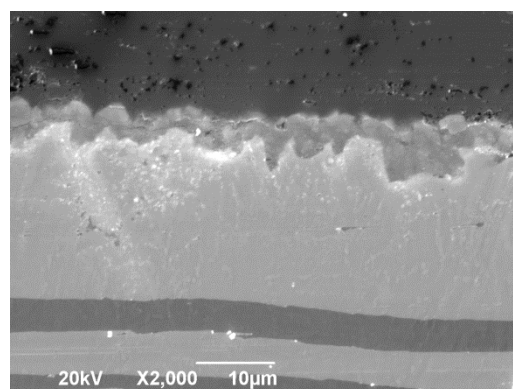


Experiment II

Figure D4: Comparison between SEM top surface analysis of  $\text{FeCO}_3$  layer after 5 days of exposure (Experiments I & II), at  $80^\circ\text{C}$ , X65I steel, 1.5 bar  $\text{CO}_2$ , pH 6.6,  $\tau = 35$  Pa for the first 2 days,  $\tau = 535$  Pa for another 3 days.

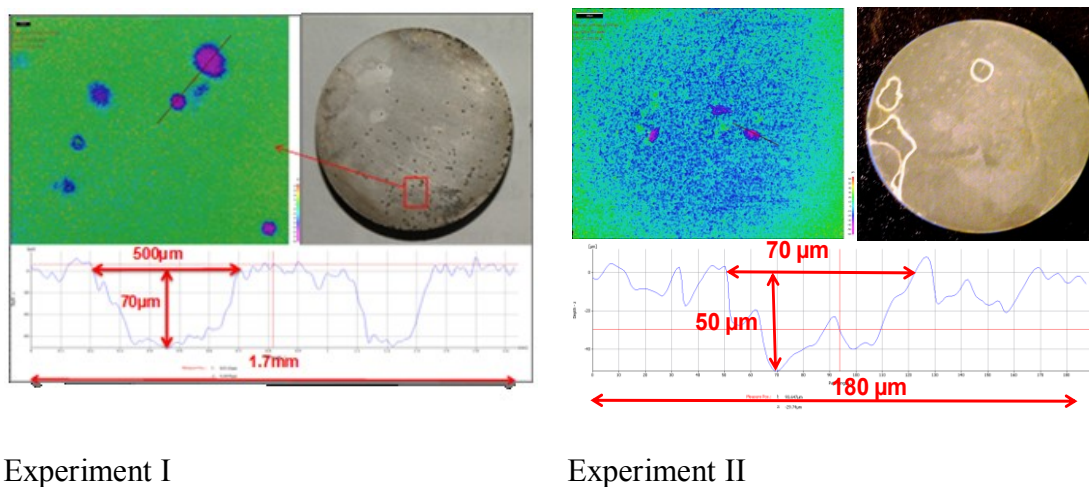


Experiment I



Experiment II

Figure D5: Comparison between SEM cross section analysis of  $\text{FeCO}_3$  layer after 2 days of exposure (Experiments I & II) at  $80^\circ\text{C}$ , X65I steel, 1.5 bar  $\text{CO}_2$ , pH 6.6,  $\tau = 35$  Pa for the first 2 days,  $\tau = 535$  Pa for another 3 days.



Experiment I

Experiment II

Figure D6: Comparison between IFM image of descaled sample after 5 days of exposure (Experiments I & II) at 80°C, X65I steel, 1.5 bar CO<sub>2</sub>, pH 6.6,  $\tau = 35$  Pa for the first 2 days,  $\tau = 535$  Pa for another 3 days.

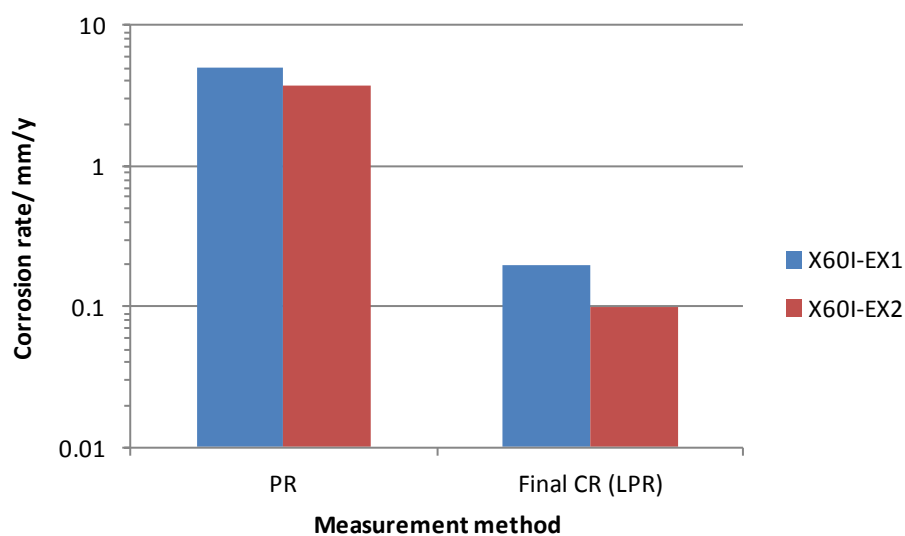


Figure D7: Comparison between corrosion rates measured by weight loss (WL), integrated LPR and average penetration rate (PR) of the deepest pits on each steel (Experiments I & II) after 5 days of exposure at 80°C, X65I steel, 1.5 bar CO<sub>2</sub>, pH 6.6,  $B = 26$  mV/decade,  $\tau = 35$  Pa for the first 2 days,  $\tau = 535$  Pa for another 3 days.

A106GRB steel:

Variation of the LPR corrosion rate of A106 in the repeated experiment (Experiment II), with exposure time is shown in Figure D8. At the beginning, the corrosion rate was high (5-6 mm/y); during the  $\text{FeCO}_3$  layer formation, the corrosion rate gradually reduced until reaching less than 0.1 mm/y after about 20 hours and remained the same during the remaining exposure time. After removal the first sample, the wall shear stress was increased to 535 Pa for the remainder of the experiment. After about 50 hours the corrosion rate increased until reaching 0.9 mm/y; however, there were no indications that the  $\text{FeCO}_3$  layer was destroyed or removed.

The images taken by SEM upon removal of the samples from the system after 2 days of exposure show that the surface was fully covered with an  $\text{FeCO}_3$  layer, Figure D9 (Experiment II).

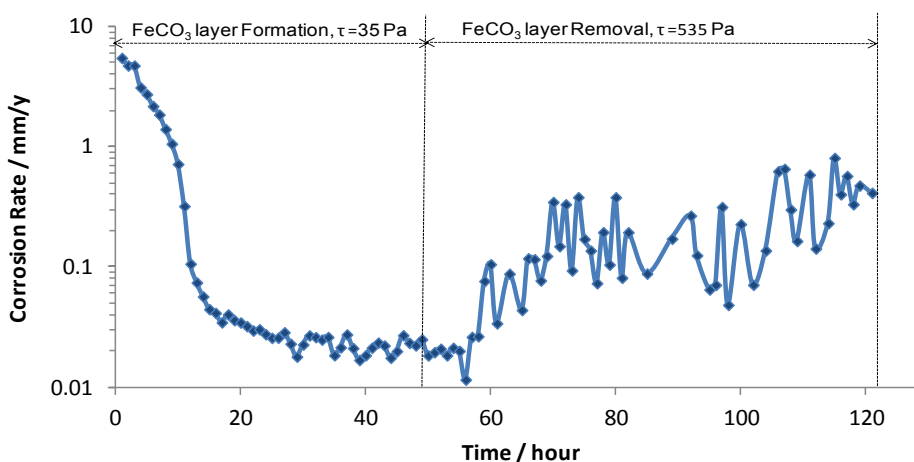
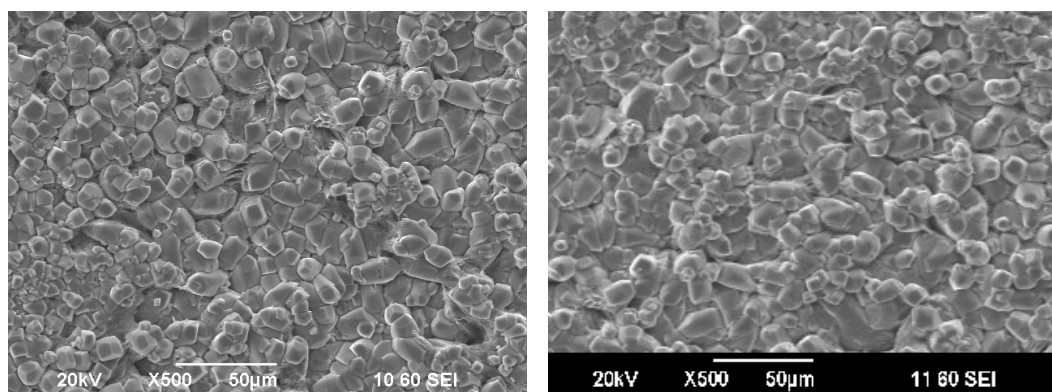


Figure D8: LPR Corrosion rate of A106 steel (Experiment II) during 5 days of exposure at 80°C, 1.5 bar  $\text{CO}_2$ , pH 6.6,  $B=26$  mV/decade,  $\tau=35$  Pa for the  $\text{FeCO}_3$  layer formation,  $\tau=35$  Pa for the first 2 days,  $\tau=535$  Pa for another 3 days.

The comparison of SEM images of the previous experiment (Experiment I), shown in Chapter 6, and this experiment (Experiment II) show that both samples were fully covered with an  $\text{FeCO}_3$  layer, see Figure D8.



Experiment I

Experiment II

Figure D9: Comparison of SEM top surface analysis of  $\text{FeCO}_3$  layer after 2 days of exposure (Experiments I & II) at  $80^\circ\text{C}$ , A106 steel, 1.5 bar  $\text{CO}_2$ , pH 6.6,  $\tau = 35$  Pa for the first 2 days.

After 5 days of exposure, the two remaining samples were removed and the weight loss corrosion rate was found to be 1.3 mm/y, as shown in Figure D10 (Experiment II). There is no significant differences between the corrosion rate in both experiments, see Figure D10. Here again the comparison of SEM images of the previous experiment (Experiment I) and this experiment (Experiment II) that were taken upon removal of the sample from the system after five days of exposure show that the sample was fully covered with an  $\text{FeCO}_3$  layer, Figure D11. However, after increasing wall shear stress the sample shows more voids than the sample that was taken before increasing wall shear stress. The images of the SEM cross-section analyses also show that the samples in both experiments were fully covered by an  $\text{FeCO}_3$  layer, see Figure D12. Additionally,

the IFM analysis of the sample after descaling shows some wide pits with different sizes, Figure D13 (Experiment II). The comparison between the IFM images of the previous experiment (Experiment I) and this experiment (Experiment II) show that the sample of the previous experiment contains narrower pits. However, there is no significant difference between the depth of the pits in both experiments, see Figure D13.

As shown in Figure D14, the penetration rate of the deepest pit was compared to the final corrosion rate measured by LPR. Here the deepest pit penetration rate is calculated to be 2.0 mm/y. The deepest pit penetration rate is still large as compared to the final corrosion rate measured by LPR, which is 0.6 mm/y.

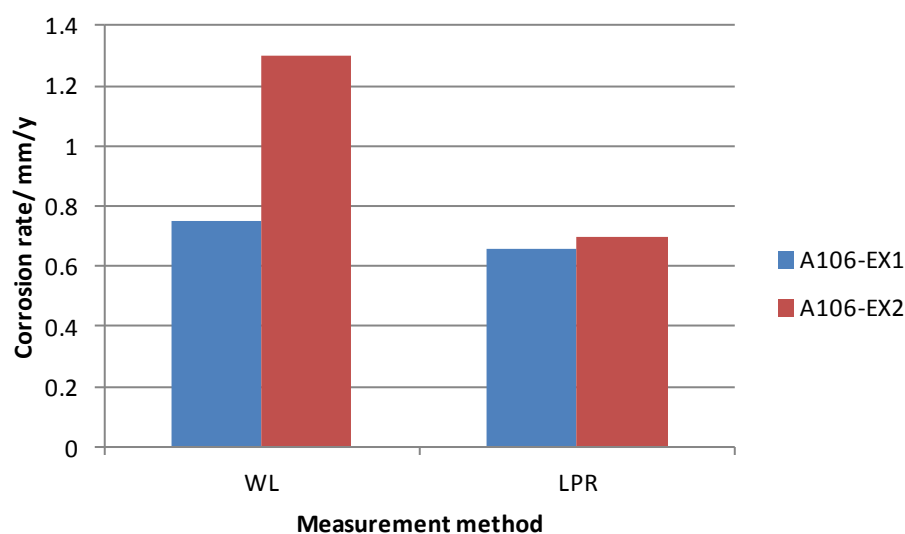
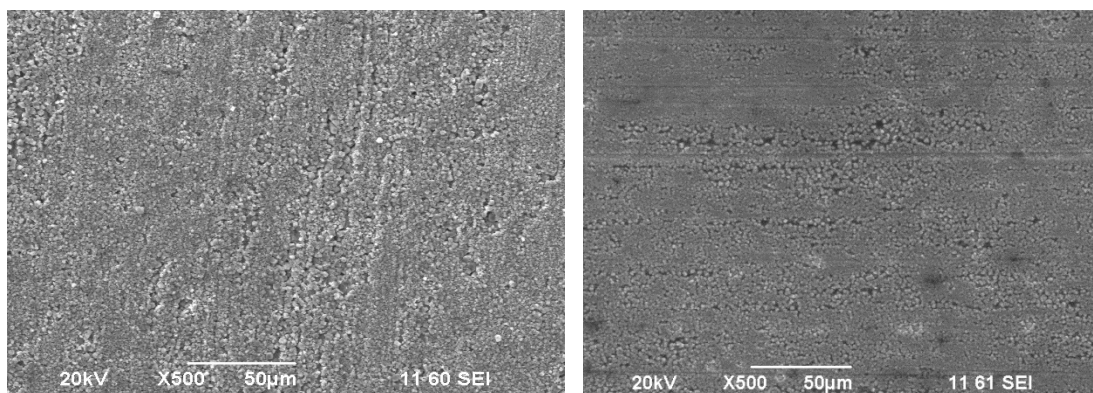


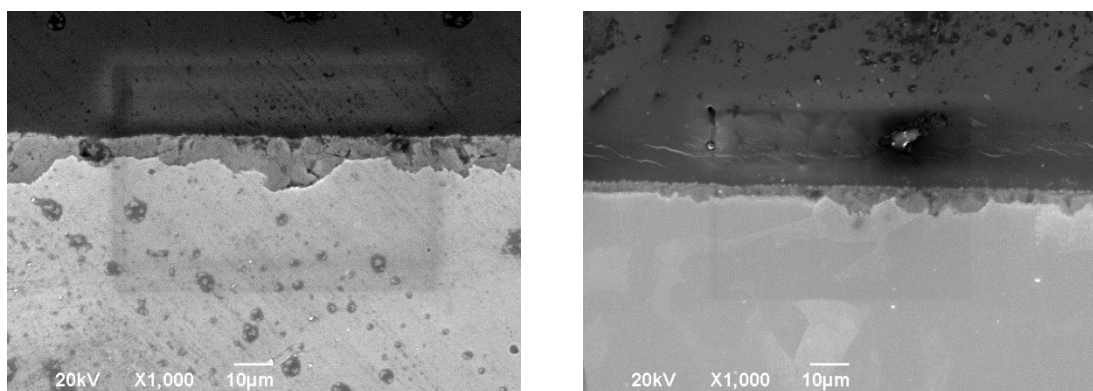
Figure D10: Comparison between corrosion rates measured by weight loss (WL) and integrated LPR after 5 days of exposure (Experiments I & II), at 80°C, A106 steel, 1.5 bar CO<sub>2</sub>, pH 6.6, B=26 mV/decade,  $\tau$ = 35 Pa for the FeCO<sub>3</sub> layer formation,  $\tau$ = 35 Pa for the first 2 days,  $\tau$ = 535 Pa for another 3 days.



Experiment I

Experiment II

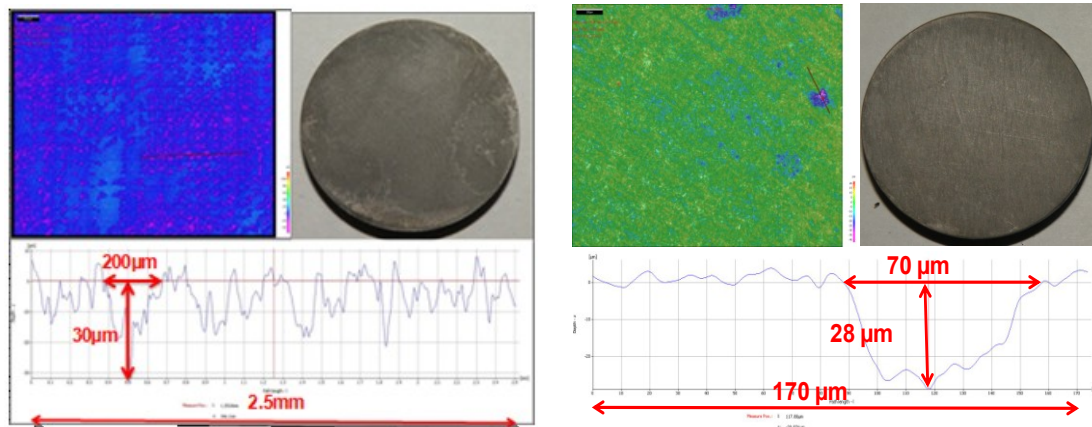
Figure D11: Comparison between SEM top surface analysis of  $\text{FeCO}_3$  layer after 5 days of exposure (Experiments I & II), at  $80^\circ\text{C}$ , A106 steel, 1.5 bar  $\text{CO}_2$ , pH 6.6,  $\tau = 35$  Pa for the first 2 days,  $\tau = 535$  Pa for another 3 days.



Experiment I

Experiment II

Figure D12: Comparison between SEM cross section analysis of  $\text{FeCO}_3$  layer after 2 days of exposure (Experiments I & II) at  $80^\circ\text{C}$ , A106 steel, 1.5 bar  $\text{CO}_2$ , pH 6.6,  $\tau = 35$  Pa for the first 2 days,  $\tau = 535$  Pa for another 3 days.



Experiment I

Experiment II

Figure D13: Comparison between IFM image of descaled sample after 5 days of exposure (Experiments I & II) at 80°C, A106 steel, 1.5 bar CO<sub>2</sub>, pH 6.6,  $\tau = 35$  Pa for the first 2 days,  $\tau = 535$  Pa for another 3 days.

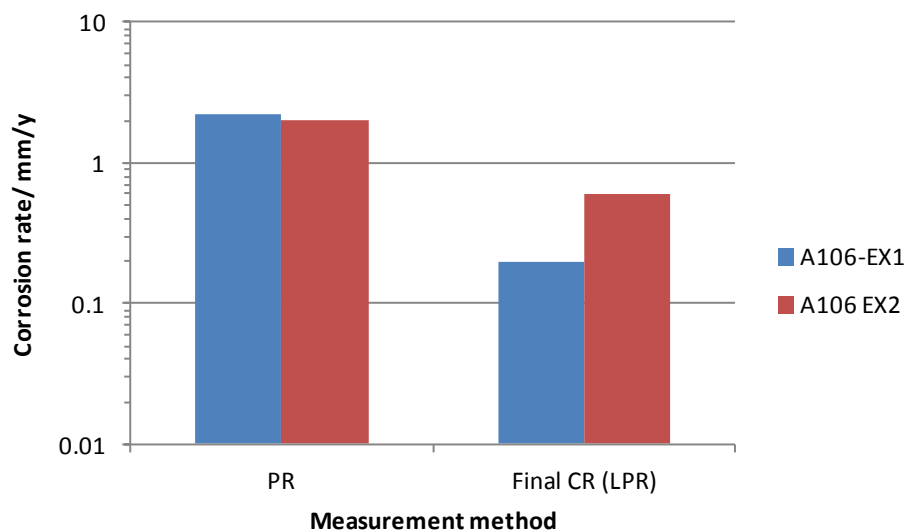


Figure D14: Comparison between corrosion rates measured by weight loss (WL), integrated LPR and average penetration rate (PR) of the deepest pits on each steel (Experiments I & II) after 5 days of exposure at 80°C, A106 steel, 1.5 bar CO<sub>2</sub>, pH 6.6,  $B = 26$  mV/decade,  $\tau = 35$  Pa for the first 2 days,  $\tau = 535$  Pa for another 3 days.



**OHIO**  
UNIVERSITY

Thesis and Dissertation Services